

---

Enhanced single – shot flame  
thermometry with  
femtosecond / picosecond  
CARS using a phase –  
characterized picosecond probe  
pulse.

M.Sc. Thesis

Anand Vijayaraghavan

---



# Enhanced single-shot flame thermometry with fs/ps CARS using a phase-characterized picosecond probe pulse

By

Anand Vijayaraghavan

Student number – 5047471

in partial fulfillment of the requirements for the degree of

**Master of Science**  
in Aerospace Engineering

at the Delft University of Technology,  
to be defended publicly on Friday, November 26, 2021, at 02:00 PM.

Thesis committee:

Dr. Arvind G. Rao,  
Dr. A. Anisimov,  
Dr. Alexis Bohlin,  
Ir. L. Castellanos,

*Chairperson*  
*External examiner*  
*Principal supervisor*  
*Daily supervisor*

An electronic version of this thesis is available at <http://repository.tudelft.nl/>.



# Contents

Contents .....	5
Table of figures .....	7
Summary .....	10
Introduction .....	11
Theory of CARS .....	13
2.1 Non-linear light-matter interaction .....	13
2.2 Four-wave mixing and CARS .....	14
2.3 Energy and momentum conservation: Phase-matching .....	16
2.4 Time-domain representation of the (rotational) Raman response .....	17
2.4.1 Molecular Response .....	19
2.4.2 Time-domain modeling .....	21
2.5 CSRS signal (Coherent Stokes Raman Scattering).....	24
2.6 Non-resonant signal.....	24
2.7 CARS signal intensity .....	26
2.8 Transform-limit and chirp .....	26
2.9 Hybrid fs/ps CARS .....	29
2.10 CPP CARS .....	30
Experimental setup: two-beam hybrid fs/ps CARS .....	33
3.1 Laser system .....	34
3.2 Degenerate pump/Stokes pulse .....	34
3.2.1 Two-beam phase-matching.....	34
3.3 SHBC and the probe pulse .....	35
3.4 4F filter.....	36
3.5 Camera and spectrometer .....	37
Research objective .....	38
4.1 Utilizing the direct probe pulse from the SHBC for hybrid fs/ps CARS.....	39
4.2 Impact of the extra photon content on signal-to-noise ratio and precision .....	44
Methodology: Characterization of the probe pulse .....	49
5.1 Discretization and characterization of the frequency information .....	49
5.2 Characterization of time (– and full phase) content .....	51
5.3 Modeling the synthetic representation of the probe pulse.....	56
5.4 Validation of the synthetic probe pulse model .....	58
5.5 Optimization of the acquired phase information .....	60
Results and discussion .....	65
6.1 Synthetic probe representation .....	65
6.2 Synthetic reconstruction of the nitrogen CSRS spectrochronogram .....	66
6.3 Synthetic reconstruction of the Air CSRS spectrochronogram .....	69

6.4	Flame thermometry.....	71
6.4.1	Center of the burner.....	72
6.4.2	Near the flame front.....	74
	Conclusions.....	76
	Appendix.....	78
	Probe pulse fluctuations.....	78
	Spectral coincidence of the probe and CARS signal.....	80
	Impact of the direct probe on the non-resonant signal.....	81
	Limits on the characterization and validation processes.....	83
	Phase information from the optimization.....	83
	Bibliography.....	85
	Acknowledgments.....	88

# Table of figures

Figure 1: Second-harmonic generation: depicting frequency conversion.....	14
Figure 2: The third-order nonlinear CARS process .....	15
Figure 3: The anharmonic potential containing the quantized vibrational and rotational states .....	16
Figure 4: CARS phase-matching approaches. ....	17
Figure 5: Synthetic frequency domain molecular response for nitrogen gas at 300K. ....	18
Figure 6: Frequency spread dephasing .....	20
Figure 7: Real component of the synthetic time-domain molecular response .....	20
Figure 8: Placzek and teller factors.....	22
Figure 9: Herman Wallis factor.....	23
Figure 10: Boltzmann population distribution at 300K and 2500K.....	23
Figure 11: Comparison of the (a) CARS and (b) CSRS processes.....	24
Figure 12: Comparison of the (a) resonant and (b) non-resonant contributions to CARS .....	25
Figure 13: Non-resonant referencing. ....	26
Figure 14: A positively chirped pulse in the time domain.....	28
Figure 15: Producing chirp using dispersive material .....	28
Figure 16: Time-resolved CARS .....	30
Figure 17: Comparison of rotational Hybrid and CPP CARS approaches.....	31
Figure 18: Interaction of the CPP with the molecular response at different time delays .....	32
Figure 19: Current hybrid fs/ps CARS setup.....	33
Figure 20: Working of the SHBC.....	35
Figure 21: 4F filter design .....	36
Figure 22: Comparison of the direct probe output of the SHBC to a Gaussian profile .....	38
Figure 23: Best fit for nitrogen CSRS spectra at room temperature .....	39
Figure 24: Time-domain probe pulses .....	40
Figure 25: Experimental hydrogen CARS spectrum (first two lines) at room temperature .....	40
Figure 26: Synthetic molecular response of pure hydrogen at 300K.....	41
Figure 27: Experimental hydrogen CARS spectrochronogram at room temperature .....	41
Figure 28: Experimental hydrogen CARS spectrum (slit open) at room temperature .....	42
Figure 29: Experimental hydrogen CARS spectrochronogram (slit open).....	42
Figure 30: Experimental nitrogen CSRS spectrochronogram at room temperature (slit closed) .....	43
Figure 31: Experimental nitrogen CSRS spectrochronogram at room temperature (slit open).....	44
Figure 32: Pure $H_2$ CARS at room temperature (experimental) (slit closed) .....	45
Figure 33: Pure $H_2$ CARS at room temperature (experimental) (slit open).....	45
Figure 34: Resonant CSRS spectra from air at room temperature with a low signal .....	46
Figure 35: Shot-to-shot precision and overall accuracy of the fitted temperature with a low signal ...	47
Figure 36: Resonant CSRS spectra from air at room temperature recorded with a high signal .....	47
Figure 37: Shot-to-shot precision and overall accuracy of the fitted temperature with a high signal ..	48
Figure 38: Comparison of the reconstructed probe profile using discretized frequency data .....	50
Figure 39: Nitrogen spectra at room temperature recorded using probes at different slit positions .....	50
Figure 40: Simulation of the time-domain response to the filter in the Fourier plane .....	52
Figure 41: Method of correlation of non - resonant signal intensity .....	53
Figure 42: Fluctuation of the non - resonant signal shot - to - shot .....	53
Figure 43: Fluctuation of the redesigned non - resonant signal shot-to-shot.....	54
Figure 44: The temporal shape of the probe pulse obtained from the correlation (main lobe).....	55
Figure 45: The temporal shape of the probe pulse obtained from the correlation (sidebands).....	56
Figure 46: Flowchart of the phase and relative intensity information flow .....	57
Figure 47: Working of the time-domain interferogram model .....	57
Figure 48: Comparison of the time- and frequency-domain representations of the pulse.....	58

Figure 49: Comparison of room temperature nitrogen CSRS spectrochronograms.....	59
Figure 50: Comparison of nitrogen CSRS spectra at room temperature.....	59
Figure 51: Two objectives to minimize .....	60
Figure 52: A Pareto front formed from the minimization of the two objectives. ....	61
Figure 53: One repetitive period of the nitrogen CSRS spectrochronogram .....	61
Figure 54: A Pareto surface generated from the minimization of three objectives .....	62
Figure 55: Design parameters per discretized frequency .....	62
Figure 56: Synthetic windows placed on the experimentally recorded probe spectra.....	63
Figure 57: The best fit of nitrogen CSRS spectra at room temperature and an arbitrary delay. ....	64
Figure 58: Flowchart of the steps in the Genetic algorithm from start to finish.....	64
Figure 59: Spectrogram of the synthetic probe pulse .....	65
Figure 60: Comparison of the time- and frequency-domain representations of the probe pulse. ....	66
Figure 61: Comparison of nitrogen CSRS spectrochronograms at room temperature.....	67
Figure 62: Comparison of nitrogen CSRS spectra at room temperature, probe delay = 26.76 ps.....	67
Figure 63: Comparison of nitrogen CSRS spectra at room temperature, probe delay = 29.02 ps.....	68
Figure 64: Comparison of nitrogen CSRS spectra at room temperature, probe delay = 31.52 ps.....	68
Figure 65: Best fit for nitrogen CSRS spectra at room temperature at a probe delay of ~43.53 ps .....	69
Figure 66: Comparison of Air CSRS spectrochronograms at room temperature (slit closed).....	70
Figure 67: Comparison of Air CSRS spectrochronograms at room temperature (slit open) .....	70
Figure 68: The $H_2/N_2$ .....	71
Figure 69: Temperature fit at the center of a hydrogen diffusion flame .....	72
Figure 70: Temperature fit at the center of a hydrogen diffusion flame .....	73
Figure 71: Temperature fit at the center of a hydrogen diffusion flame .....	73
Figure 72: Temperature fit 3mm away from the flame front of a hydrogen diffusion flame .....	74
Figure 73: Temperature fit 3mm away from the flame front of a hydrogen diffusion flame .....	75
Figure 74: Spectral content in the laser pulses.....	78
Figure 75: Intensity of the laser pulse-to-pulse .....	79
Figure 76: Shift in the spectrum of the probe with changes in the SHBC.....	80
Figure 77: Spectral coincidence of the higher frequency photons from the probe .....	80
Figure 78: Absence of spectral coincidence of the lower frequency photons.....	81
Figure 79: Non-resonant signals from the slit open and slit closed case compared .....	82
Figure 80: Synthetic computation of the non-resonant signals.....	82
Figure 81: Arrival times resulting from the measurement of the time-domain profile .....	84



# Summary

With the ongoing battle against climate change, new technologies are being proposed in response to stringent rules by governments and companies in a worldwide attempt to reduce emissions from commercial aircraft. The gas turbine engine is a matured technology and the combustion powering the engine seems to be irreplaceable for the foreseeable future. Laser diagnostics form a crucial part of the venture into identifying potential reductions, and the CARS (coherent anti-Stokes Raman scattering) diagnostic technique has become a gold standard in temperature and species concentration measurements in flames. CARS is a complex light-matter interaction process, that takes advantage of the fact that the interaction of the electromagnetic (laser) fields with molecules allows for the direct measurement of their Boltzmann distributions and energy values that are specific to different species of molecules. Hybrid femtosecond/picosecond (fs/ps) coherent anti-Stokes Raman spectroscopy (CARS) is a powerful laser diagnostic technique for thermometry and concentration measurements in chemically-reacting flows. This technique employs ultrashort laser pulses to perform frequency- and time-resolved measurements: fs-duration pump and Stokes pulses excite modes of “Raman-active” molecules, whilst a ps-duration probe pulse is coherently scattered from the molecules on a time-scale much lower than that of molecular collisional processes.

In recent years, the use of SHBC (second-harmonic-bandwidth-compression) to generate the ps probe pulse is taking hold in fs/ps CARS systems, owing to its simplicity, robustness, and relatively large conversion efficiency (~30%). However, the often presence of imperfections in the optical conversion processes employed in SHBC results in the generation of sidebands in the compressed pulse spectrum. The presence of these spectral sidebands in the probe pulse determines a significant additional modulation of the CARS spectrum, which prevents meaningful comparison to typical time-domain CARS models. A common solution to this issue is to employ a 4F-filter, to clean the spectrum of the ps pulse output by the SHBC: this can result in a loss of up to ~70% of the probe pulse energy. This filtering can thus adversely impact CARS thermometry, especially in high-temperature environments, where the number density of the molecular scatterers is small. In this respect, fs/ps CARS thermometry performed with probe pulses generated via SHBC can greatly benefit from a thorough investigation of the spectrochronographic properties of the ps pulses, allowing to operate the system without a 4F-filter. In this work, the ps pulse generated by the SHBC is characterized through frequency- and time-correlation measurements: its spectrum is discretized and the relative phase of each spectral segment is determined by measuring its arrival time, relative to the carrier frequency of the pulse. Here, the fs pump/Stokes pulse is employed as an active temporal gate to perform these time-correlation measurements. The phase information thus achieved is further tuned using a tailored genetic algorithm, to improve the fit quality.

With this information secured, the CARS signal can be modeled using existing models for the molecular response generated by the pump/Stokes pulse – varying depending on the concentration and temperature – and the probe pulse, which is now a characterized constant. The resulting synthetic CARS model is capable of rendering the additional modulation of the experimental CARS spectra owing to the presence of the spectral sidebands in the probe pulse. It was then used to perform CARS thermometry in a laminar hydrogen/air diffusion flame, where the accuracy and precision of the recorded temperature were within good margins to those predicted by the regular filtered probe pulse.

# 1

## Introduction

The climate is changing, and the world is getting warmer every year. The net positive radiative forcing in the atmosphere has been traced back and attributed to the CO<sub>2</sub> and NO<sub>x</sub> emissions dating back to the 1750s [1]. Aviation emits a very high amount of CO<sub>2</sub> per passenger-kilometer, although it contributes only a small (3-5%) amount to the net global radiative forcing. The impacts of emission of water and CO<sub>2</sub> at higher altitudes on radiative forcing are more pronounced, however, and the NO<sub>x</sub> content in the emissions from aircraft is harmful for living beings to ingest.

The International Civil Aviation Organization has initiated the Carbon Offsetting and Reduction Scheme for International Aviation (CORSIA). This policy could stimulate the demand and production of sustainable aviation fuels, while also reducing air travel growth by increasing airfare. This will take effect in 2021 and aims to reduce aviation carbon emissions [2]. According to the goals set by the Advisory Council for Aviation Research and Innovation in Europe (ACARE), the NO<sub>x</sub> emission levels in 2050 must only be 10% as compared to a baseline aircraft of the year 2000 [3].

Alternatives to fossil fuels as the main energy carrier are not yet viable for use in aviation. Airlines have responded to the CORSIA and ACARE goals by taking measures through various means, including the gradual introduction of sustainable fuels and the continuous reduction in fuel consumption of aircraft. These innovations in engineering require an in-depth knowledge of the relevant scientific processes. One of the most important regions of focus is the combustion inside the modern turbofan engine.

Combustion is the most common energy generation process present in almost all automobiles, and aircraft. The combustor is also where emission is produced. The design of next-generation combustors increasingly relies on complex numerical combustion and flow simulations. Accurate models can have a direct impact on their polluting species and fuel consumption. For example, the CFD technique, Large-eddy simulation (LES), has gained importance in describing turbulence [4]. In such schemes, modeling is required for processes that cannot be resolved (at the sub-grid scale, for example, in LES). The validation of these models using reliable and comprehensive experimental data is then a crucial part of the development of combustion-LES [4]. Experiments have always been essential for advances in computational modeling, by providing data for validation and measuring realistic boundary conditions for numerical studies [5].

The combustion chambers in modern turbofan engines achieve very high pressures and temperatures in reaction zones with turbulent mixing, where the heat release from numerous chemical-reactions-dominated instabilities develop, grow, and interact at frequencies of 1–10 kHz or greater. In such reaction zones, spatially and temporally resolved temperature and multi-species concentration measurements can provide critically valuable data for the validation of multidimensional turbulent combustion models. These models can then be

utilized to optimize the respective combustion and energy-transfer processes and minimize the release of harmful pollutants from those combustors [6].

Laser diagnostics are a well-established cornerstone of experimental combustion research. They enable measurements of flames without the need for intrusive sampling probes such as thermocouples which disturb the flow field of a flame and may have additional catalytic effects [7]. In-situ measurements are possible using light as the probing medium, which does not occupy space and is the fastest information carrier known, making it more trustworthy with true in-situ capability. There are well-established techniques for the remote spatially and temporally resolved probing of temperature, velocity, and a variety of chemical species in instrumentally hostile environments typical of practical combustion and plasma devices [8], where the use of physical probes is difficult, if not impossible. The fundamentals of combustion are complex, and accurate experimental data can go a long way to bolster the understanding of its intrinsic properties. Laser-based measurements can provide data encompassing a broad range of spatial and temporal scales of flames [5].

The work presented here attempts to develop a relatively recent, but well-established experimental technique in laser spectroscopy that can be used to image temperature and species concentrations fields in flames with extremely high precision and accuracy – CARS (Coherent Anti Stokes Raman Spectroscopy). The first part of this report sets up the necessary theoretical content behind CARS and inherent light-matter interaction (Chapter 2) and distinguishes the two main approaches to performing CARS: time- and frequency-resolved measurements. Then, the experimental setup at the Advanced Laser Diagnostics and Flame laboratory at TU Delft is presented (Chapter 3), and a research objective is posed (Chapters 4). The subsequent part then discusses the methodology of answering research questions (Chapter 5) formed sequentially, to achieve the research goal and then discusses the results (Chapter 6).

# 2

## Theory of CARS

The theoretical content of the work is heavily focused on the CARS process and its inherent non-linear light-matter interactions. The molecular physics involved is critically important and its understanding will contribute to finding novel ideas to improve the CARS technique effectively.

### 2.1 Non-linear light-matter interaction

At the location of the interaction of one or more electric fields (such as contained in light, which is an electromagnetic wave), a dipole moment is generated on a microscopic (molecular) scale. The polarizability of a molecule ( $\alpha$ ) relates the polarization ( $\tilde{p}$ ) produced through the generated dipole moment (single molecule) to the electric field (e.g. laser light) that induces it ( $\tilde{E}$ ), as shown in equation 1, where  $\epsilon_0$  is the permittivity of free space. Such microscopic dipoles (i.e. the single molecules) result in a macroscopic optical susceptibility of the medium,  $\chi$  and, a macroscopic polarization,  $\tilde{P}$  when considering a large number of molecules,  $N$ . In nonlinear optics, the optical response can often be described by expressing the polarization field  $P(t)$  for a macroscopic region, as a power series in the field strength  $E(t)$  as can be seen in equation 2, where the quantities  $\chi^1, \chi^2$  and  $\chi^3$  are the linear, second-order, and third-order nonlinear optical susceptibilities respectively.

$$\tilde{p} = \alpha * \tilde{E}, \quad \text{and}, \quad \tilde{P} = N\tilde{p} = \epsilon_0 * \chi * \tilde{E} \quad \text{Eq. 1}$$

$$\overline{P(t)} = \epsilon_0 * [\chi^{(1)} * \overline{E^1(t)} + \chi^{(2)} * \overline{E^2(t)} + \chi^{(3)} * \overline{E^3(t)} + \dots] \quad \text{Eq. 2}$$

Spectroscopy can be classified as the study of the wavelength dependence of the absorption or any other interaction of light with matter and CARS is inherently a non-linear spectroscopic process. Nonlinear optics is the study of phenomena that occur because of the modification of the optical properties of a material system by the presence of light. Typically, only laser light is sufficiently intense to modify the optical properties of a material system. Nonlinear optical phenomena occur when the strength of an optical field and the response of a material system to the applied optical field are related in a nonlinear manner [9]. For example, both sum-frequency generation and second-harmonic generation occur as a part of the response of a molecule (dipole moment, discussed below) that scales quadratically with the strength of the applied optical field. This is possible due to the interaction between two fields (at the molecule) in generating the SHG signal, as shown in figure 1, and is a second-order non-linear spectroscopic process. A common apparatus called the Second Harmonic Bandwidth Compressor (which is important to this project, and is discussed later) uses sum-frequency generation to convert broadband pulses to a higher (narrowband) frequency. Sum frequency generation (SFG) and second harmonic generation (SHG) differ in the type of photons being consumed (Light can be discussed both as a particle and a wave depending on the subject,

and photons are generally used to describe the interaction of a quantized field interacting with quantized energy gaps in molecules). The SHG process uses two photons of the same frequency, while this is not a requirement for the SFG process. It is interesting to note that all second-order processes occur in photonic crystals, as isotropic media (such as gas-phase media) do not possess second-order susceptibility. The SFG in the SHBC also takes place in a special photonic crystal (BBO crystal).

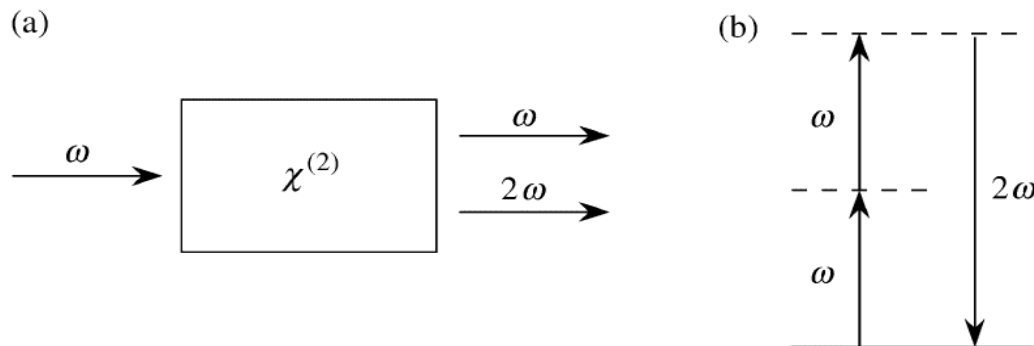


Figure 1: (a) Second-harmonic generation: depicting frequency conversion.  $\chi^{(2)}$  shows the second order nature of the medium. (b) The dashed lines represent virtual states and solid lines represent real energy states of the molecule in the medium. Each arrow represents a photon which takes the molecule to a higher energy state. [9]

## 2.2 Four-wave mixing and CARS

Four-wave mixing processes all derive their name from the principle of three electromagnetic fields interacting to produce a fourth electromagnetic field. The first electromagnetic field, when applied to the dielectric medium, induces an oscillating polarization that then re-radiates with some phase shift determined by the damping of the individual dipoles in the dielectric. This can easily be represented by linear optics and is commonly referred to as Rayleigh scattering. Now, a second applied electromagnetic field will also impact the polarization of the dielectric, and the interference of the two waves (depending on their frequencies) will cause harmonics in the polarization at the interaction (sum and difference) frequencies. The application of a third electromagnetic field will now make the polarization beat with both the other input fields as well as the many possible harmonics (sum and difference frequencies).

$$\omega_4 = \omega_3 \pm \omega_2 \pm \omega_1 \quad \text{Eq. 3}$$

This beating with the sum and difference frequencies is what gives rise to the fourth field in four-wave mixing, and the interaction is a third-order non-linear spectroscopic process. Since each of the beat frequencies produced can also act as new source fields, many interactions and fields may be produced from this basic process [10].

The CARS process is a clear example of four-wave mixing (Figure 2, left) that uses two laser pulses termed the pump ( $\omega_{pump}$ ) and Stokes ( $\omega_{Stokes}$ ) and a third narrowband laser pulse termed the probe ( $\omega_{probe}$ ). The CARS signal hence scales with the intensity of each electric field (Third-order).

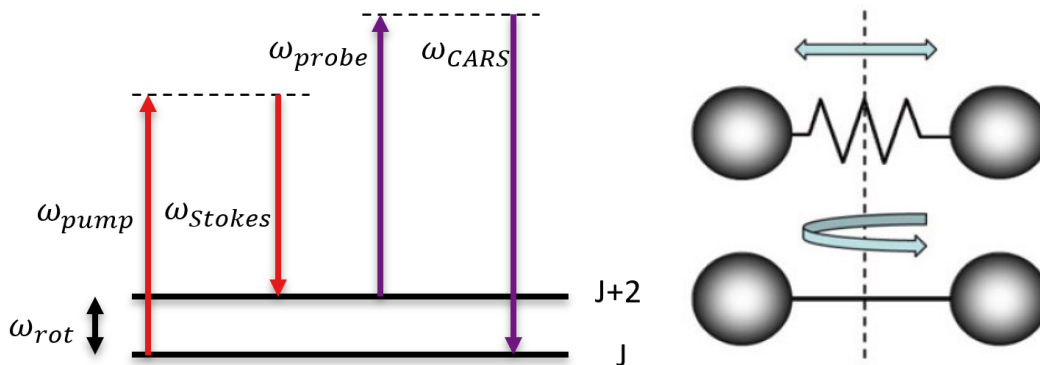


Figure 2: (Left) The third-order nonlinear CARS process is visualized. The dashed lines represent virtual states and solid lines represent real energy states of the molecule in the medium. Each arrow represents a photon (quantization of the field) that takes the molecule to a higher energy state ( $J \Rightarrow J+2$ ).  $J$  is the rotational quantum number. (Right) Vibrational (top) and rotational (bottom) degrees of freedom in the diatomic molecule. The bond between two atoms in nitrogen for example can rotate around or vibrate about its center of mass. [11]

The pump and Stokes beams together first arrive and establish resonance (a harmonic in the polarization of the molecule with this particular energy gap) between the ground state and an excited vibrational or rotational state of a Raman active molecule ( $\omega_{vib}$ ). This prepares a coherence due to the resonant excitation (and due to the coherence of the incoming beams) and forms the molecular response of the medium, which is explained more in detail in the following section. The probe beam is then scattered off these molecules and the change in its frequency ( $\omega_{CARS} - \omega_{probe}$ ) due to the coherent inelastic scattering process can be recorded by a spectrometer and analyzed to obtain species and temperature measurements (see next chapter on the experimental setup).

As shown in Figure 2 (Right), the molecule to be excited can be visualized as a harmonic oscillator (Vibration, top in the figure) or a rigid rotor (Rotation, bottom in the figure), and the energies in the respective vibrational or rotational states are quantized within the molecule [11] as shown in Figure 3. From this diagram it can be seen, the increasing bond length, with the vibrational and rotational quantum numbers. The harmonic and anharmonic (Morse) potentials describe the ro-vibrational energy of the diatomic molecule as a function of the equilibrium internuclear distance. It is also important to note that at higher energies, the molecule attempts to vibrate stronger non-linearly and the average bond length increases. This influences the rotational energies directly and results in rovibrational states. More importantly, at larger distances, the attractive forces between the atom are weak, resulting in an anharmonic potential.

The pump and Stokes photons must reach the molecule simultaneously. As the pump photon is absorbed, the molecule reaches a higher “virtual” energy state for a very short period (quick to dephase). This is the “Born-Oppenheimer approximation”, which states that the motions of the electrons and the nuclei can be decoupled, as they happen on largely different timescales. Hence, the fast-oscillating electric field (at the optical frequency of the pump laser pulse) interacts directly with the electrons, not with the nuclei. This short-living state is commonly referred to as a “virtual state” in literature [12], and the Stokes photon must be incident during this period. According to [7], the pump/Stokes excitation is essentially instantaneous, occurring on timescales of  $10^{-12}$  s or less.

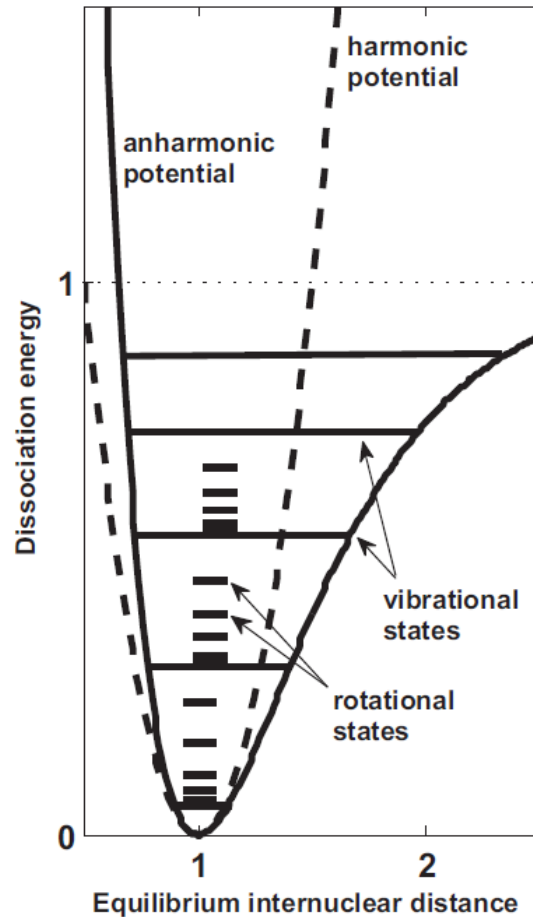


Figure 3: The anharmonic potential containing the quantized vibrational and rotational states for a diatomic molecule. Multiple rotational states exist within a single vibrational energy level. A higher electronic level would be above this, containing its own vibrational and rotational energy levels. [11]

### 2.3 Energy and momentum conservation: Phase-matching

The probe and pump/Stokes pulses need to first be spatially coincident at the probe volume (measurement location and volume of the interaction between the three pulses) to generate a CARS signal. Phase matching is then an important characteristic that contributes to the success of the CARS technique. The CARS process is a four-wave mixing technique that utilizes three input pulses ( $E_1$  – pump,  $E_2$  – Stokes, and  $E_3$  – probe) which must obey the conservation of energy and momentum in the generation of a fourth laser-like pulse ( $E_4$  – CARS). Each pulse can be described as a time-dependent electric field:

$$\vec{E}(\vec{r}, t) = \vec{E}(t) \cdot \exp(i\vec{k}\vec{r} - i\omega t) \quad \text{Eq. 4}$$

Where  $k$  is the wave vector along the propagation direction  $r$ ,  $\omega$  is the frequency, and  $E(t)$  is the pulse envelope of the electric field. The frequency of the generated radiation,  $\omega_4$ , is constrained by conservation of energy as follows:

$$\omega_4 = \omega_1 - \omega_2 + \omega_3 \quad \text{Eq. 5}$$

Where a large increase in signal is observed if  $\omega_1 - \omega_2$  is resonant with a rotational transition in a sample molecule. The same conservation of momentum can also be written as:

$$k_4 = k_1 - k_2 + k_3 \quad \text{Eq. 6}$$

The energy and direction of the signal beam,  $k_4$ , is then governed by the incoming wave vectors by what is termed as the Phase-matching condition [13].

For gases that are nearly dispersion-less, phase matching occurs when the beams are collinearly mixed. Although easy to implement, collinear phase matching possesses several drawbacks from a diagnostic standpoint. Since the CARS signal is coherent and represents an integrative effect, the spatial resolution cannot be well defined by imaging techniques. Collinear phase matching can then result in poor and often ambiguous spatial resolution. In [14], a crossed-beam phase-matching technique is demonstrated, primarily intended for gas-phase diagnostics. The technique leads to unambiguous spatial resolution, is versatile, and greatly enhances the utility of CARS for spatially precise diagnostic applications. BOXCARS is a different phase-matching technique that was developed to ensure phase-matching is preserved along with maintaining spatial resolution. And, as is visible from Figure 4 (bottom), BOXCARS needs individual control on the three independent laser beam directions. Some vibrational CARS techniques are performed using the BOXCARS approach [15], [16] [17]. BOXCARS is impossible for the current experimental setup and is discussed in chapter 3.

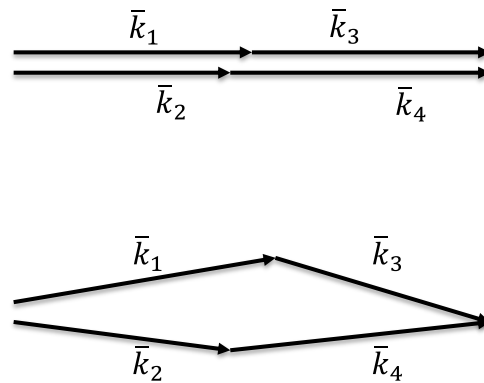


Figure 4: CARS phase-matching approaches: (top) collinear, (bottom) crossed beam or BOXCARS.

## 2.4 Time-domain representation of the (rotational) Raman response

For CARS, the difference  $\omega_{pump} - \omega_{stokes}$  is tuned to match the wavelength of molecular vibrational and/or rotational resonances. This thesis deals with pure rotational CARS, which means only the rotational transitions are looked at, by the excitation from the pump/Stokes photon pair. The different rotational transitions for nitrogen at room temperature are shown in figure 5.

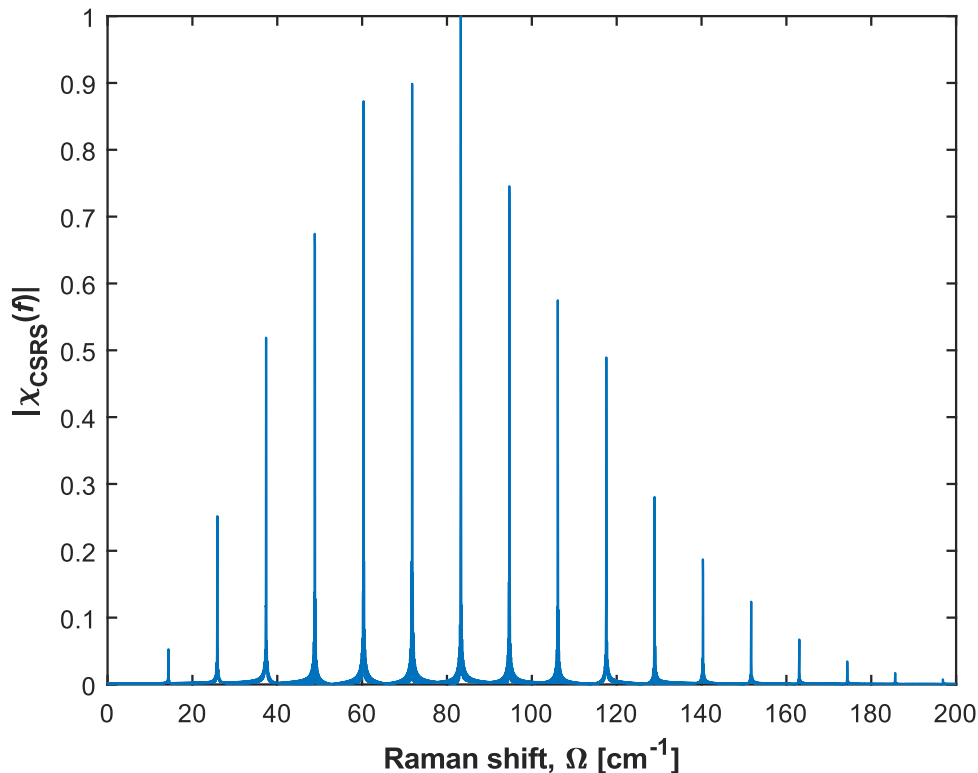


Figure 5: Synthetic frequency domain molecular response for nitrogen gas at 300K (Simulation). X-axis: Raman shift – change in the probe photon frequency after the interaction with the molecule.  $\chi_{CARS}$  is the third order susceptibility induced in the medium.

When the probe pulse scatters inelastically off the Raman-active molecules, if the molecules are in a coherent rotational/vibrational state (as set up by the pump and Stokes pulses), the radiation produced by the probe scattering is coherent as well. This separates coherent Raman spectroscopy from other regimes that use spontaneous Raman scattering, where the signal is generally very weak. For probing in high-temperature gases, the coherent preparation of molecules includes a great increase in the observed signal strength, leading to better data for thermometry. “Impulsive excitation” is an excitation process that (on a macroscopic scale) happens at a timescale much shorter than the characteristic period of the Raman mode excited (this can be compared to the time it takes for the simplified model of the nuclei to rotate). If the excitement of the rotational resonances is impulsive, meaning that the different Raman modes have a collective starting point, the coherence in the medium is maximized, also leading to a stronger CARS signal.

Figure 5 also shows the relative intensities between different rotational transitions for nitrogen at room temperature. This depends on a multitude of factors but generally indicates that some are more probable than others, and this is partly due to selection rules governing these probabilities. First, a selection between Raman scattering and other forms of scattering needs to be established. Infrared spectroscopy, for example, deals with the interaction between matter and infrared radiation by either absorption or emission. Efficient absorption-based spectroscopy (such as IR spectroscopy) is typically limited to heterogeneous diatomic species such as NO, OH, and CH because it requires a permanent dipole moment. Raman spectroscopies such as CARS, however, are highly effective for investigations of symmetric stretches or rotational transitions in symmetric molecules such as  $N_2$ ,  $O_2$ , and  $CO_2$  [14]. There are several useful generalities concerning Raman and IR spectroscopy: Symmetric vibrations lead to relatively strong Raman signals and no IR signal. Asymmetric vibrations lead to much weaker Raman signals and are often quite strong in IR spectroscopy. Bending vibrational modes lead to much weaker Raman signals and are often quite strong in IR spectroscopy. A

molecule can have both IR and Raman signals at the same frequency, though if the Raman signal is strong, the corresponding IR peak will be weak and vice versa.

When talking of Raman scattering, the vibrational and rotational energies are often represented by respective quantum numbers,  $(\nu, J)$ , which have further selection rules. The Raman scattered signal (now affected by the rovibrational motion of the molecule) can be separated into three branches (for diatomic molecules) in the frequency spectrum, the  $Q$  ( $\Delta J = 0$ ) branch that contains vibrationally shifted transitions, and the  $O$  ( $\Delta J = -2$ ) and  $S$  ( $\Delta J = +2$ ) branches that are rotationally shifted, where  $J$  denotes the rotational quantum number of the molecule. The  $O$  and  $S$  branches are, respectively, blue-shifted, and red-shifted from the probe carrier frequency and correspond to anti-Stokes and Stokes pure rotational Raman scattering [13], while the  $Q$  branch corresponds to a pure vibrational transition involving no change in  $J$ . The probabilities of each of these transitions occurring are discussed in the following section. For molecules that are not diatomic, selection rules allow for  $P$  and  $R$  branches as well. On the high-frequency side of the  $Q$ -branch, the energy of rotational transitions is added to the energy of the vibrational transition. This is known as the  $R$ -branch of the spectrum for  $\Delta J = +1$ . The  $P$ -branch for  $\Delta J = -1$  lies on the low wavenumber side of the  $Q$  branch. However, this work focuses only on pure rotational CARS.

### 2.4.1 Molecular Response

Once the many Raman transitions are created in the vibrational/rotational manifold by the pump/Stokes interaction, they begin to oscillate at their natural frequencies. These individual frequencies, beating together, start exhibiting interference patterns and start to dephase (due to destructive interference between them) after the initial coherence. Consequently, this also induces destructive interference in the contribution to the resonant CARS signal [15] and is called frequency-spread dephasing, like the theory of beating of waves. This decay of the coherence is shown in figure 6 (displaying data from vibrational CARS) and is characteristic due to the consistent starting point of all the driven Raman transitions. How this impulsive excitement is achieved experimentally, is explained later in the chapter on the experimental setup.

With an increase in temperature, more rotational transitions are present in the manifold due to higher energy levels being populated (Boltzmann distributions, discussed later), and the dephasing is hence quicker. This “pure” dephasing (due to the bandwidth of the resonant signal, discussed with the transform limit theorem later) also leads to revival structures whenever the Raman dipoles constructively interfere. For a nitrogen pure rotational manifold, generated at 300K, a full revival peak occurs at around  $\sim 8.4$  picoseconds and a half revival occurs at  $\sim 4.2$  picoseconds. This can be seen in the molecular response for nitrogen at 300K in Figure 6. From this figure, it is also evident that the overall signal decays over time, slower than the initial frequency spread dephasing (which leads to revival structures in the response). This is because of multiple reasons. First, with time, the probability of perfectly rephasing the individual coherences to form the revival peaks decreases. Hence each revival peak is lower in amplitude than the one before.

These molecules are also bound to collide with each other, at a rate directly proportional to pressure and inversely to temperature (according to the gas law). These collisions can be elastic or inelastic. Elastic collisions do not change the energy state of the affected molecules but induce a loss of molecular coherence. This phenomenon is known as “quantum decoherence” and results in the reordering, and hence loss, of energy. In [16], the mechanisms behind this quantum decoherence in the time-resolved CARS spectra (described in [section 2.8](#)) of molecules in liquids are clarified. Inelastic collisions end up exchanging energies between molecules and destroying the molecular coherence. For example, for nitrogen at 300K and 60 atm, the collisional dephasing time is about 15 ps [17]. This dephasing

can be represented synthetically by including a decay-dependent spectral linewidth into the molecular response for frequency-resolved measurements,  $\Gamma$ , which impacts how wide the lines are in figure 4. For time-resolved measurements, which is the focus of this work, the decay information is compiled into dephasing coefficients that describe the same in the time domain.

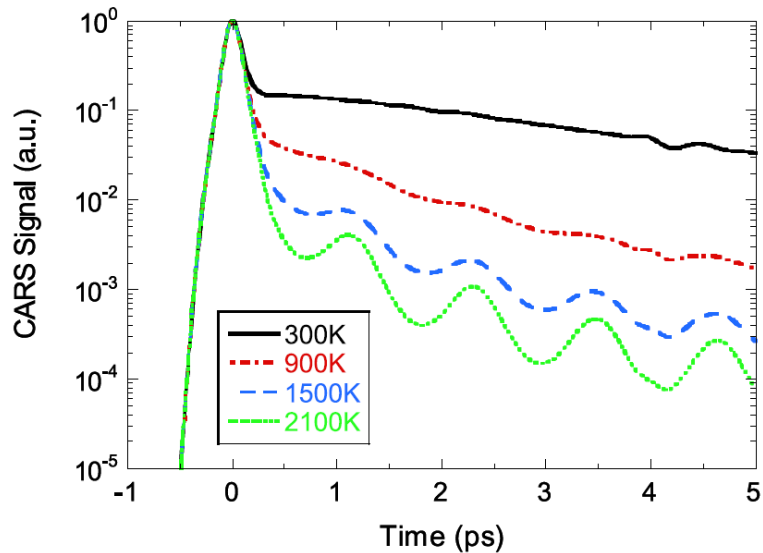


Figure 6: Frequency spread dephasing and its temperature dependence, as depicted in [15]. The time-domain data shown here contains information on vibrational transitions of  $N_2$ . Higher temperatures decay faster due to the larger number of Raman frequencies in the manifold (from the population of higher energy levels).

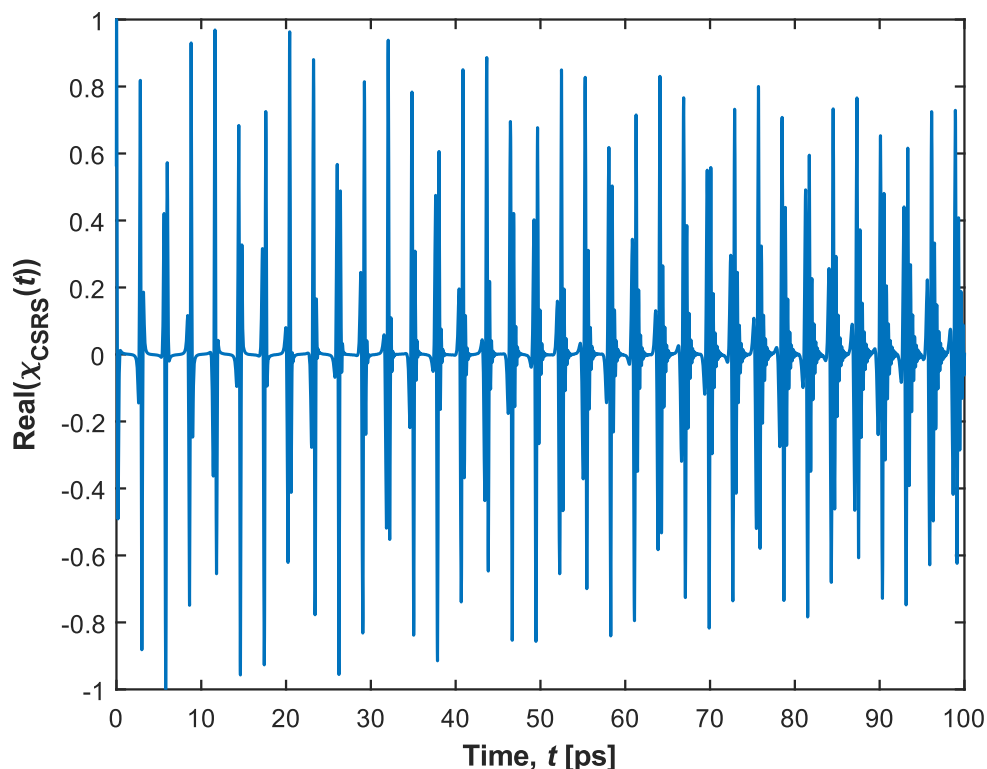


Figure 7: Real component of the synthetic time-domain molecular response for  $N_2$  at 300 K, with evident exponential decay over 100 ps and pure dephasing leading to revival peaks in the response with a period of  $\sim 8.4$  ps (Simulation).

### 2.4.2 Time-domain modeling

The molecular response,  $\chi^3(t)$ , further depends on multiple parameters, which are detailed below:

$$\chi_{CARS}^3(t) = \sum_k \sum_v \sum_{\Delta J=+2} \left( X_k \cdot \gamma_k^2 \cdot F_{J \rightarrow J+2}^{(k)} \cdot b_{J \rightarrow J+2} \cdot \left( N_{J+2}^{(k)} - N_J^{(k)} \right) \cdot \exp \left[ \left( i \cdot \omega_{v, J \rightarrow J+2}^{(k)} - \Gamma_{J \rightarrow J+2}^{(k)} \right) \cdot t \right] \right) \quad \text{Eq. 7}$$

Here,  $\chi^3(t)$  represents the third-order susceptibility induced in the medium as a function of time, (t). k denotes the  $k_{th}$  chemical species in the gas mixture; v is the vibrational quantum number, which denotes the vibrational state of a molecule. J is the rotational quantum number.  $\Delta J$  denotes a change in the rotational quantum number, i.e., a rotational transition (S-branch in the present case).  $X_k$  is the mole fraction of the  $k_{th}$  species.  $\gamma_k^2$  is the polarisation anisotropy of the  $k_{th}$  species.  $F_{J \rightarrow J+2}^{(k)}$  is the Herman-Wallis factor for a molecule of the  $k_{th}$  species undergoing an S-branch transition.  $b_{J \rightarrow J+2}$  is the Placzek-Teller coefficient for an S-branch transition.  $N_J^{(k)}$  is the Boltzmann fraction for the rotational energy level J of the  $k_{th}$  species.  $\omega_{v, J \rightarrow J+2}^{(k)}$  is the Raman frequency for the rotational transition of a molecule of the  $k_{th}$  species, from the quantum state  $|v, J\rangle$  to the state  $|v, J+2\rangle$ .  $\Gamma_{J \rightarrow J+2}^{(k)}$  is the linewidth of the spectral line corresponding to the rotational transition considered, which contains the dephasing information of the particular transition and for the particular species, which further depends on all the species that may collide with it (For example, a nitrogen molecule is perturbed by all the different species in the medium, and this cumulative perturbation information would need to be modeled in the collisional dephasing constant, and hence linewidth, of nitrogen at the particular J number. The significant parameters involved in Equation 7 are explained subsequently.

Each of the S, Q, and O branch transitions can occur depending on the rotational quantum number of the initial state, J. The relative strengths between the three branches are given by Placzek and Teller factors which are inherently probabilities of each transition [18]. It can be seen from Figure 7 that at lower values of J, the S branch dominates due to the higher probability of a transition to a higher J state. For J values of 0 and 1, reducing the total angular momentum of the molecule by  $\Delta J = -2$  is not possible and hence, the Placzek-Teller coefficient for O (J = 0) and O (J = 1) is zero, and these transitions do not exist in the Raman spectrum. The S-branch and O-branch spectra have the same number of lines, but their parametrization with the initial J-value is different. This means that S (J = 0) and O (J = 2) represent the same transition on the corresponding side of the spectrum. Furthermore, at any value of J, the three probabilities should sum to unity. Theoretically, at a high enough J, both the S and O branches should both have an equal probability of 3/8 and the Q branch of 1/4).

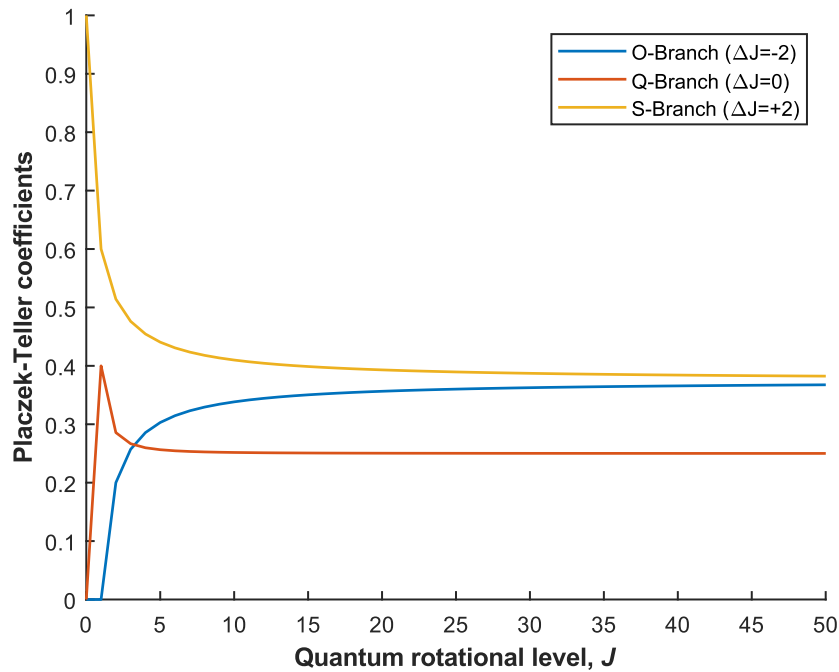


Figure 8: Placzek and teller factors (probabilities on the y-axis) for the three possible transitions (Simulation).

Generally, the rotational energy of a molecule is affected by its vibrational energy and vice-versa. Rigid molecules can rotate and vibrate, and their rigidity infers the ability to change the distance between nuclei or their rotational energies, without affecting each other. Non-rigid molecules are different in that they can tunnel through a potential barrier from vibrational to rotational energies [19]. In the absence of vibration-rotation interactions, however, the relative intensities of the rotational lines in an allowed vibrational transition are given by standard factors, often called Hönl-London factors. The influence of molecular nonrigidity can then normally be represented by correction factors depending on the rotational quantum numbers [20].

The effect of this vibration-rotation interaction is quantified utilizing the Herman-Wallis (HW) factor. Additionally, the centrifugal constant captures the influence of centrifugal force on the intensity of spectral lines. The centrifugal force is responsible for the coupling between vibrational and rotational modes in light molecules and the Coriolis effects are important in making corrections to energy levels in these non-rigid molecules approximated as rigid rotors [21].

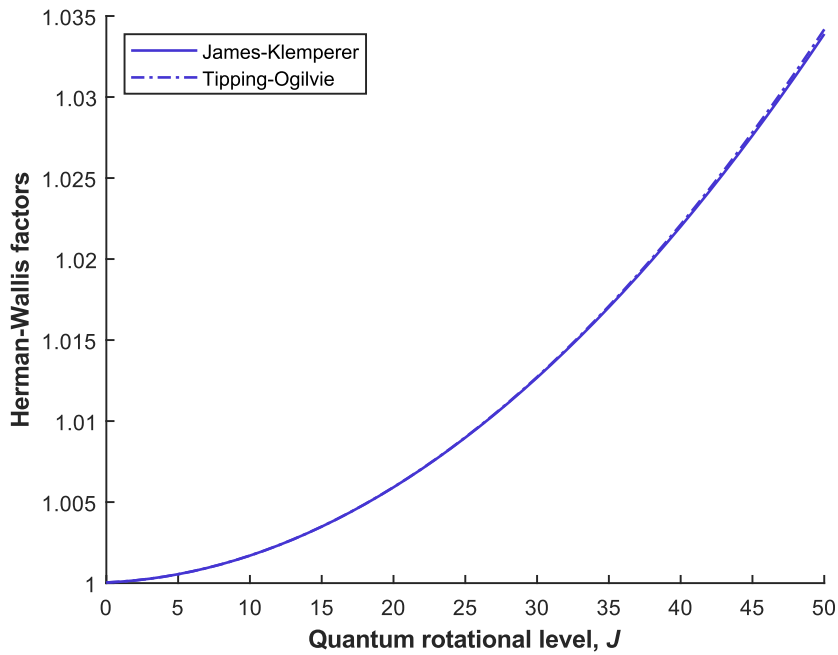


Figure 9: Herman Wallis factor for different rotational quantum numbers for nitrogen (Simulation). The two curves are results from two different models to calculate these factors.

Boltzmann statistics is the pivotal concept behind the success of laser diagnostics in probing temperatures. They describe the population of the different rotational states depending on temperature. Lower  $J$  numbers are populated at lower temperatures and as the temperature increases, higher energies are accessible to be occupied by the molecule (seen in Figure 9). [22] explains the use of these parameters and contains an in-depth explanation of the model development for molecular response generation. In the figure below, a consistent difference in population between even and odd rotational levels can be observed. This is related to the number of degenerate levels (levels with the same energy, but differences in other quantities such as the quantized magnetic spin of the molecule).

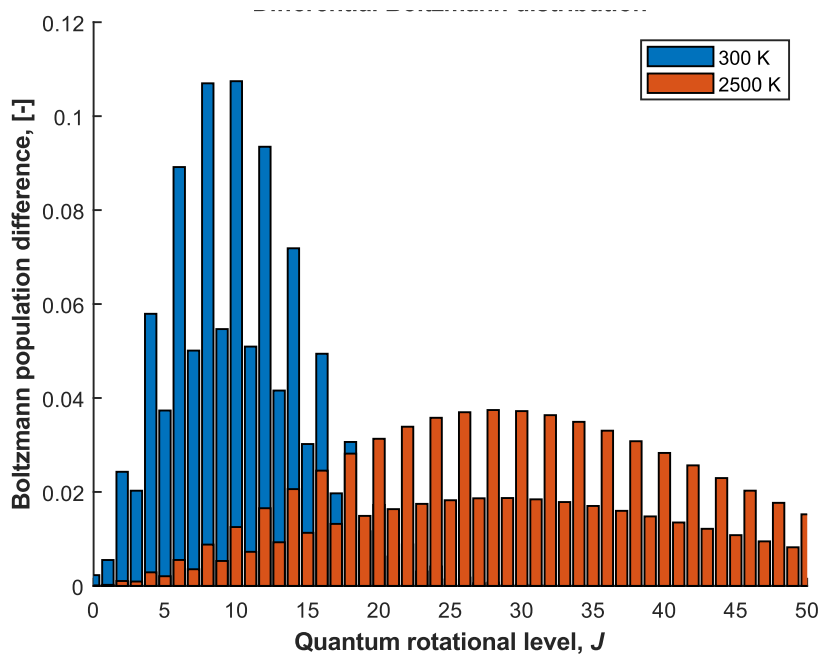


Figure 10: Boltzmann population distribution at 300K and 2500K (Simulation).

## 2.5 CSRS signal (Coherent Stokes Raman Scattering)

If the molecules are excited before the interaction with the probe beam (as is the case with the coherent preparation of molecules by the pump/Stokes photon pair for CARS measurements), they either give up energy to the incident probe photon, upshifting the frequency and scattering them to a lower wavelength or, they take energy from the incident probe photon, downshifting the frequency and scattering them to a higher wavelength. The first process, for historical reasons, is called an anti-Stokes process. The second Raman process is often termed the Stokes process, leading to coherent Stokes Raman spectroscopy [7]. The comparison of the energy diagrams between CARS and CSRS is made in Figure 13.

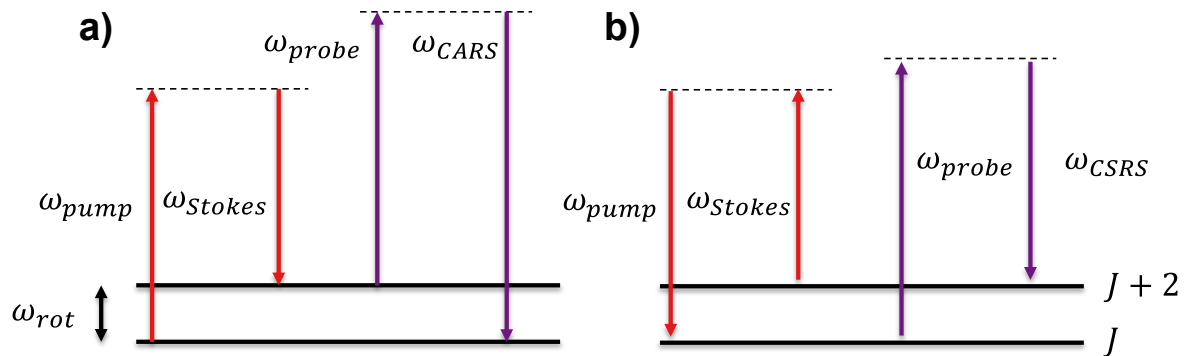


Figure 11: Comparison of the (a) CARS and (b) CSRS processes  $J_2 \rightarrow$  real, excited rot state and  $J_0 \rightarrow$  real, ground state. Dashed lines are virtual states and arrows represent individual photons [12]

The CSRS signal is always present when attempting to work with CARS diagnostics. It is generally dependent on the type of research whether to look at the CARS or the CSRS side of the probe carrier frequency. Coherent Stokes Raman scattering (CSRS) has been largely ignored mainly because it is often strongly affected by fluorescence, particularly for resonance-enhanced measurements [28] (Resonance spectroscopy is an enhancement technique for CARS in which the laser excitation frequency is chosen to match the frequency of an electronic transition of the sample, and as a result increases the Raman scattering intensity). But it can be advantageous to use the CSRS signal for diagnostic purposes. For example, most cameras are designed for the visible wavelength range, and so is the camera in the setup worked on (see the section on experimental setup). The CSRS signal, with the current probe carrier wavelength at  $\sim 402\text{nm}$  (carrier frequency/wavelength corresponds to the fast oscillating field that contains the information in a pulse containing some bandwidth), is closer to this range and could record higher intensities as a result.

## 2.6 Non-resonant signal

While the CARS signal is the most important observable signal, other non-linear interactions of the three incident pulses are also present. The relative intensities and mechanisms of these other processes are well explained in the tutorial by Rigneault [12]. The “non-resonant” signal is another four-wave mixing signal. This scattering process occurs in a non-linear medium, between the three photons when the linear combinations of their frequencies do not correspond to a “resonant” electronic/vibrational/rotational state. The difference between the resonant CARS signal and the non-resonant four-wave mixing is shown in figure 10.

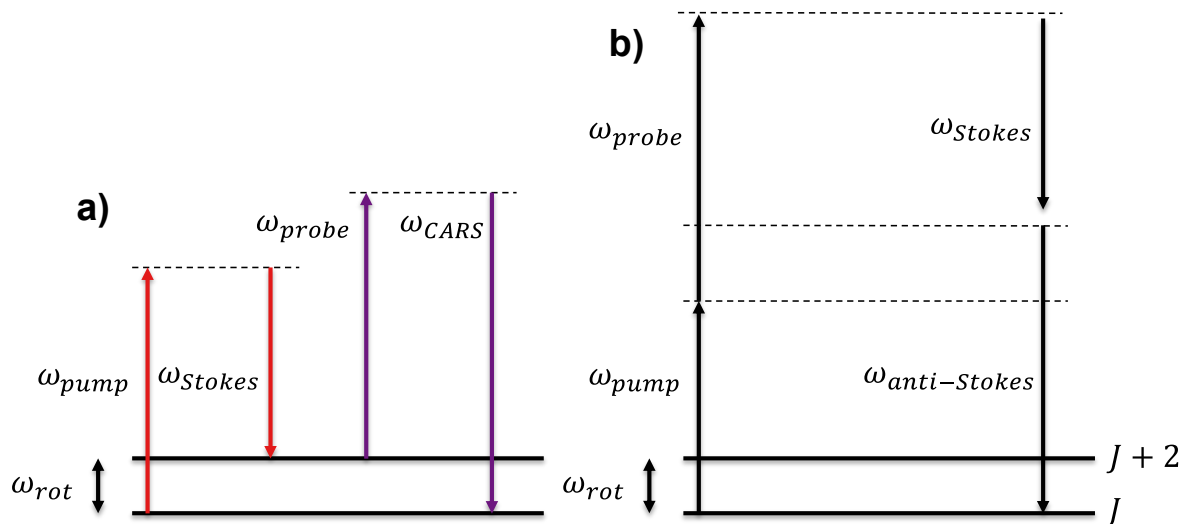


Figure 12: Comparison of the (a) resonant and (b) non-resonant contributions to CARS.  $J_2 \rightarrow$  real, excited rotational state and  $J_0 \rightarrow$  real, ground state. Dashed lines are virtual states and arrows represent photons. [12]

The three probe, pump, and Stokes photons interact with the molecule simultaneously to generate the non-resonant signal. They combine at a specific molecule and elevate it to a higher virtual state. Since the addition frequency  $\omega_1 - \omega_2 + \omega_3$  is not sufficient to reach even the lowest excited electronic state and it does not correspond to any of the vibrational/rotational states, a photon is elastically scattered off at this frequency. With the resonant CARS signal, the interaction of the pump and Stokes pulses leaves the molecule at a higher energy level, which is a “real” energy state of the molecule and hence exists for a sufficient period. However, the three laser pulses must be coincident spatially and temporally to generate the non-resonant signal.

The non-resonant signal must be either filtered out or avoided to observe a clear resonant CARS molecular response. This is because it coincides spectrally with the resonant contributions (see figure 11). Moreover, delayed probing of the Raman coherence enables the elimination of interference from non-resonant four-wave mixing processes due to the necessity of temporal coincidence of the pulses in the case of the non-resonant signal [27]. This is only possible for time-resolved CARS (discussed later), where the time decay of the coherence can be accounted for in their models. Additionally, the generation of the signal also implies the temporal coincidence of the three laser pulses. The non-resonant signal strength scales the same way as the resonant does, implying a linear dependence on each of the probe, pump, and Stokes pulses. This, in turn, allows for the mapping of one of the pulses with another in the time domain. This is of critical relevance to this project and is discussed later along with the chapter on the methodology of probe characterization. The non-resonant signal is also useful to CARS as its measurement (separate, not interfering with the resonant contribution) gives directly the excitation efficiency of the pump/Stokes excitation due to this intensity profile being the frequency domain representation of the convolution product of the pump and Stokes fields (due to the direct intensity dependence). This normalization is shown in figure 12.

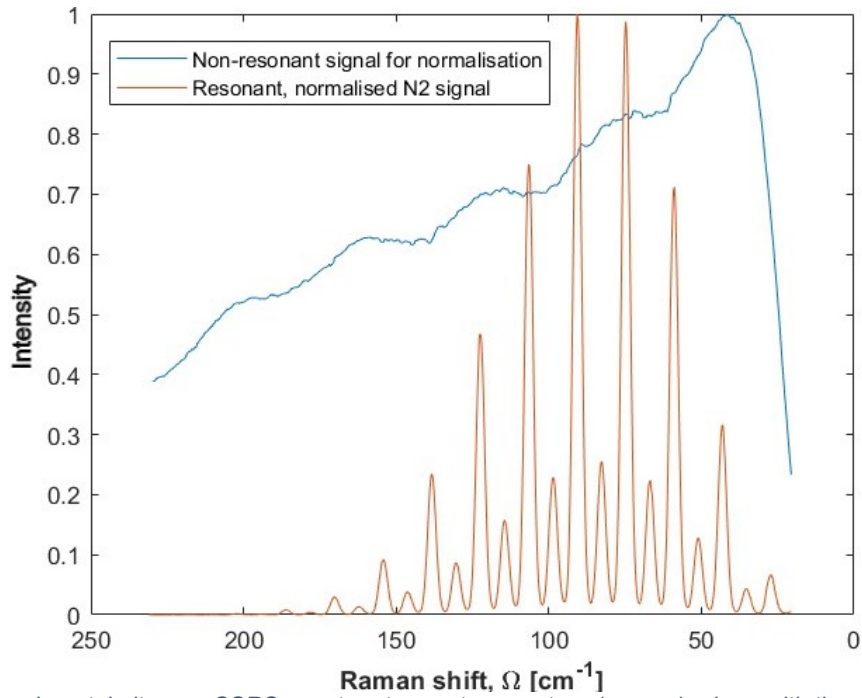


Figure 13: Experimental nitrogen CSRS spectra at room temperature (orange), along with the non – resonant signal used to normalize it (blue). The initial drop at less than  $\sim 40 \text{ cm}^{-1}$  is due to the bandpass filter attenuating the signal (mainly to avoid imaging the probe beam directly on the camera). Both data were recorded on the CSRS side (see next section) with pure  $N_2$ .

## 2.7 CARS signal intensity

The intensity of the CARS signal (also the CSRS and non – resonant signals) at the output is of primary interest in this project and is described by the following equation:

$$I_{CARS}(z) = \frac{16 \cdot \pi^4 \cdot \omega_{CARS}^2}{n^4 \cdot c^4} \cdot I_{pump} \cdot I_{Stokes} \cdot I_{probe} \cdot |\chi^3|^2 \cdot z^2 \cdot \text{sinc}^2\left(\frac{\Delta k \cdot z}{2}\right) \quad \text{Eq. 8}$$

where  $\omega_{CARS}$  is the frequency of the CARS signal,  $I_{pump}$ ,  $I_{Stokes}$  and  $I_{probe}$  are the intensities of the incoming laser beams,  $\chi^3$  is the third-order susceptibility,  $z$  is the interaction length (the length along the region coincident with the multiple lasers), and the  $\text{sinc}^2$  term is a phase-matching condition [11].

An increase in the carrier frequency in the probe also increases the  $\omega_{CARS}$ , and has a direct proportional impact on the strength of the signal. Hence, a higher carrier frequency increases the intensity of the CARS signal output. Moreover,  $I_{CARS}$  is also directly proportional to the number density (of molecules) in the probe volume. And the density  $\propto \frac{1}{\text{Temperature}}$ , which makes it more difficult to observe the signal in flames.

## 2.8 Transform-limit and chirp

The condition of being at the transform limit, coming from the inherent properties of Fourier transform (which relates the time-domain and frequency-domain) is perceived in the form of the minimum pulse duration (or minimum time-bandwidth product, as shown in the equation below) for a given optical spectrum of a pulse. A pulse at this limit is termed to be “transform-limited” and contains a very localized constructive interference between the constituent

frequencies. The time-bandwidth product of this pulse will be at its minimum and the pulse is said to contain no chirp (defined in the next sections) [30].

$$TBP = \Delta\nu \cdot \Delta\tau \quad \text{Eq. 9}$$

A transform-limited pulse also holds the maximum possible peak power, due to the minimum duration. The minimum duration-bandwidth product is different for different pulse shapes. For example, gaussian pulses have a minimum duration-bandwidth product of 0.441 [31].

One of the primary advantages of using mode-locked ultrafast laser pulses for CARS thermometry is the temporal coherence exhibited by the pulses. The femtosecond laser pulses are generated by actively mode-locking an oscillator with a broad bandwidth such that all frequencies oscillate in phase. This induces the initial coherence when the pulses are temporally overlapped and all frequencies are in-phase, and their duration is very short due to quick dephasing, caused by their broadband nature.

Every signal has a time dependence and a spectrum that are related by the Fourier transform. Because of the mathematical properties of this transform, the time-bandwidth product (defined as above) is lower bounded. This property is called the Fourier uncertainty principle (which is also the mathematical explanation of Heisenberg's uncertainty principle in quantum mechanics). A Fourier-transform-limited pulse saturates the inequality and the equality holds. An optical pulse is said to be chirped when its instantaneous frequency (temporal rate of the instantaneous phase) has a dependence on time. This results in a spread of the localized constructive interference that makes the pulse. Specifically, an up-chirp (or positive chirp) means that the instantaneous frequency rises with time, and a down-chirp (or negative chirp) means that the instantaneous frequency falls with time (see figure 14). The magnitude of a chirp can be the rate of change in the instantaneous frequency, in units of hertz per second. The chirp of a pulse can also be non-linear (and contain higher-order chirp terms) where the rate of change of the instantaneous frequency is not constant over the pulse. [32].

When a laser pulse contains a finite bandwidth, different wavelengths are affected differently by the optical elements and media that the laser pulse passes through. In optics, dispersion is the phenomenon that results in the phase velocity (this is the velocity at which the phase of any one frequency component of the wave travels) of a wave being dependent on its wavelengths. Media having this common property are termed dispersive media. Generally, longer wavelength components travel faster than the shorter wavelengths, resulting in pulse broadening and a chirped pulse with different wavelengths of light at different durations of the probe. Hence, a pulse can be chirped using thick dispersive media, such as a glass rod. A 30cm glass rod was used to deliver a chirped probe pulse to generate a CPP CARS signal (discussed later) in [33] and in [29] as shown below in figure 15.

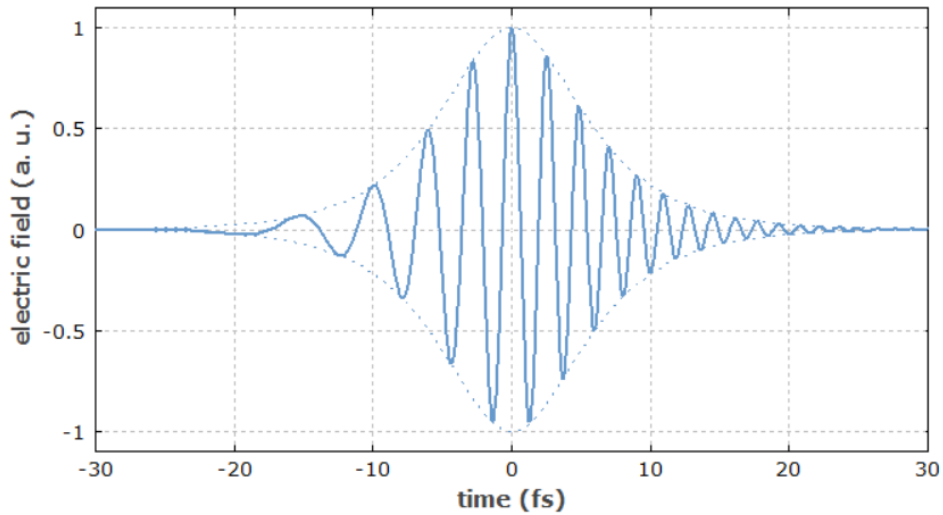


Figure 14: A positively chirped pulse in the time domain, with increasing frequency over time [32]. This leads to a spread of the localized constructive interference between the frequencies that make the pulse, resulting in a longer pulse (than T.L.).

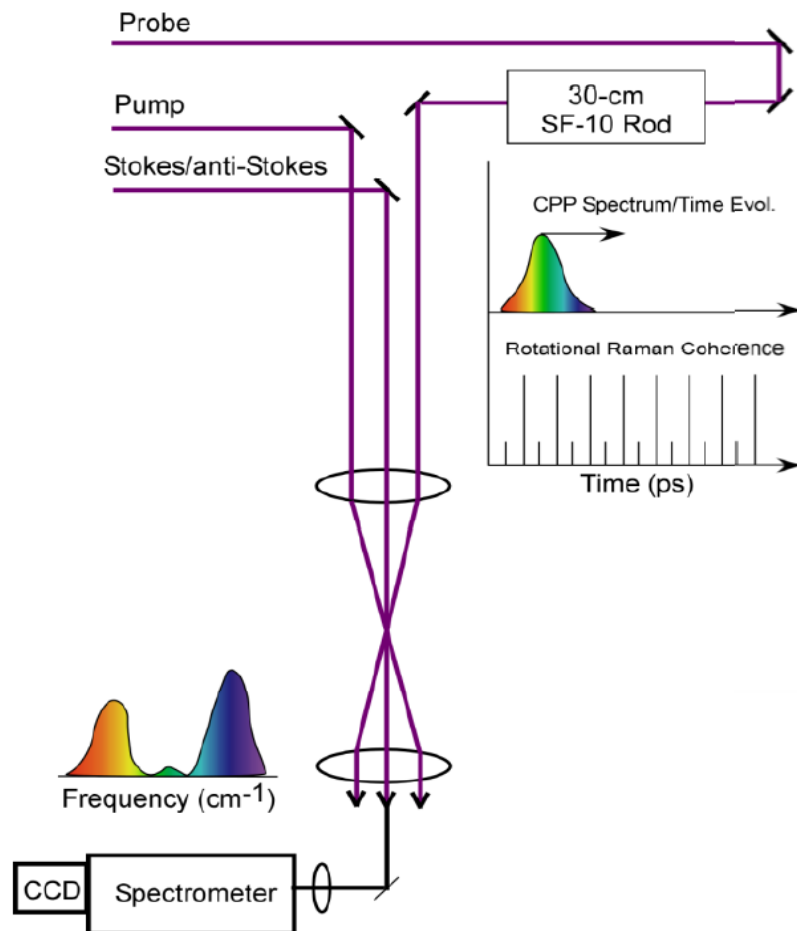


Figure 15: Producing chirp using dispersive material (Glass) and chirped probe pulse delivery for CPP CARS. The probe frequency-domain representation and molecular response of the medium are presented on the top right. The final CPP CARS spectrum, on the bottom left [29].

Gratings use diffraction to induce dispersion based on frequency in the laser pulse. Light impinging on a diffraction grating is either reflected or transmitted (depending on the type of grating) away from the grating surface toward a point in space that is reliant on its frequency,

and thus the individual frequencies can be dispersed. Sets of two diffraction gratings can be utilized to compress or stretch a laser pulse in time. To stretch a transform-limited laser pulse: When a broadband laser pulse is incident on a diffraction grating, the different frequencies that make up the pulse will diffract from the grating at points dictated by those frequencies. If a second grating is positioned such that it is not parallel to the first grating, then each frequency arrives at a different time, dictated by the difference in path length (due to the different dispersion angles). Once the light diffracts from the subsequent grating, the various individual frequencies of the pulse are recombined. This yields a spatially coherent pulse that contains frequencies delayed with respect to each other (chirp). When a chirped pulse is compressed (through a similar setup), a pulse with higher peak power is built, depending on the extent of compression. Pulse compression or stretching generally utilizes two gratings with the same groove frequency and efficiencies peaked for the polarization and carrier frequency of the laser, or a single grating can be traversed twice by each laser pulse [34].

## 2.9 Hybrid fs/ps CARS

A femtosecond (fs) is a unit of time equal to  $10^{-15}$  seconds, and a picosecond (ps) equals  $10^{-12}$  seconds. Hybrid Fs/Ps CARS (Hybrid femtosecond/picosecond coherent anti-Stokes Raman spectroscopy) has taken CARS to the next level and has become a gold standard for thermometry in flames. In this scheme, the broadband femtosecond pump and Stokes laser pulses form numerous photon pairs, allowing the coupling of every Raman transition and creating a strong Raman coherence in the molecular response [35]. This implies that the excitation bandwidth is sufficient to simultaneously excite the entire manifold of rotational states (also impulsively for pulse durations  $< \sim 50$  fs for  $N_2$ ). The duration of pump/Stokes pulses varies in between 30-100 fs and the narrowband probe in the order of a few ps. This also results in the frequency domain linewidth of the probe being small compared to the broadband pump and Stokes pulses, arising from the transform limit theorem. With sufficiently short fs pulses, a single degenerate pulse can be used to excite the pure-rotational coherence of most molecules of interest (i.e. two-beam CARS).

The usage of lasers as coherent light sources also allows the focusing of this beam to a very small area. The further crossing of laser beams that produce the CARS signal results in a very small area, with a diameter of  $\sim 50$  microns [36], and hence a very high spatial resolution. The emergence of femtosecond ultrafast laser systems delivering high peak pulse powers at high repetition rates also enables the acquisition of temperature and species through single-shot CARS measurements at Kilohertz rates in turbulent flames [28]. This follows from the extremely high peak powers that they can provide ( $\sim 7$  mJ per  $\sim 35$  fs pulse, direct from the laser) to be able to produce sufficient CARS signal intensity per pulse to acquire spectra from a single pulse, with sufficient signal-to-noise intensity. The resulting repetition rates (1 kHz) are capable of resolving almost all scales of turbulence in flames, where the number of molecules involved in the CARS process is low (from the CARS intensity, equation 8).

With this technique, it has also become possible to probe the molecular response and its decay by recording CARS signals at different time delays relative to the pump/Stokes excitation. With a revival peak occurring every  $\sim 8.4$  ps (in the case of pure nitrogen at room temperature), and the probe duration greater than this value (around  $\sim 9$  ps), temperature information from the decay of the coherence in the molecular response can be probed in a time-resolved manner (see figure 16). This is due to the relative intensity of Raman lines within spectra recorded at different probe delays being invariant, and hence models to resolve changes in spectra across delays are not important. Hence, the decay of the molecular coherence (which depends on temperature directly) can be probed and fit with models of the same to obtain temperature information. Simultaneously, the effects of any collision-related decay are avoided by probing only within the first  $\sim 100$  ps. The initial decay rate of the coherence is very sensitive to temperature and is not affected by collision rates or Stark shifts

(which pertain to the shifting and splitting of spectral lines of atoms and molecules due to the presence of an external electric field). These two factors have significantly complicated frequency-domain nanosecond CARS measurements, for example [37]. A time-domain model for the methane vibrational Q-branch transition was developed and validated using delay scans across various pressures and temperatures [38]. Here, the recorded CARS signal was compared to a synthetic CARS signal in which spectral line positions, line widths, and pulse shapes map the population distribution in the discrete energy levels of the probed species.

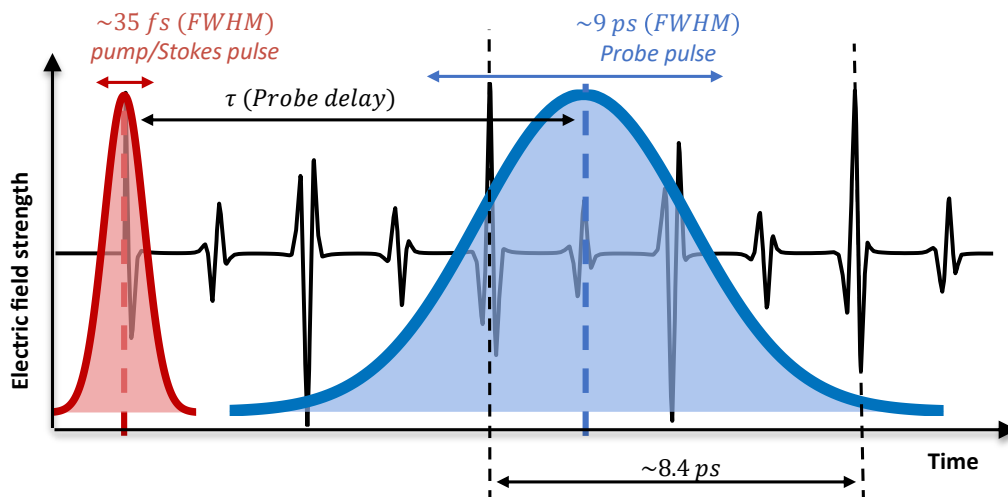


Figure 16: Femtosecond pump/Stokes pulses (only one is shown here) excite the pure-rotational coherence of Raman-active molecules. Picosecond probe pulse is coherently scattered from the molecules on a ps time-scale (collisionally independent signal). This ps pulse (~ 9 ps) is longer than one period of the nitrogen molecular response (8.4 ps).

## 2.10 CPP CARS

CARS measurements with ultrafast lasers can be performed using broadly two different methods. The hybrid fs/ps CARS, which was the subject of discussion in the previous section, and the chirped probe pulse CARS (CPP CARS). They both share the common pump/Stokes excitation of the Raman rotational transitions which also establishes the coherence. They differ in the way that this coherence is probed. A spectrally narrow picosecond laser pulse probes the coherence created into the medium in the case of hybrid fs/ps CARS. The laser pulses produced by the hybrid approach are in the order of picoseconds and their spectral shapes can be narrow enough to scatter off the different resonant rotational or vibrational frequencies of the probe species [39].

In the CPP fs CARS method, the probe beam used contains chirp. This means that the pulse (now less than a picosecond in duration) contains a broadband spectral linewidth, spread over time. In this new scheme, the Raman coherence is still created with the fs pump/Stokes interaction, but its advantage is to map the temporal decay of the Raman coherence onto the frequency domain of the measured CARS spectrum [33]. The signal will hence depend on both the CPP and the molecular response. By analyzing only rotational transitions, the technique can attain the name “pure rotational CPP CARS”. Theoretically, the CARS signal is produced from the convolution of both the electric field of the CPP and, the polarization of the molecular response. Here, each pulse can be described as a time-dependent electric field such as:

$$E_i(\vec{r}, t) = E_i(t) \exp[ik\vec{r} - i\omega t] \quad \text{Eq. 10}$$

The convolved product is then best described by the following equation from [14].

$$P^{(3)}(t, \tau_{23}) = \left(\frac{i}{\hbar}\right)^3 \int_0^\infty dt_3 \int_0^\infty dt_2 \int_0^\infty dt_1 \left[ R(t_3, t_2, t_1) E_3(t - t_3) e^{i(\omega_1 - \omega_2 + \omega_3)t_3} \times \right. \\ \left. E_2^*(t + \tau_{23} - t_3 - t_2) e^{i(\omega_1 - \omega_2)t_2} E_1(t + \tau_{23} - t_3 - t_2 - t_1) e^{i\omega_1 t_1} \right] \quad \text{Eq. 11}$$

Where  $\tau_{23}$  is the corresponding element in the third-order susceptibility matrix leading to third-order polarizability,  $P^{(3)}(t)$ . Here,  $t_1$ ,  $t_2$ , and  $t_3$  are the coherence time scales during the pump–Stokes, Stokes–probe, and probe–CARS interactions respectively,  $R$  is the molecular response function,  $E_1$ ,  $E_2$ , and  $E_3$  are the electric field envelopes, and  $\omega_1$ ,  $\omega_2$ , and  $\omega_3$  are the frequencies of the pump, Stokes, and probe electric fields. This temporarily ignores the spatial component of the electric field.

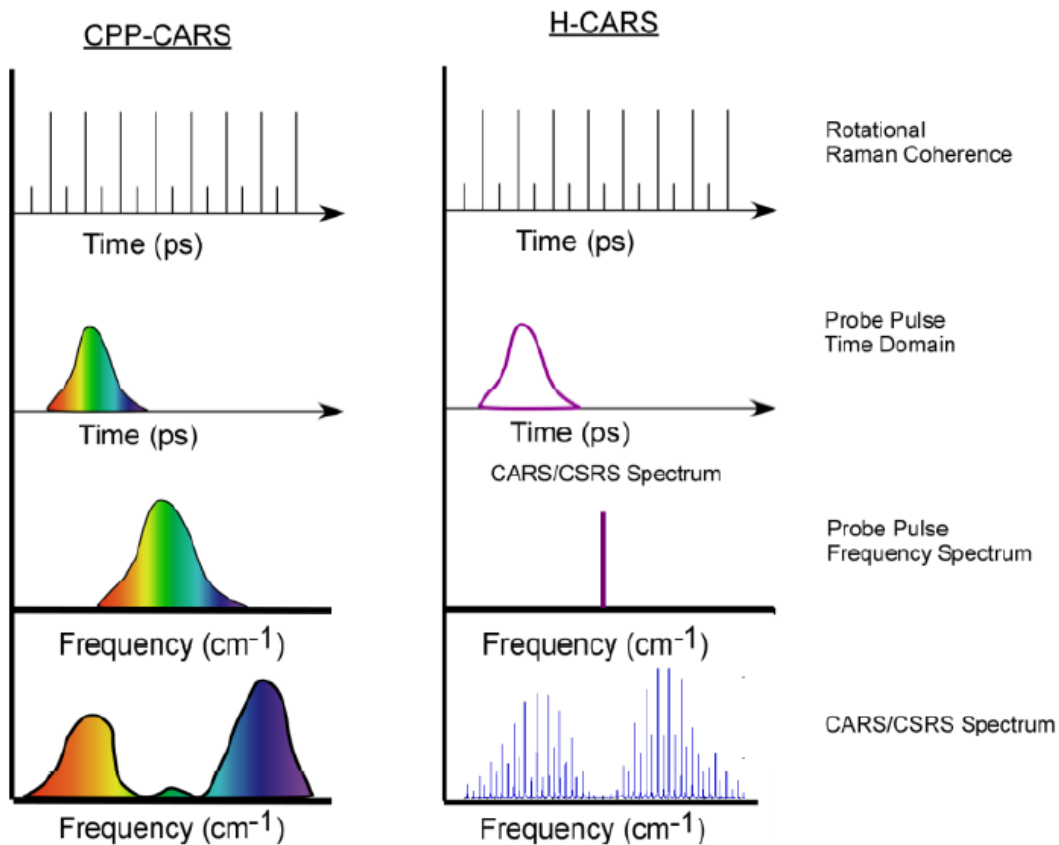


Figure 17: Comparison of rotational Hybrid and CPP CARS approaches, and the probe pulses involved [29]

The experimental simulation of such an interaction (Figure 18) was performed by [40], although they aimed to study the laser-induced alignment of molecules. From this figure, it can be seen how the CPP scatters from each of the revival peaks. If the chirp of the probe pulse is sufficiently large compared to the revival period (Example: For  $N_2$ ,  $\sim 8.4$  ps), the probe pulse temporally overlaps the complete revival structure (for pure rotational transitions). Each spectral component of the probe then samples the molecular response at a specific delay and experiences Raman shifts accordingly. Therefore, recording the spectrum at a given fixed

pump-probe delay maps the dependence on time of the polarization of the molecules in the sample onto the frequency domain. Full information on the revival structures was obtained on a single-shot basis by [40].

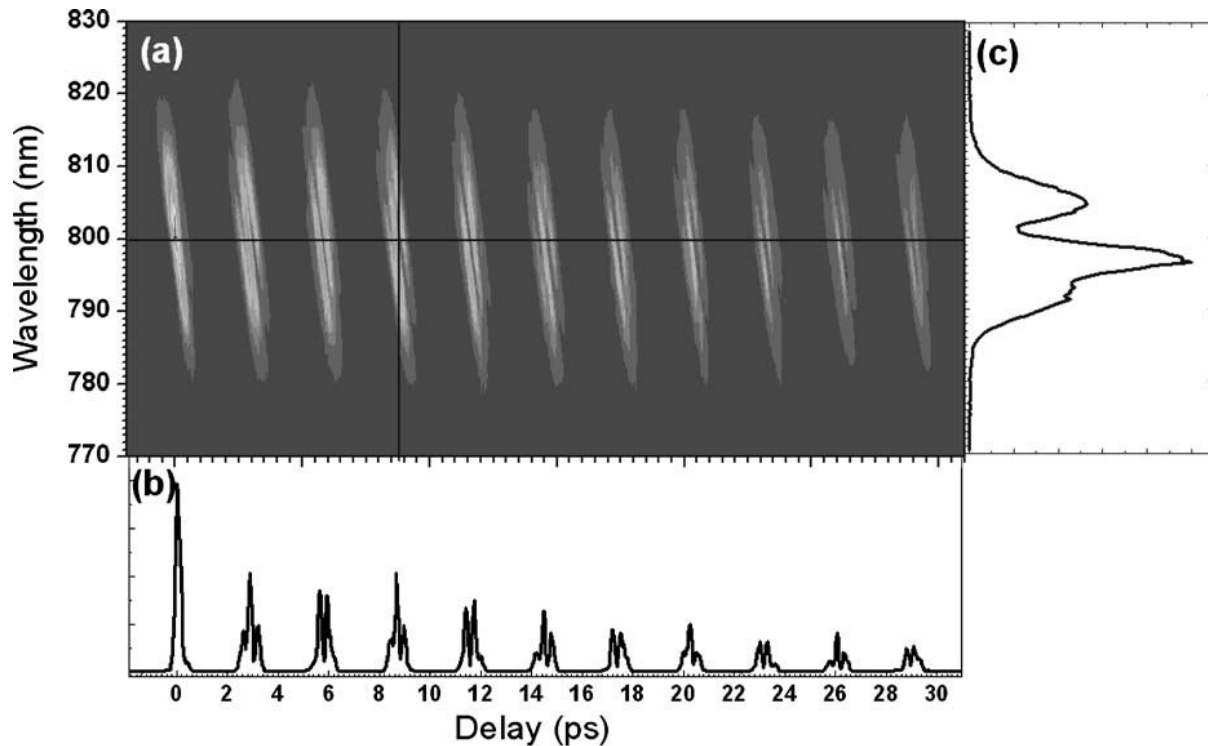


Figure 18: Interaction of the CPP with the molecular response at different time delays (on the x-axis). (a) Time-wavelength contour plot showing the spectrum of the probe beam that is transmitted through because of the birefringence of the molecular sample, as a function of the delay between the pump/Stokes excitation and the chirped probe pulse. (b) The signal transmitted at 800 nm as a function of the pump-probe delay. (c) The spectrum of the probe beam at a pump-probe delay of 8.8 ps [40].

The time-wavelength contour plot in Figure 18 illustrates the signal evolution as a function of the delay in time between the pump/Stokes and probe pulses. Both the initial transient alignment (due to incident laser pulses, the first slanted ellipse is at  $t=0$ ) at zero pump/Stokes – probe time delay and the revival structures that occur repeatedly at intervals of 2.89 ps can be seen. The revival structures appear as slanted ellipses [40]. The slope is related to the (linear) chirp of the probe pulse, due to the frequencies arriving at linearly segmented times. The ellipse shape can be attributed to the short duration of one revival structure (causing elongation in the x-axis), along with the bandwidth contained in the structure (causing a long ellipse stretched in the y-axis). It can especially be seen from Figure 18 (c), how using a chirped probe pulse can destroy the spectral resolution of different Raman lines, albeit without losing any spectral information.

# 3

## Experimental setup: two-beam hybrid fs/ps CARS

It has already been discussed, how the CARS technique can perform non-intrusive measurements in-situ and provide scalar information with excellent spatial and temporal resolution. The experimental setup used for this thesis is located at the Advanced Laser Diagnostics and Flame Laboratory at the Faculty of Aerospace engineering at the TU Delft. The lab is used for thermometry in flames and performing experiments for various projects. The CARS setup in the lab is shown in figure 19 and employs hybrid fs/ps CARS. This existing CARS setup is capable of measuring temperature with precision  $< 1\%$  and accuracy  $< 3\%$ . The spectral resolution of this technique is mainly limited by the linewidth of the probe pulse. Considering the energy separation of the pure-rotational nitrogen CARS spectral lines ( $\sim 8 \text{ cm}^{-1}$ ), a  $\sim 10 \text{ ps}$  duration *transform-limited* probe pulse would result in isolated spectral lines, dispersed at the detector [36]. The probe in this setup is produced from a second harmonic bandwidth compressor, pumped by a broadband pulse from the only laser source. The SHBC delivers picosecond transform-limited pulses from the incoming femtosecond transform-limited laser pulse. The short duration of the pump/Stokes pulse (when optimized,  $\sim 35 \text{ fs}$ ) also ensures impulsive excitation of the Raman transitions. The excitation can be considered impulsive if the durations of the fs laser pulses are less than one-tenth of the molecular rotational period [41]. For example, a  $\sim 50 \text{ fs}$  laser pulse is required to impulsively excite  $N_2$  with a  $\sim 500 \text{ fs}$  rotational period [36].

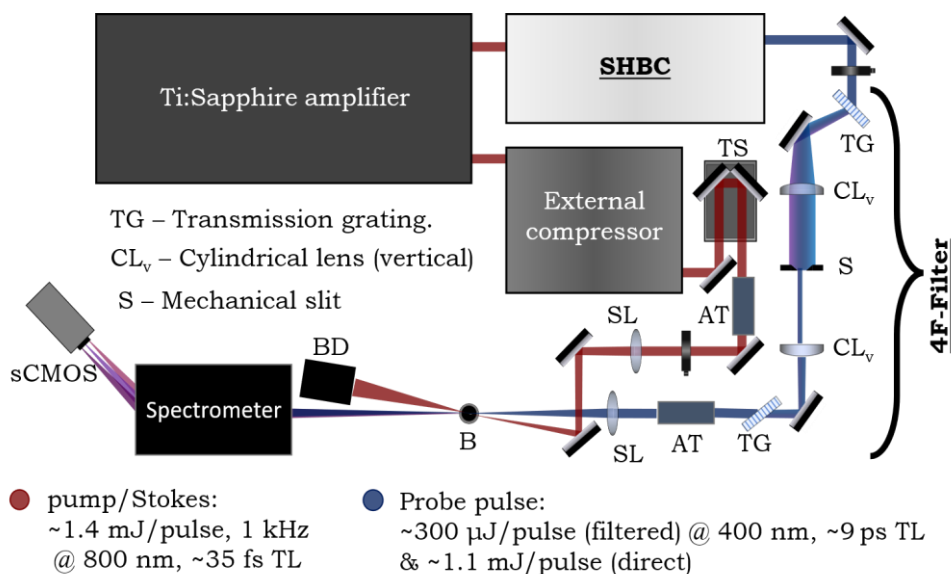


Figure 19: Current hybrid fs/ps CARS setup. Nomenclature: TG, transmission grating; S, slit; TS, translation stage; CL, cylindrical lens with horizontal (h) and vertical (v) alignment symmetry axes; AT, attenuator (half-wave plate + polarizer); B, burner; SL, spherical lens; sCMOS, camera.

### 3.1 Laser system

In figure 19, the paths of the pump/Stokes, probe, and CARS beams can be seen. The Single regenerative laser amplifier system produces transform-limited laser pulses at a 1kHz repetition rate, with ~7mJ per pulse at ~800 nm and ~35 fs. Before the amplification, ~20 fs transform-limited pulses, 80MHz repetition rate, with pulse energies in the orders of nJ are present. The pulse is stretched inside the laser before amplification for the chirped pulse amplification technique. A chirped pulse can be amplified more due to its energy being spread in time. This is because amplifying a transform-limited fs pulse to high peak energies is limited by the laser-damage threshold of the gain medium in the amplifier (due to the high peak power of transform-limited fs pulses). Chirped pulse amplification (CPA) has revolutionized laser technology, elevating the output powers to the petawatt regime in the past thirty years or so and possibly beyond that soon [42].

### 3.2 Degenerate pump/Stokes pulse

After the amplification process, the pulse is split out of the laser amplifier before compressing it. This output pulse from the laser is split 65% (for the probe) and 35% (for the pump/Stokes). The degenerate pump/Stokes pulse exits the system uncompressed in time, and an external compressor is used to control its compression. The probe pulse is compressed back to a transform-limited fs pulse using the compressor part of the CPA system, and it is possible to control the extent of compression, to chirp/pre-chirp the pulse. This usage of the degenerate pump/Stokes pulse is only possible due to its broadband nature, short duration, and high peak power, allowing the excitation of the entire rotational manifold using different difference frequencies present within this pulse. Hence, a two-beam fs/ps configuration is employed. The two-beam configuration significantly reduces the number of degrees of freedom in the setup and improved signal levels can be achieved because of both the ease of alignment and the higher pulse energy available to the pump and Stokes fields. Phase matching conditions when satisfied, result in the probe beam and the generated rotational CARS signal propagating in the same direction [13]. From Equation 8, it can also be seen that  $I_{CARS} \propto I_{pump/Stokes}^2 \cdot I_{probe}$ . This is because the pump/Stokes beam is degenerate in the current setup and hence the CARS signal intensity scales quadratically with the intensity of the beam. An optical delay line is then used to tune the difference in path length between the pump/Stokes beam and the probe beam, and hence their relative arrival time at the probe volume. The translation stage is fully automated, and the desired time delay can be easily set between the pump/Stokes and probe pulses.

#### 3.2.1 Two-beam phase-matching

Many phase-matching schemes are not feasible with the current two-beam setup. CARS using only two laser beams does not utilize the full flexibility of four-wave mixing. The advantages of using three laser beams for CARS compared to two beam CARS are better spatial and spectral discrimination of the signal from noise (due to the ability to ensure phase-matching) and the possibility of point probing in gases. However, the need to overlap three (tightly focused) beams is a significant experimental inconvenience. Generally, both three-beam CARS, and in two-beam CARS, the phase-matching angles depend on the medium dispersion and the magnitude of the Raman shift,  $(\omega_1 - \omega_2)$  [43]. In this setup, the two beams are crossed at a shallow angle (collinear phase-matching) which creates the coherence in a spatially well-resolved manner (~45 microns diameter) at the “probe volume”, which is the volume of the interaction of the laser pulses and where the CARS signal is generated from.

### 3.3 SHBC and the probe pulse

The 65% probe is then passed to the SHBC where the fs pulse is converted to a narrowband ps pulse. This conversion efficiency is around ~30% and the probe beam contains ~1mJ per pulse at the output of the SHBC. This is now a narrowband pulse of duration ~4ps (FWHM) [36], centered at ~402 nm, and is both repetition-wise synchronized with the fs pump/Stokes pulse and automatically phase-locked at the CARS measurement, with an arbitrary arrival time [43]. This automatic temporal lock of the two pulses has a large positive impact on the precision of the technique.

The SHBC essentially carries out sum-frequency generation from two fs pulses with conjugate chirps and provides picosecond probe pulses with energies over 1 mJ per pulse (in this setup) that are temporally locked to the femtosecond pump/Stokes preparation. This method overcomes previous limitations on hybrid femtosecond/picosecond rotational CARS techniques, which have relied upon less efficient bandwidth-reduction processes that have generally resulted in prohibitively low probe energy for flame measurements [44], [45]. The input fs broadband transform-limited pulse is split in two (via a beam splitter) and chirped conjugately (as symmetric chirp ramps, figure 20a) using the frequency-dependent dispersion of gratings. Using a lens, the different frequency content that was dispersed from the grating can be focused and reflected to arrive at different spatial coordinates on the same grating, which gathers back the frequencies and imparts a temporal chirp dependent on the distance between frequencies incident on the grating. By positioning the focus of the lens behind the grating, a negative chirp is induced and with the focus in front, a positive chirp can be induced. By producing the same magnitude of chirp, positively in one branch and negatively in another, exact phase conjugate chirped beams are achieved in the SHBC. These conjugate “arms” are then coincident temporally and spatially at a BBO crystal, where they undergo sum-frequency generation. This conjugate chirping is necessary because pairs of frequencies need to be carefully chosen, that only yield to the same wavelength (half of the fs carrier wavelength, 400nm, and twice the frequency). This is shown in figure 20b.

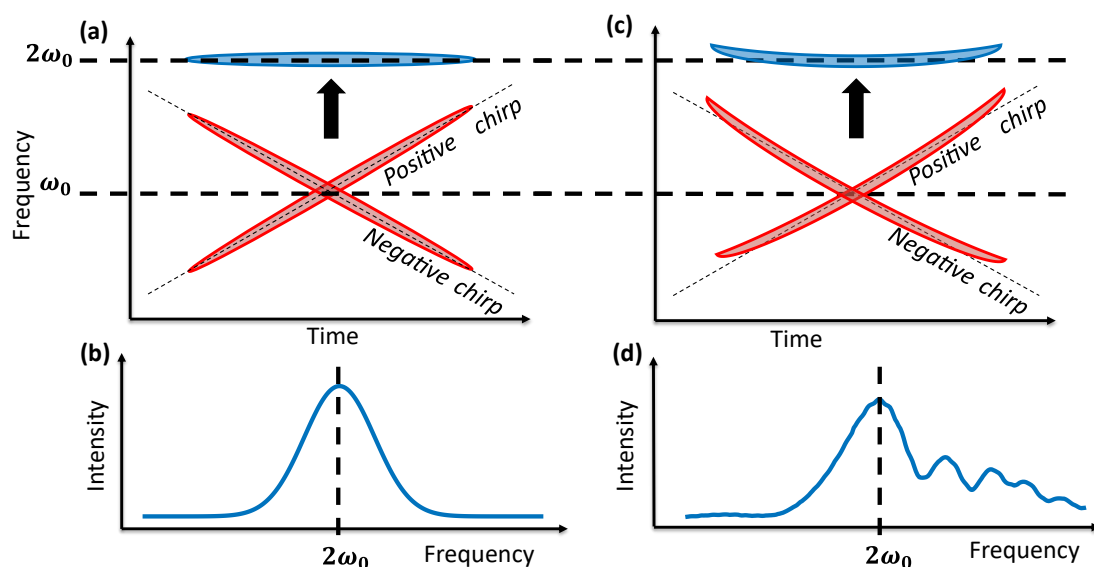


Figure 20: Working of the SHBC.  $\omega_0$  is the center frequency of the input pulses, which gets summed conjugately to  $2\omega_0$ . (Top) The conjugation from broadband pumps, leading to an SFG output in (a) perfect conjugation and (b) imperfect conjugation due to higher-order chirp terms imparted to the arms (broadband chirped pulses). (bottom) Spectra of the output of the conjugation (b) Gaussian shape from the case of perfect conjugation and (d) Higher frequency terms or “sidebands” being generated through imperfect conjugation.

At the output of the crystal, alongside the SFG signal, other signals such as the second harmonic generation and the individual broadband beams are also present at differing angles depending on their respective phase-matching conditions. The treatment of these signals, however, goes beyond the scope of this report.

The conjugate nature of the two arms in the SHBC can be disturbed by any additional chirp imparted to the pumps and this would give rise to a chirped pulse at the output of the SHBC, due to the sum frequency generation occurring between asymmetric components of frequencies in each contributing arm (figure 20c). The probe beam pulses that are compressed in the SHBC might be chirped due to imperfections in the gratings of the second harmonic bandwidth compression process. Many researchers use the SHBC to compress the probe pulse and are faced with the above-mentioned problem due to higher-order non-linear chirp generation from the gratings of the SHBC [44], [45], [47]. The output is no more a perfect transform-limited pulse but contains “sidebands” in the frequency domain separate from the “main lobe” centered at 402nm (figure 20d). This probe beam pulse may also be chirped at the output of the SHBC. This pulse is treated by removing certain frequencies from it through a 4F filter (see next section). These unwanted frequencies, if not removed, will scatter from the molecular response, leading to multiple carrier frequencies in the CARS signal with close center wavelengths [47]. A more efficient generation of a narrowband pulse by chirped pulse mixing is explained in the paper [45], although a fraction of photons is still lost in this process.

### 3.4 4F filter

In the setup, these sidebands are removed via 4F filtering, which is shown in Figure 21. The common 4F system contains two lenses L1 and L2, both with focal length  $F$ . The frequencies are separated before entering this system. Separated frequency components are then collimated by the lens and are incident on the Fourier plane, which exists at the center of the 4F optical system. Each point in the Fourier plane corresponds to a single spatial frequency and the image at the Fourier plane is exactly the spatial Fourier transform of the input beam. Using a slit (which is an optical device consisting of two blades that can move relative to each other in the parallel direction), the unwanted frequencies can be removed. The second lens reconstructs the image for a second grating, after which, the pulse is reconstructed spatially with the preserved frequencies [48].

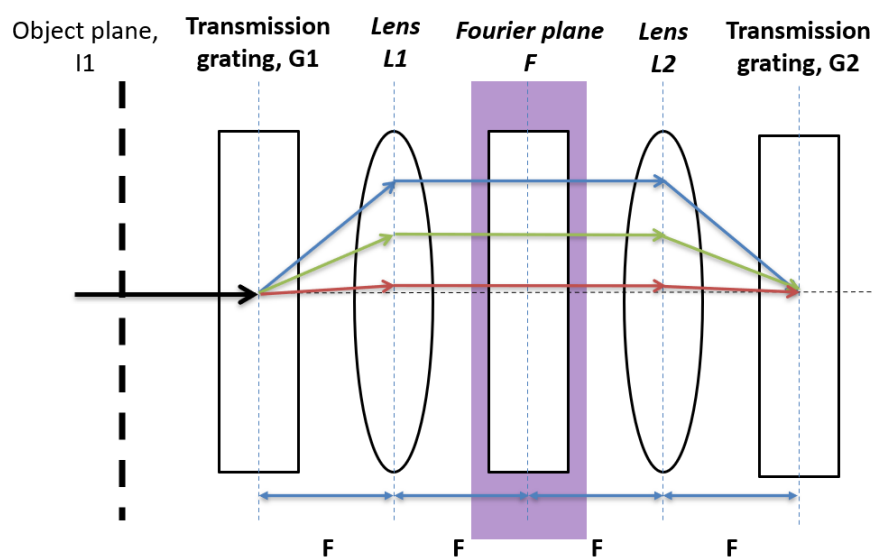


Figure 21: 4F filter design. G1 and G2 – transmission gratings; L1 and L2 – lenses;  $I_1$  – object plane; F – Fourier plane (and focal length when denoting distance).

The 4F filter dumps “unwanted” frequencies from the probe pulse. This effectively dumps probe photons that could contribute to the intensity of the resulting CARS signal, resulting in a loss in intensity of ~70% in the cleaned probe pulse. Half-wave plates (provided by Eksma Optics in this setup) change the relative polarizations of input beams and are the main cause of such high losses in the 4F-filter [36]. In this setup, they are needed to:

- 1) Control the relative polarizations of the pump/Stokes beam and the probe beam (this also adds a layer of control on the attenuation of the output CARS signal),
- 2) Maximize the grating efficiency by turning the probe beam polarization to the transmission axis of the grating (>90% diffraction efficiency at 400 nm for s - polarization) in the optical line for the 4F-filter (discussed later), and
- 3) Turn the polarization of the output CARS beam to satisfy the transmission axis of the grating at the spectrometer.

### 3.5 Camera and spectrometer

The sCMOS (scientific Complementary metal-oxide-semiconductor) is the camera in the setup and records the optimized CARS signal at the end of the spectrometer. It has a varying quantum efficiency over its frequency range but in the pure-rotational region, the quantum efficiency is more or less constant. The sCMOS camera records at a repetition rate of 1kHz and has an exposure time that is orders of magnitude larger than the duration of the laser pulses. Hence, the CARS pulse at the output will be a sum-response from the scattering of the duration (in ps) of the probe with the molecular response, and the information on the Raman transitions is contained in this pulse. This CARS pulse is then dispersed into its constituent frequencies to gain Raman shift information from it. This is done using a relay telescope where a grating is used to disperse frequencies, along with a lens to focus them onto pixels on the camera [43]. And so, the CARS signal spectrum is achieved, which can be fitted with models to retrieve accurate temperature and species data.

# 4

## Research objective

In the CARS facility, laser pulses of high power  $\sim 1.1$  Watt (and pulse frequency  $\sim 1$  kHz) are commonly used. However, the Raman scattering is very weak. Even though the output pulses are made to be coherent by coherently preparing the molecules in the case of CARS spectroscopy, it is challenging to observe good quality signal (high signal to noise ratio) in flames due to the low number of molecules per volume (to scatter from) at higher temperatures. Hence, this project researches how the signal-to-noise ratio of hybrid fs/ps CARS spectra can be increased, especially when using a single laser source with unvarying power.

The use of SHBC is a clever scheme to efficiently produce a ps narrowband probe pulse from the fs laser source. However,  $\sim 70\%$  of the intensity in the probe pulse is lost when the signal is subsequently filtered through the 4F-pulse shaper, which could be useful to measure high temperature in flames or perform temperature imaging. The operation of the 4F-filter and a comparison of how the probe pulse looks in the frequency domain when filtered through the 4F filter (mechanical slit in the Fourier plane closed to 150 microns, termed either the filtered probe pulse or the probe pulse with the “slit closed” throughout this report) and without filtering (mechanical slit in the Fourier plane open to at least 1.3 mm, termed either the direct probe pulse or the probe pulse with the “slit open” throughout this report) is shown in figure 22. Additionally, the direct pulse from the SHBC might contain chirp due to the aforementioned imperfect generation through conjugation in the SHBC. A chirped probe can still gather valuable time-domain information on the molecular response by mapping it onto the frequency domain (regardless of the non-isolation of Raman lines), as shown by CPP CARS.

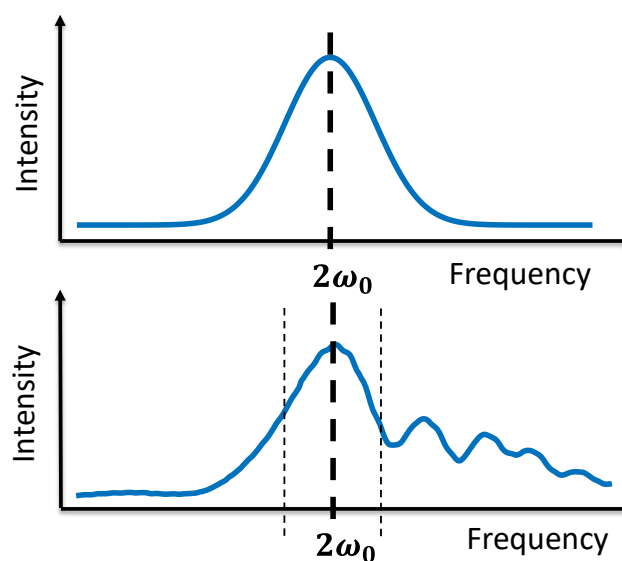


Figure 22: Comparison of the direct probe output of the SHBC (bottom) to an ideal Gaussian profile with similar FWHM (top). The operation of the 4F-filter (light dashed lines in the bottom figure), applying a top-hat filter in the frequency domain to the pulse profile.

Moreover, the current CARS models cannot predict temperature using the signal produced with the direct output of the SHBC. This is shown in figure 23 (with a pure rotational nitrogen CSRS spectrum at room temperature), and the differences in the spectra are due to the impact of the frequencies present in the direct output from the SHBC. The blue curve on the figure to the right shows the experimentally acquired spectra generated by the direct probe for one shot, which is significantly different from the same generated by the filtered probe (blue curve on the left). The attempt to fit such a spectrum retrieves a very inaccurate temperature value.

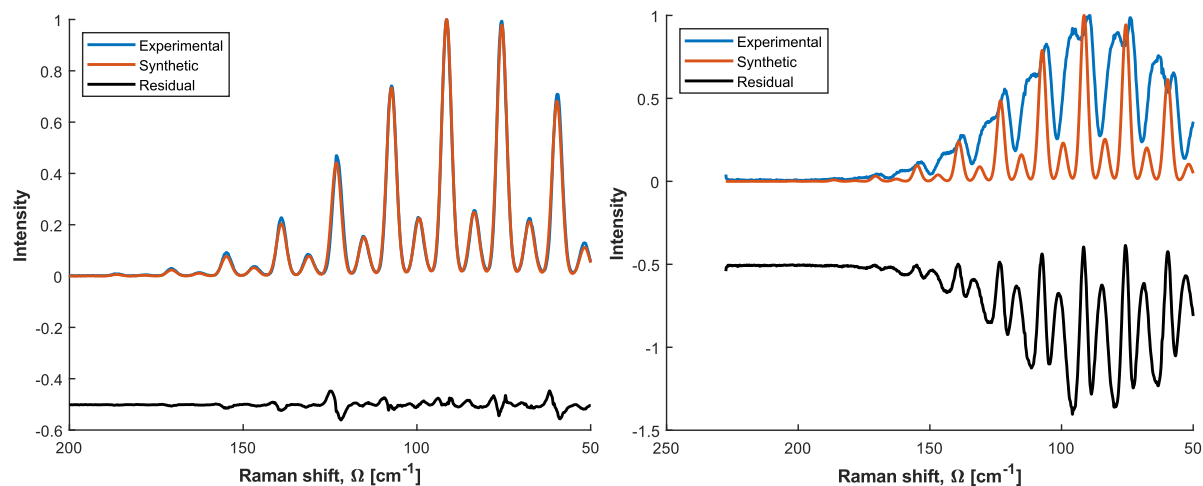


Figure 23: Best fit for nitrogen CSRS spectra at room temperature at a probe delay of  $\sim 43.53$  ps, performed for both the direct (right) and filtered (left) probes. Synthetic best fit using the same model for the filtered probe (orange curve), and experimentally acquired spectra (blue curve). The black curve computes a residual between the two. The fitted temperature for the filtered probe pulse (left) is  $\sim 290$  K, and for the direct probe pulse (right),  $\sim 400$  K.

This direct output pulse might also contain chirp, which may add a time variation to the spectra recorded using it. The only way to predict temperatures using this probe pulse shape is to fully understand it by characterizing it in the frequency and time domains to use it alongside models for molecular responses.

#### 4.1 Utilizing the direct probe pulse from the SHBC for hybrid fs/ps CARS

This section analyses the impact of the additional photons from the direct probe pulse and their involvement in the coherent scattering process. Firstly, as a result of the time-bandwidth product relation, the broader bandwidth in the direct probe pulse results in the shortening of the pulse in time. This can be seen from figure 24, where the pulse formed with the slit open has a shorter duration than the one formed when the slit is closed. These time-domain pulses were measured using a method of correlation that will be explained in the subsequent chapter (A delay scan using the non-resonant signal from Argon). The time-domain information suggests that not only has the pulse become shorter but it also has a much more unpredictable shape. This experimental data was also influenced by parameters that will be detailed later, making it unreliable to an extent. Nevertheless, this much-changed shape most definitely indicates the existence of a chirp within the pulse.

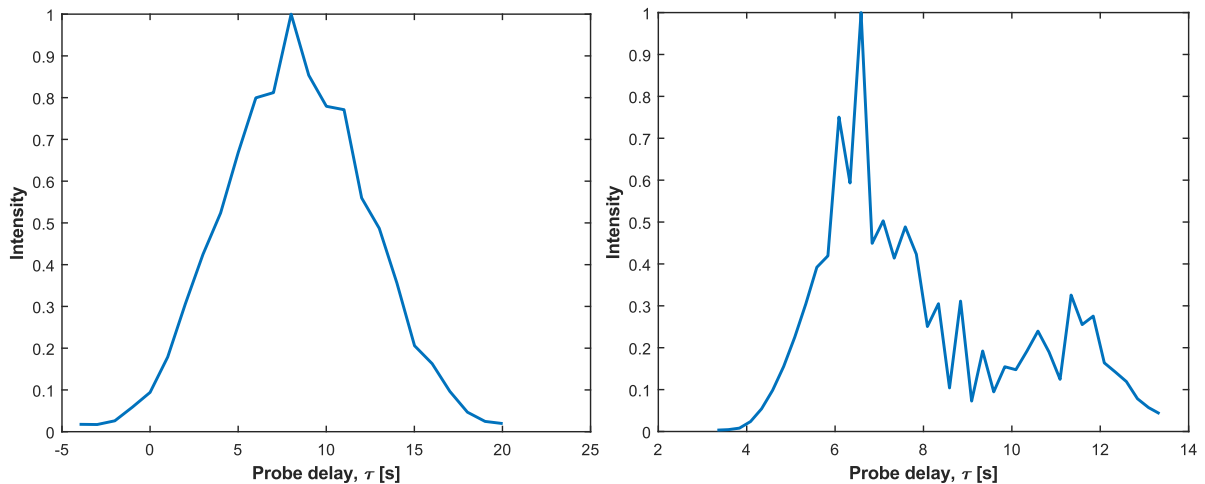


Figure 24: (Left) Time-domain probe pulse formed when the slit in the 4F plane is "closed". This data was recorded experimentally by performing a delay scan of the non-resonant signal across the probe. The FWHM of this pulse is  $\sim 10$  ps. (Right) Time-domain probe pulse formed when the slit in the 4F plane is "open". The duration of this pulse is shorter. These profiles were recorded experimentally by performing a delay scan of the non-resonant signal across the probe (for each probe).

All the experimental CARS data presented in this chapter are recorded by measuring spectra through 1000 frames with a repetition rate of 1 kHz (and an exposure time  $\sim 1$ ms), through different gasses provided by a 10 cm diameter Bunsen burner. The measurement of resonant spectra is repeated for a total of 81 probe delays ranging from  $\sim 33.65$  ps to  $\sim 53.25$  ps with a step size of 250 fs. Figure 25 shows the relative intensity of the first two resonant Raman lines of pure hydrogen at room temperature. This data was produced from the interaction of the pump/Stokes pulse with only hydrogen molecules in the probe volume, which then get prepared to a coherent state and produce a molecular response. The probe can then scatter off the response but at a controllable delay from the initial excitation of the coherence that can be controlled by the delay stage that adds a certain controllable path (probe delay) to the distance traveled by the (pump/Stokes) pulse.

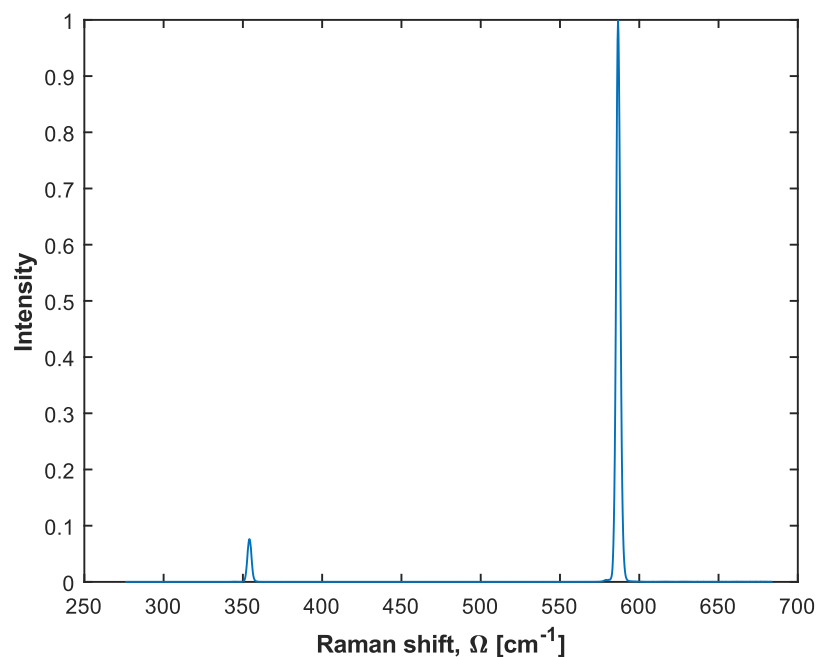


Figure 25: Experimental hydrogen CARS spectrum (first two lines) at room temperature recorded with the slit closed.

The frequencies of these two lines are very well separated (as compared to their linewidth). Due to this reason, their CARS signal is also not affected by the frequencies in the probe (see [appendix](#) for more information). Due to the frequent modulation in this response (as compared to the duration of the probe pulse,  $\sim 9$  ps), this CARS spectrum produced from scattering off of different delays is invariant. The synthetic molecular response of  $H_2$  is shown in figure 26. The invariance in spectra across delays can be captured by a spectrochronogram, which is formed by composing the recorded spectra at multiple delays into a contour plot as shown in figure 27. Here, each horizontal line is a spectrum recorded at a different delay.

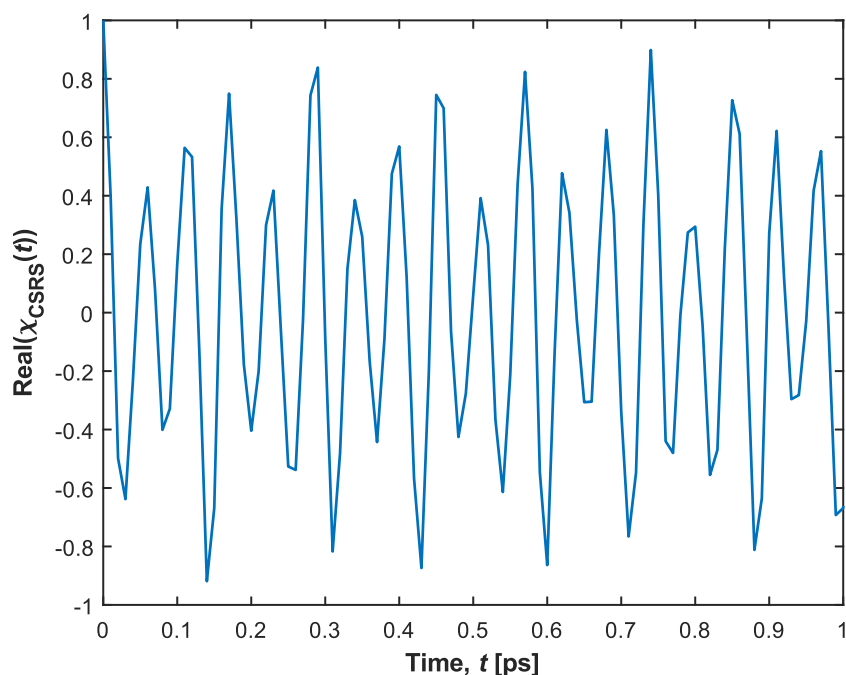


Figure 26: Synthetic molecular response of pure hydrogen at 300K, showing a full revival of the initial coherence at  $\sim 8.4$  ps and half revival at  $\sim 4.7$  ps.

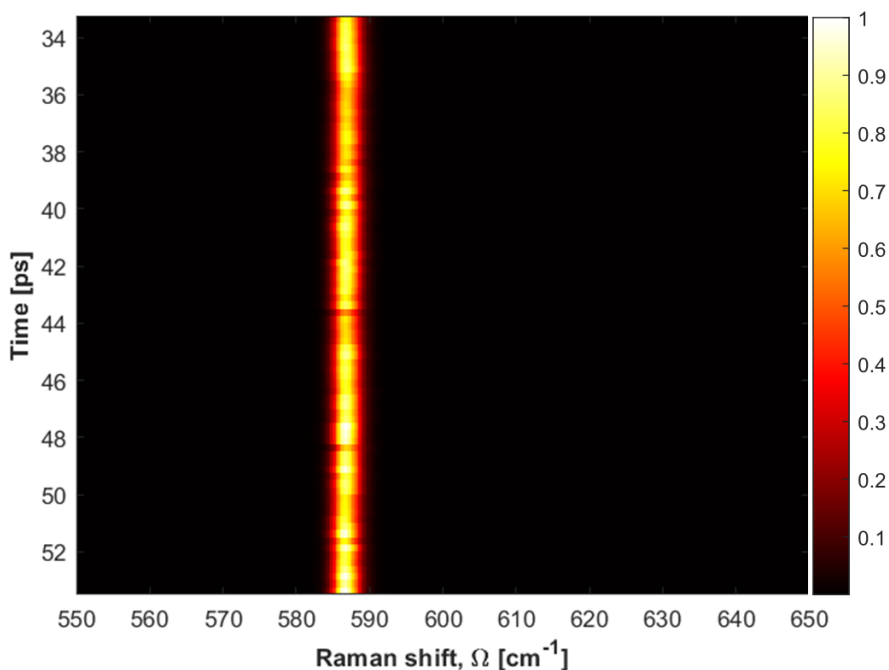


Figure 27: Experimental hydrogen CARS spectrochronogram at room temperature with the slit closed. Each horizontal line is a spectrum like that in figure 25. Here, only one line of  $H_2$  is shown to zoom in.

The same spectra can then be recorded with the slit open to make a comparison. The extra frequencies in the probe then interact (a direct convolution) with the hydrogen molecular response and are involved in the CARS process. The CARS spectra produced now see an “imprint” of the extra frequencies on each Raman line. This is shown in figure 28. Due to the frequent modulation in the molecular response, again, the spectrochronogram compiled (using spectra recorded with the direct probe) shows no variance in spectra, as can be seen in figure 29 and, the same imprint of the extra frequencies can be seen across delays. Any small variations are expected to be due to irregularities in the data acquired.

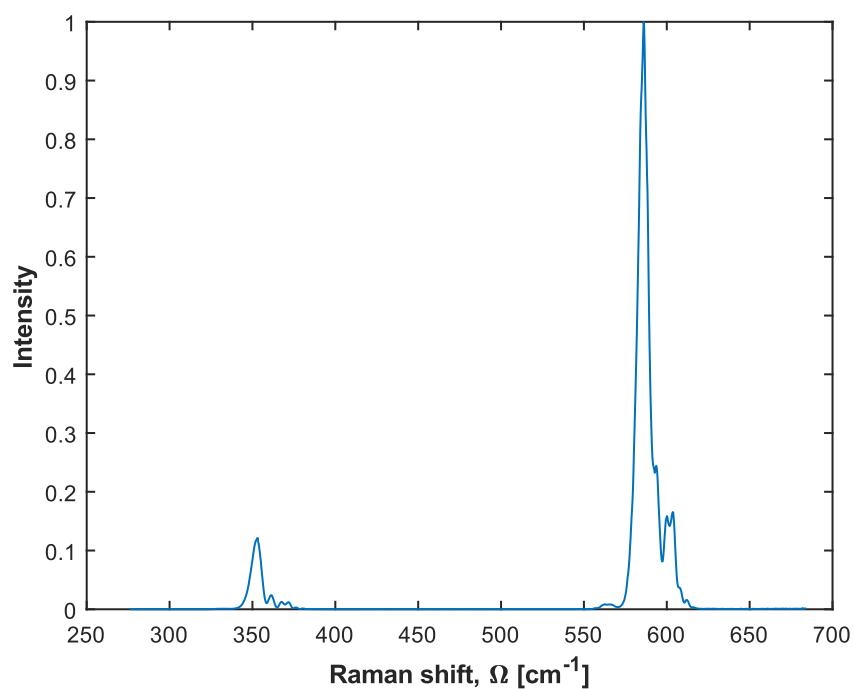


Figure 28: Experimental hydrogen CARS spectrum (first two lines) at room temperature recorded with the slit open.

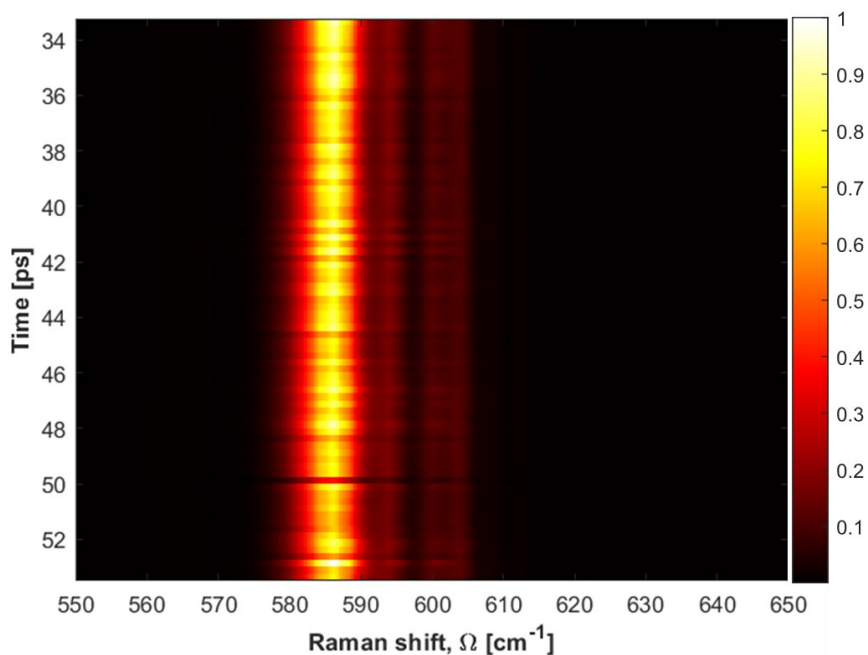


Figure 29: Experimental hydrogen CARS spectrochronogram at room temperature with the slit open. Each horizontal line is a spectrum like that in figure 28. Here, only one line of  $H_2$  is shown to zoom in.

Nitrogen is the most commonly used molecule for CARS thermometry (due to its abundance) and has resonant Raman lines much closer to each other (in frequency separation) than hydrogen. Figure 28 showed the imprint of the higher frequencies in the probe onto each Raman line of hydrogen. Additionally, there was no variance with probe delay. However, closer Raman lines imply the possibility of these lines to interact and convolve with each other when recorded using the direct probe, producing spectra that do not have separate lines, but a more continuous shape (as shown in figure 23). The rest of the spectra shown in this report are recorded on the CSRS side due to reasons mentioned in the [appendix](#). Figure 30 shows the CSRS spectrochronogram compiled from delaying the probe pulse through pure nitrogen at room temperature, recorded with the slit closed. Due to the probe pulse being longer than one half-revival period of nitrogen ( $\sim 4.7$  ps, figure 7), and its linewidth (in frequency, when the slit is closed) being low, this spectrochronogram also shows no variance across different probe delays.

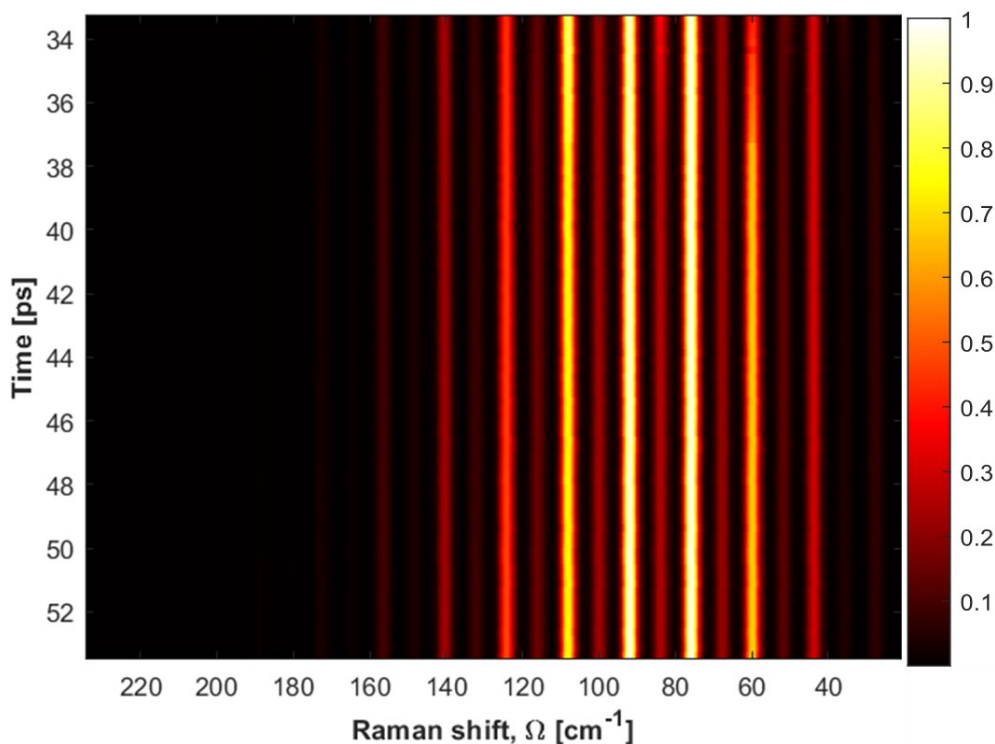


Figure 30: Experimental nitrogen CSRS spectrochronogram at room temperature with the slit closed. Each horizontal line is a spectrum like the blue curve on the left of figure 23.

However, when the same spectrochronogram is reconstructed using data recorded with the slit open, we see a change in spectra per probe delay. Figure 31 shows this significant variance across probe delays, which is hypothesized to be due to the varying time-arrival (chirp) of the different frequencies in the probe pulse, which influences the instantaneous carrier frequencies scattering off from different parts of the molecular response at different times.

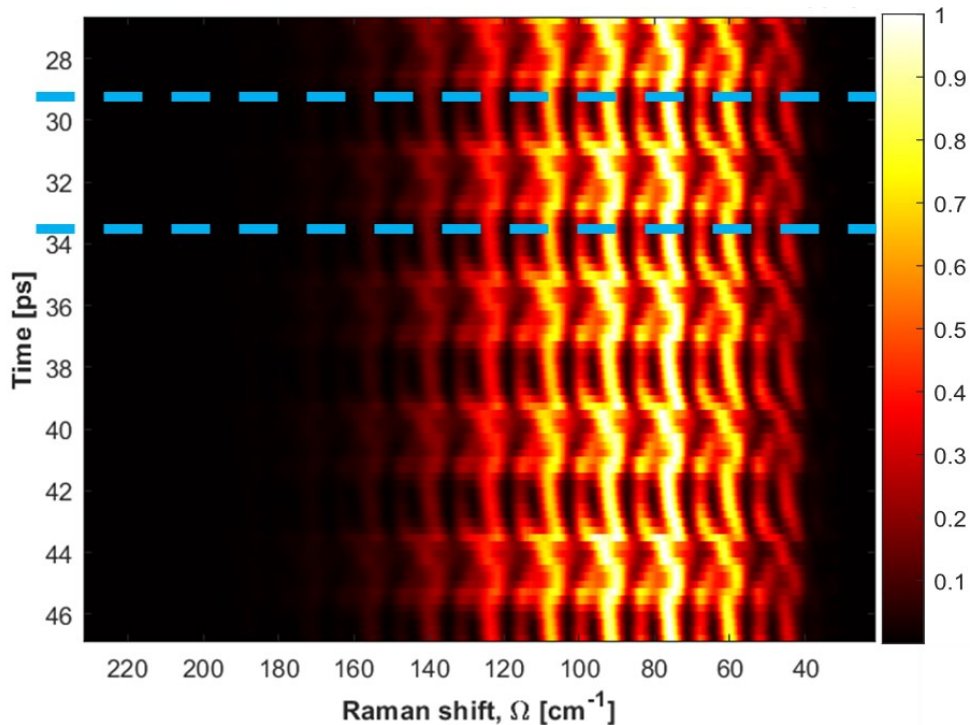


Figure 31: Experimental nitrogen CSRS spectrochronogram at room temperature with the slit open. Each horizontal line is a spectrum like the blue curve on the right of figure 23 (which is the spectra from the y-axis position: 43.53 ps). The horizontal blue dashed lines indicate a periodicity of  $\sim 4.2$  ps in this figure.

Some conclusions can be drawn from this figure (the results chapter explains them in detail):

1. Depending on the probe delay, subsequent even and odd lines get convolved and form a more continuous shape.
2. There is a distinct periodicity relating to the  $N_2$  rotational period ( $\sim 4.2$  ps).
3. This is mainly due to the chirp (phase information) contained in the probe pulse.

## 4.2 Impact of the extra photon content on signal-to-noise ratio and precision

It has been shown what the CARS/CSRS spectra look like when the slit in the 4F plane is opened, and the extra photons can participate in the CRS process. The differences are quite evident and differ depending on the molecule. However, this project aims at including them in the signal generation to increase the probe power in the probe volume. The CRS signal observed with the extra photons either contains a higher overall signal count (in the case for nitrogen) or falls on separate spectral positions (in the case for hydrogen). Both cases will be discussed subsequently: Figure 32 shows the spectral positions that each Raman line of hydrogen occupies. This is the region over which a useful signal can be seen when the slit is closed. Figure 33 shows the same signal when recorded using the direct probe pulse.

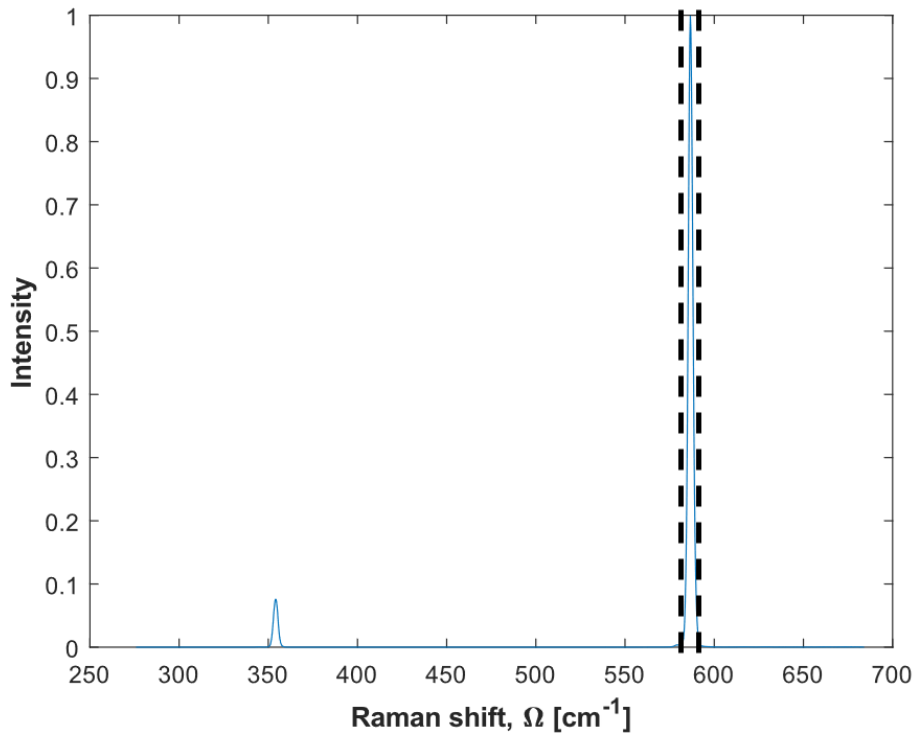


Figure 32: Pure  $H_2$  CARS at room temperature (experimental): Spectral region containing information on one  $H_2$  Raman line (slit closed)

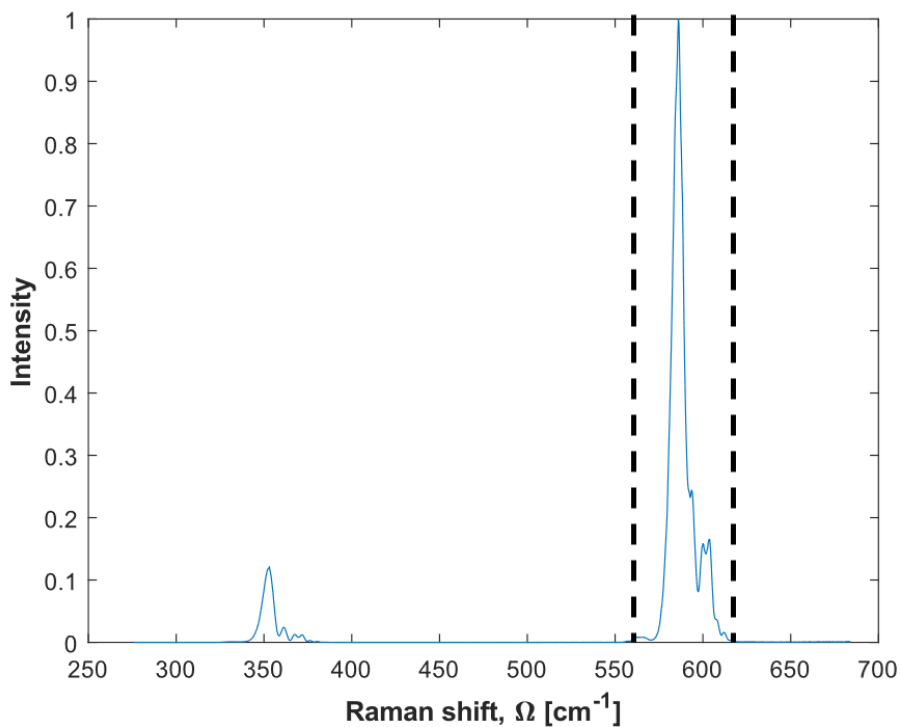


Figure 33: Pure  $H_2$  CARS at room temperature (experimental): Spectral region containing information on one  $H_2$  Raman line (slit open)

The hydrogen CARS spectra recorded using the direct probe contain a broader spectral region of useful signal. All information on one Raman line can be obtained by averaging spectrally, elevation signal-to-noise ratios, and increasing the dynamic range (this is the relative intensity range between the strongest and weakest peaks – which limits the signal-to-noise ratio of the weakest peak due to the strongest one saturating the camera). This can be seen in figure 33.

To show how the signal-to-noise ratio can be increased in resonant spectra with closer Raman lines, a case of air at room temperature with the slit closed is presented. The rotational constants and revival period of Oxygen ( $\sim 1.44 \text{ cm}^{-1}$  and  $\sim 5.8 \text{ ps}$ ) are different from that of nitrogen ( $\sim 1.99 \text{ cm}^{-1}$  and  $\sim 8.4 \text{ ps}$ ), positioning their Raman lines slightly farther away (still in the same spectral range) and ensuring their convolution when present together. Hence, the resonant spectra from air (which is a combination of  $\sim 79\%$  nitrogen and  $\sim 21\%$  Oxygen) do not show well-resolved lines and also beat across probe delays, due to the varying parts of the molecular response convolving with the probe pulse.

Figure 34 shows resonant spectra from air at room temperature recorded at a particular arbitrary delay ( $\sim 32 \text{ ps}$ ), overlaid with the best fit generated synthetically (generated through the convolution product of a model for the molecular response of air and a model for the filtered probe pulse). The fit between these two curves is not ideal, as evidenced in the high residual. This is because of the low probe power used to record this signal, which contains  $\sim 400$  counts as the maximum intensity. Due to this low signal intensity, the signal-to-noise ratio is also low, which influences the percentage of errors creeping into the measurement from the background noise. This, not only affects the accuracy of the temperature fit (expected to be  $\sim 290 \text{ K}$ ) but also the precision shot-to-shot due to the fluctuation in the background noise. This is evident from figures 34 and 35, which show an inaccurate temperature fit ( $\sim 280 \text{ K}$ ) and a high standard deviation ( $\sigma_{T_{fit}} = 10.6128$ ) in the fitted temperature over one thousand shots (1 second of acquisition with a repetition rate of  $1 \text{ kHz}$ ).

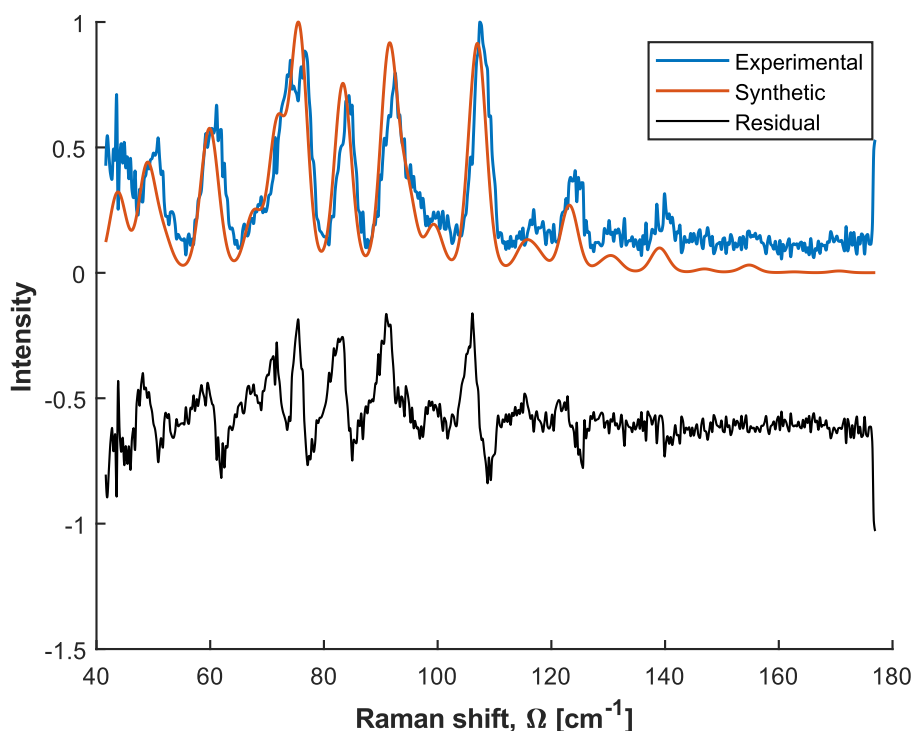


Figure 34: Blue: Resonant CSRS spectra from air at room temperature recorded at a particular delay ( $\sim 32 \text{ ps}$ ) using a probe with the slit closed with a maximum signal intensity of  $\sim 400$  counts. Orange: Synthetically modeled spectra for this delay, concentration, and temperature. Black: residual between the two curves.  $T_{fit} = \sim 280 \text{ K}$   
The probe power was attenuated in steps to decrease signal counts.

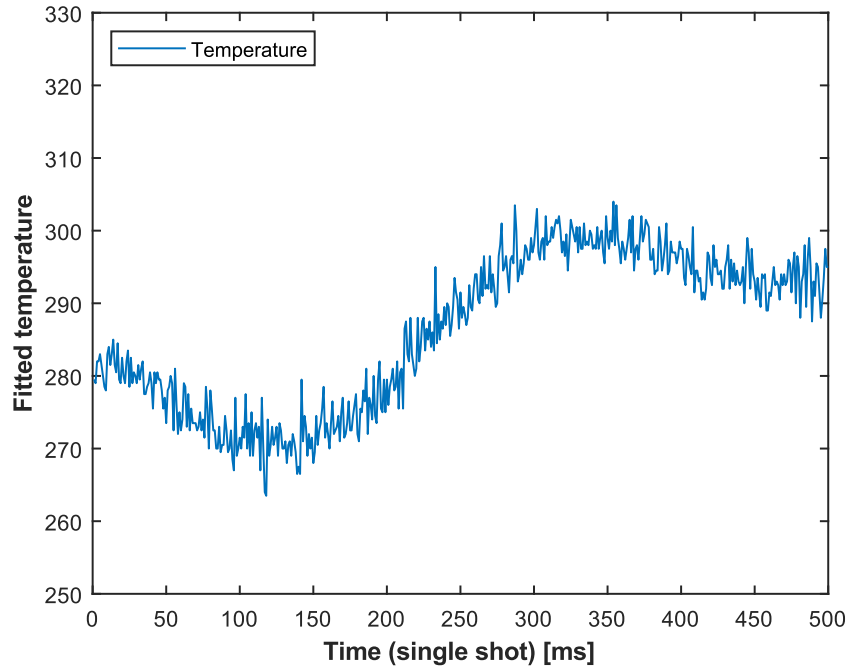


Figure 35: Shot-to-shot precision and overall accuracy of the fitted temperature with a maximum signal intensity of  $\sim 400$  counts.  $\sigma_{T_{fit}} = 10.6128$ . Each data point is a fit using the comparison in figure 34. The data is recorded at room temperature in air at a probe delay of  $\sim 32$  ps, and a repetition rate of 1 kHz.

An increase in probe power results in an elevation of the signal-to-noise ratio over the background noise, and results in a better fit, as shown in figure 36 where the maximum recorded signal count was  $\sim 12700$ . The resulting temperature fit is much closer to what is expected at room temperature ( $\sim 290$  K) and with a much lower standard deviation of fitted temperatures  $\sigma_{T_{fit}} = 1.7057$ , indicating an improved precision (figure 37).

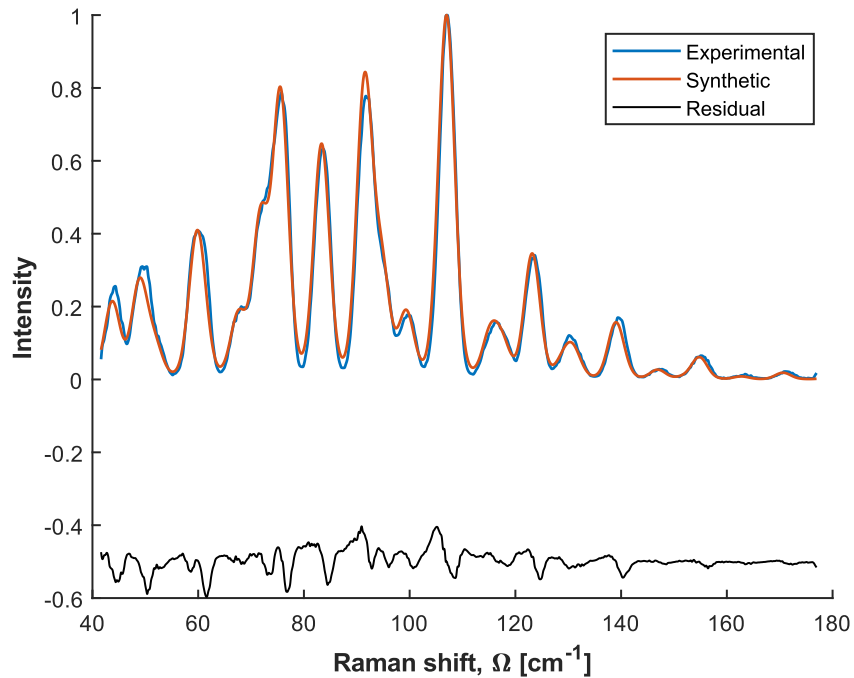


Figure 36: Blue: Resonant CSRS spectra from air at room temperature recorded at a particular delay ( $\sim 32$  ps) using a probe with the slit closed with a maximum signal intensity of  $\sim 12700$  counts. Orange: Synthetically modeled spectra for this delay, concentration, and temperature. Black: residual between the two curves.  $T_{fit} = \sim 290$  K. The probe power was attenuated in steps to decrease signal counts.

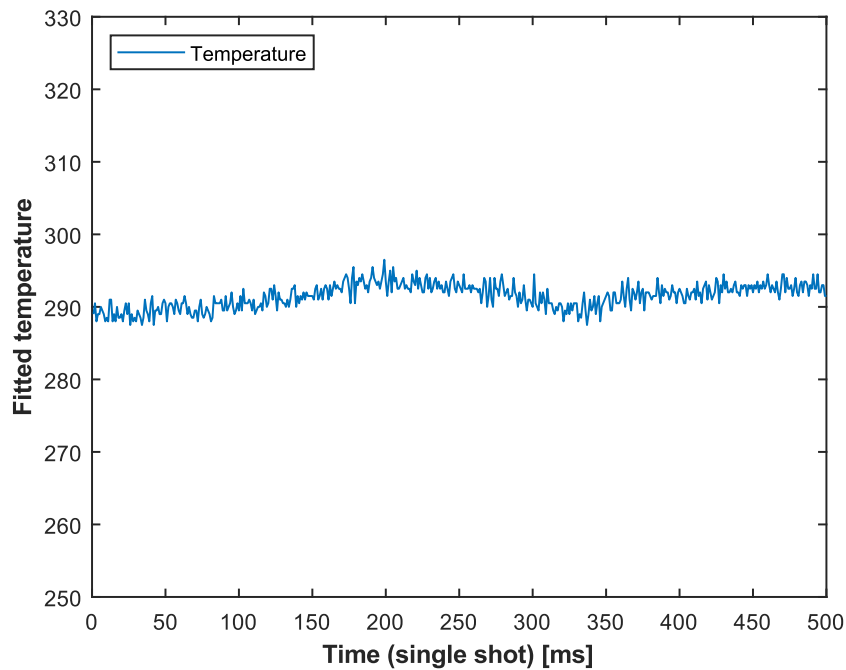


Figure 37: Shot-to-shot precision and overall accuracy of the fitted temperature with a maximum signal intensity of  $\sim 12700$  counts.  $\sigma_{T_{fit}} = 1.7057$ . Each data point is a fit using the comparison in figure 36. The data is recorded at room temperature in air at a probe delay of  $\sim 32$  ps, and a repetition rate of 1 kHz.

The resulting data shows that, with an increase in probe power, the standard deviation of the fitted temperature decreases – implying that when observing spectra containing closer resonant lines which convolve to form a continuous shape, the increase in probe power leads to a direct increase in signal-to-noise ratio and precision (and accuracy).

Hence, the CARS signal can be generated using the direct output of the SHBC, and benefits from the higher intensity in the probe pulse, as obtained when not cleaned using the 4F-filter. As mentioned before, the use of the 4F-filter results in a loss of  $\sim 70\%$  intensity in the probe pulse, reducing the maximum available power (that can be achieved without attenuation) from  $\sim 1.1$  W to  $\sim 300$  mW. This project then aims at improving single-shot precision, at the expense of losing spectral resolution (due to the extra frequencies in the probe). This loss in spectral resolution does not translate to a loss in information on Raman transitions, and hence Boltzmann distributions and temperature, *if* it can be modeled, as evidenced by CPP CARS thermometry. The main research objective of this thesis can then be posed:

***“To characterize the probe pulse at the output of the SHBC and utilize it directly for hybrid fs/ps CARS, in order to maintain an efficient use of the photon content of the laser pulses and improve shot-to-shot precision.”***

And, critical research questions can be posed that help in completing the objective:

- Can the probe pulse be characterized using the CARS signal as a correlation method?
- What are the accuracy and precision of CARS thermometry when performed with such a probe pulse, as compared to when the 4F filter is employed?

# 5

## Methodology: Characterization of the probe pulse

The increase in the intensity of the CRS signal helps, only if the probe is fully characterized in its phase information (frequency and time), and the CARS signal can be reconstructed synthetically using the temperature- and concentration-dependent molecular response – and the synthetic representation of the probe. This characterization was executed in generally three steps:

1. Discretize the probe pulse in frequency using the 4F-filter and read these frequencies.
2. Obtain relative phase information (time arrival), and intensities per discretized frequency position.
3. Construct the pulse synthetically to use for fitting CARS/CSRS spectra.

The main objective behind these general steps was to characterize the chirp contained within the pulse. The motive behind the discretization of the probe in the frequency domain was to obtain tangible discretized frequency segments, to further map their respective time signatures. This combined information, then, fully represents the chirp within the pulse and is sufficient to reconstruct it, when combined with the relative intensity per frequency.

### 5.1 Discretization and characterization of the frequency information

The first step was to characterize the frequency content in this pulse using the 4F-filter. The mechanical slit at the 4F-filter was employed to discretize the spectrum into 20 segments, equally spaced by 30 microns with the opening in the slit also 30 microns (hereby called slit size). This resulted in a discretization in frequency with a nearly uniform step size of  $\sim 2 \text{ cm}^{-1}$  (shown in figure 38). Two different methods were employed to detect each discretized frequency: Firstly, by using the home-built spectrometer discussed in the chapter on the experimental setup and measuring the resulting discretized parts of the probe directly in the frequency domain. Secondly, as a validation method, the pure-rotational nitrogen CARS signal was also acquired at room temperature, generated per discretized segment of the probe, to read the frequency content from each of these slit positions

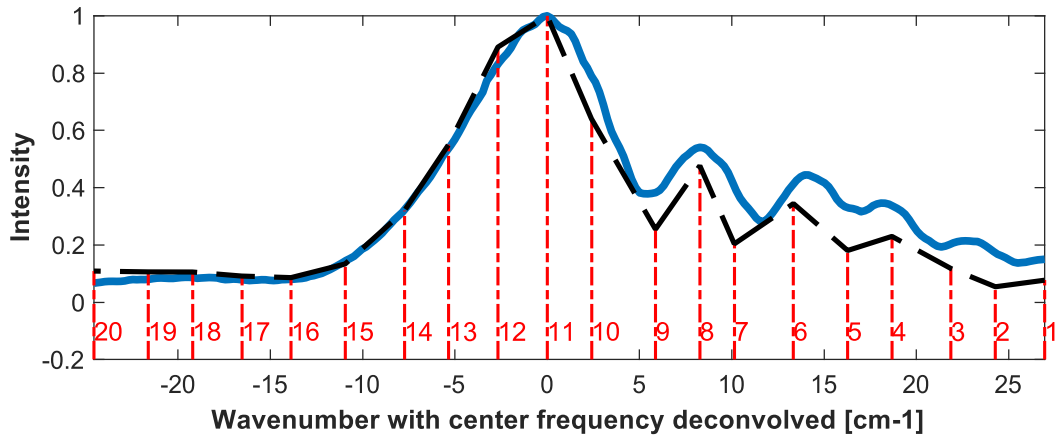


Figure 38: Comparison of the reconstructed probe profile using discretized frequency data (black, dashed lines) and the whole probe (with the slit open) imaged on the camera (blue, continuous line). A total of 20 points were recorded with a step size of  $\sim 2 \text{ cm}^{-1}$ . Each number in red corresponds to a slit position in the Fourier plane and hence, a discretized frequency point.

Figure 39 shows how the resonant Raman lines are shifted by the instantaneous carrier frequency in the probe after the discretization in the Fourier plane. This was needed to calibrate the spectrometer to measure even the direct probe (as in the first method). Moreover, if the signal is scattered with a probe part at a different frequency (from a different discretized segment, due to uncertainties and variations in the path direction of the probe beam), the CARS signal would get shifted in the sensor by the same amount and not anymore reflect a shift in the actual discretized probe carrier frequency. Hence, these two methods go hand-in-hand to acquire strong data, by validating each other.

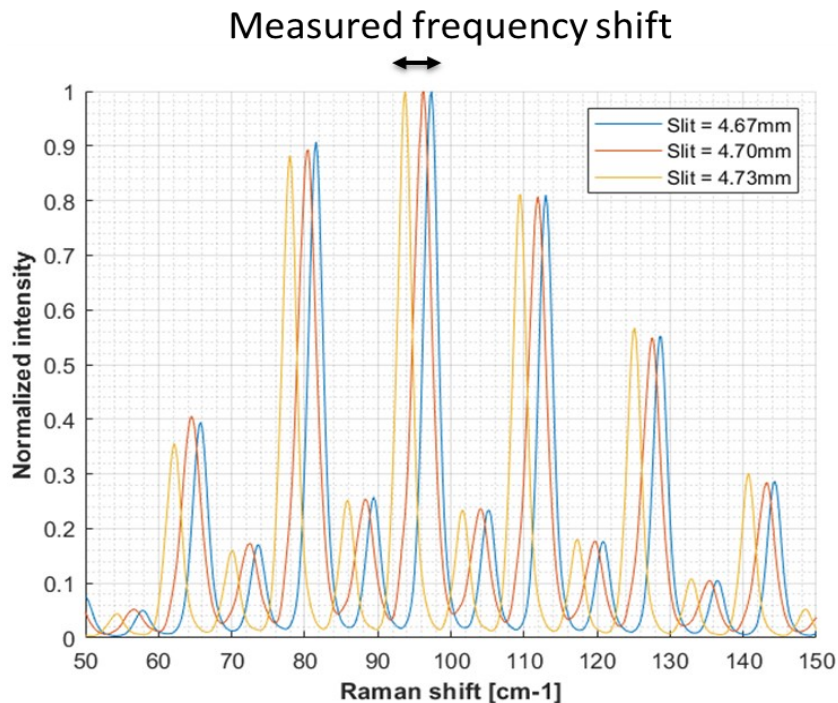


Figure 39: Nitrogen spectra at room temperature recorded using probes generated from three different (and consecutive) slit positions in the Fourier plane. The absolute value of these positions does not matter as much as their relative displacement, which is 30 microns ( $\sim 2 \text{ cm}^{-1}$ ). As the frequency passed through the 4F – filter increases, the spectra shift to the right.

Once an accurate estimate of the discrete frequency segments in the probe was finalized, the experiment measuring the direct probe segments on the camera was used to also capture the relative intensities of each discretized segment. This was done by recording the maximum intensity value observed by the camera at each probe segment. The limit on the lowest slit size possible is set by small abrasions in the slit in the Fourier plane, which leak intensities from surrounding spatial locations at this plane. A step size of 30 microns guarantees minimal leakage from these abrasions and is fine enough to capture the frequency domain profile of the probe, as shown in figure 38. With this data compiled, the frequency information per discretized point can be visualized as shown in this figure and the reconstructed probe follows the trend set by the experiment that imaged the probe directly without filtering in the Fourier plane, implying an agreement between the “discretized” and “continuous” experimental recordings of the probe spectrum.

## 5.2 Characterization of time (– and full phase) content

With these discretized points obtained, their respective time-arrival information can be characterized. This was done by measuring the arrival time of each discretized frequency with respect to the pump/Stokes pulse. This combined set of time and frequency information can then represent the full phase information on this probe pulse.

The time-arrival information adds phase information to the already measured discretized frequency information. When treating the constituent frequencies as sinusoids, equation 12 explains the phase information contained within each sine wave. The frequency is generally described as the instantaneous derivative of the phase of this pulse. If we ignore the spatial frequency (as it is a direct result from knowing the temporal frequency and the speed of light), then the only unknown to this equation of describing a frequency in the probe pulse is  $\phi$ , or the initial phase angle, per frequency. This comes as a direct result of knowing the temporal position of each frequency and hence the time-arrival information completes the ensemble of phase information.

$$y = A \cdot \sin(\alpha); \alpha = kx - \omega t + \phi, \text{ and } \omega = \frac{\partial \alpha}{\partial t} \text{ (and } k = \frac{\partial \alpha}{\partial x}) \quad \text{Eq.12}$$

When the slit filters frequencies in the Fourier plane, it essentially applies hard edges to the pulse in the frequency domain (top-hat filter). This, in turn, has some effects on the time-domain profile of the probe pulse:

1. The pulse is now longer in time (FWHM) due to fewer frequencies that make up the pulse, from the time-bandwidth product.
2. The shape is that of a  $\text{sinc}^2$  profile, due to the top hat applied in the frequency domain.
3. An airy pattern is created, as shown in figure 40.

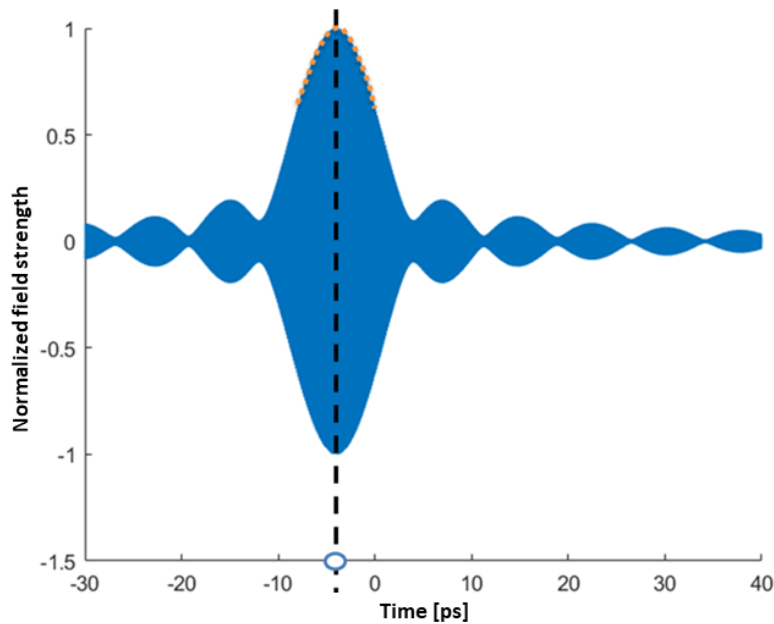


Figure 40: Simulation of the time-domain response to the filter in the Fourier plane. The electric field of the pulse in time now has a longer duration, a different profile (to the incoming Gaussian pulse), and forms a diffraction pattern, generally called an "Airy pattern". The time-arrival of the maximum intensity of this profile is important and the orange dotted line shows the area needed to be recorded to obtain this information.

An effective way of mapping the time-domain intensity profile of this pulse is to use the intensity of the non-resonant signal as a way of correlating to the intensity of the probe pulse. A non-resonant signal is only generated from the laser pulses when the pump/Stokes and probe pulses coincide spatially and temporally. Moreover, the intensity of the four-wave mixing process (detailed in equation 8), depends linearly on the intensity of the probe pulse used to generate it. Hence, by delaying the pump/Stokes pulse across the probe pulse in time, and recording the non-resonant signal generated, the intensity of the probe pulse can be extracted as a function of pump/Stokes pulse delay, and hence, time. Figure 41 attempts to detail this procedure. The time-arrival of the maximum intensity of this profile is consistent with the time-arrival of the discretized frequency that generated this pulse. The limiting time-step (or resolution) for this experiment is the minimum step size on the delay stage ( $\sim 250$  fs), as this is larger than the pump/Stokes pulse duration (35 fs). Additionally, to avoid imaging any interference from the resonant signal, Argon is used as the gas to record non-resonant signals as Argon does not produce any resonant signal (due to it being a single atom) and it also does not react due to its inertness. A resonant signal is undesired here, because of its variance with time in a manner that would not reflect the behavior of the probe pulse.

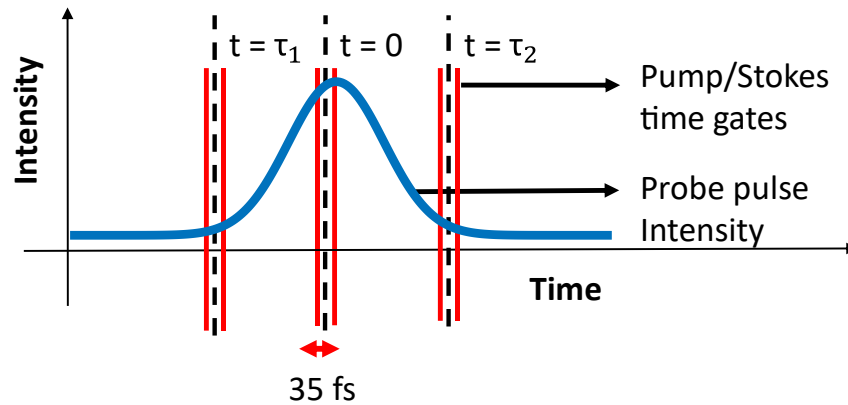


Figure 41: Method of correlation of non - resonant signal intensity at different pump/Stokes pulse delays to the probe profile intensity in time: Positioning the pump/Stokes pulse (duration ~65 fs FWHM) at multiple delays ( $t = 0, \tau_1, \tau_2$ ) and recording the intensity of the non - resonant signal subsequently generated.

A demerit of using the non - resonant to correlate the probe profile is the use of four-wave mixing intensity. Whereas, CARS is powerful due to its spectral information, depending only on the unvarying molecular information. This is because the intensity of the non-resonant signal depends on a multitude of factors affecting the probe volume, for example, any concentration changes, or turbulence-caused instabilities in the air that steer the beams. This effect is called beam-steering and occurs due to any change in local refractive indices that the laser pulses are subject to, which causes the beam to move or “steer” and result in irregularities in the signal at the camera. These irregularities are evidenced in figure 42 and are the significant limitation to this method of correlation.

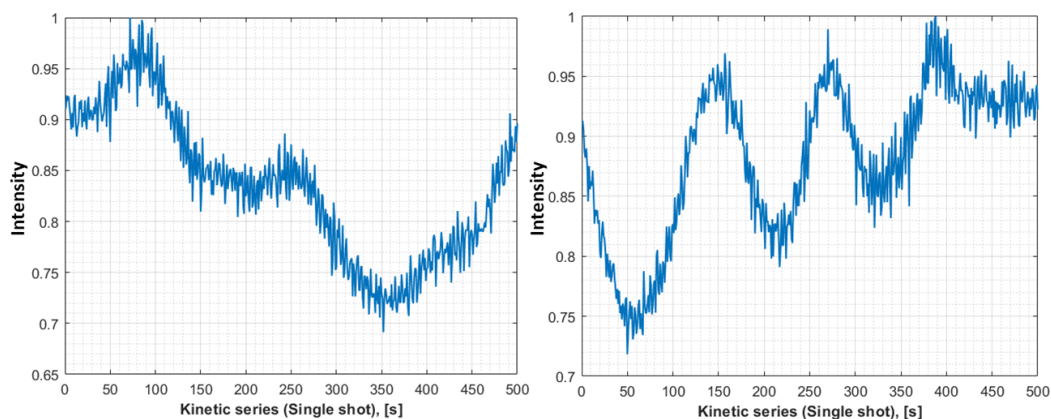


Figure 42: Fluctuation of the non - resonant signal shot-to-shot, leading to errors in measurements at an arbitrary slit position. This is mainly due to flow instabilities near the burner and in the non-resonant gas flow (Argon) causing beam-steering. Each figure is a repetition of the recording at a different probe delay (the consistency of these irregularities is important). Each data point in each figure is a binned value of all the non - resonant signal content seen at the camera.

These problems occur only due to a variation of the flow in the probe volume. Hence, the production of the non-resonant signal from a solid (and transparent material) such as glass could generate much better data. However, in this work, it was decided to work with a redesigned flow of Argon to produce better (more stable) non-resonant data. With this knowledge, the correlation experiment can be redesigned to have:

1. A low enough flowrate of Argon to reduce the instabilities significantly.
2. A large enough flowrate to avoid entrapping air (air would generate a resonant signal).

3. A long enough capture time (combination of exposure time per shot and number of frames/shots) to dampen out any further instabilities.

With a flowrate of Argon of 0.25 L/min, 500 frames per acquisition, and an exposure time of 10 ms (effectively summing up 10 pulses), the following time-fluctuation of the non-resonant signal was recorded (figure 43):

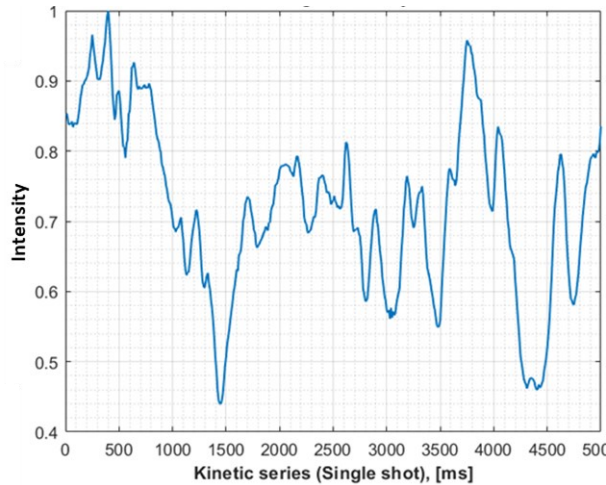


Figure 43: Fluctuation of the non - resonant signal shot-to-shot at an arbitrary delay and slit position. This is mainly due to beam-steering. Each data point is a binned value of all the non - resonant signal content seen at the camera. Total acquisition time: 5 seconds (500 frames per acquisition and an exposure time of 10 ms per frame).

With these settings, a scan of the pump/Stokes pulse across the probe pulse can be performed as mentioned in the previous sections, and the resulting data yields a good  $\text{sinc}^2$  fit (as shown in figure 44), indicating not only that the data resembles expected results, but also that this correlation method is a very useful tool for characterizing time information.

These fits also yield important time-arrival information for each discretized frequency. In figure 44, the arrival times of the center frequency are shown to be zero because this is regarded as the reference point for all the arrival times. In this figure, it is also shown from which part of the conjugation in the SHBC this was generated. The center frequency can only be generated from the center of the conjugation as the distorted shape of the conjugate disks prevent the formation of this frequency at any other portion of the SFG and instead lead to “sidebands”, or higher frequency terms as discussed before (see the section on the SHBC in the chapter on the experimental setup).

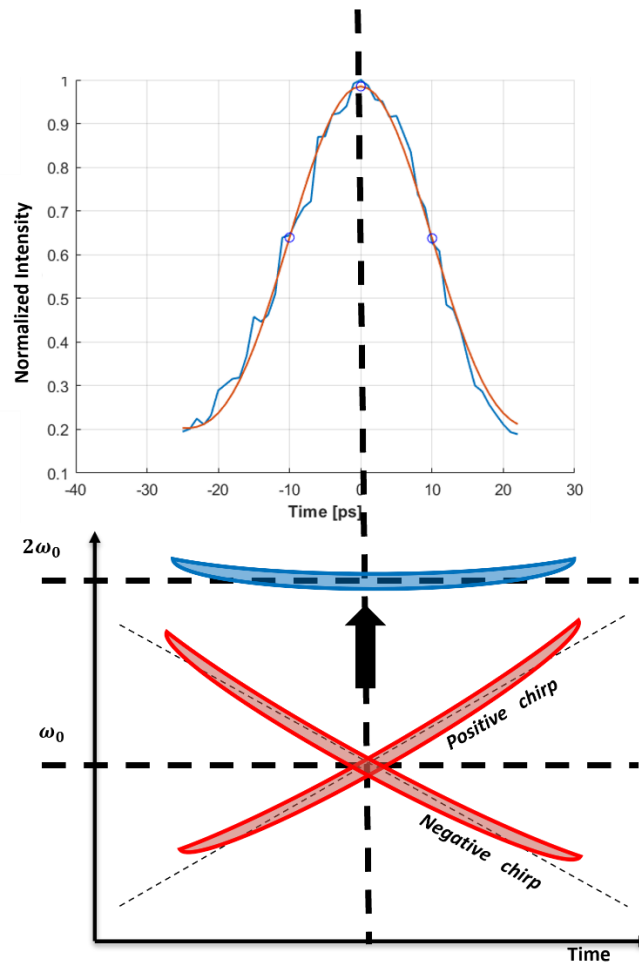


Figure 44: (Top) The temporal shape of the probe pulse obtained from the non-resonant signal produced by Argon at different probe delays: resulting from scanning the pump/Stokes pulse across the probe pulse in time (blue), and the corresponding  $\text{sinc}^2$  fit (orange). The black dashed line marks the location in time of the maximum intensity, which is an important time–arrival information (here, normalized to zero for convenience). This scan was recorded from the probe generated when the slit position passes through the main lobe in the probe as the discretized frequency (position 11 in figure 38). (Bottom) Conjugation in the SHBC: The two red disks represent the broadband pulses, which undergo SFG to produce the narrowband pulse (violet disk). When this conjugation is imperfect, the center frequency of the probe can only be generated from the center of this conjugation.

In figure 45, the Argon scans and respective time–arrival information from other frequencies are overlapped with the diagram of the conjugation in the SHBC. Precisely, the arrival times from the first and third sideband are of interest (these correspond to discrete segments 8 and 4 respectively in figure 38). As the selected frequency in the probe pulse increases, the time – locations in the conjugation diagram from where they can be formed must grow wider and wider from the center in each direction. This can be seen from figure 45, where the frequencies present in the third sideband of the probe (higher than the first sideband in frequency value) appear at wider time locations in the conjugation diagram, on either side. The positions of these local maxima in the Argon scans are detected by a program that evaluates the prominence of these peaks. Hence, the results of this correlation are, at least, physical and the data from each discretized frequency follow nicely from one another.

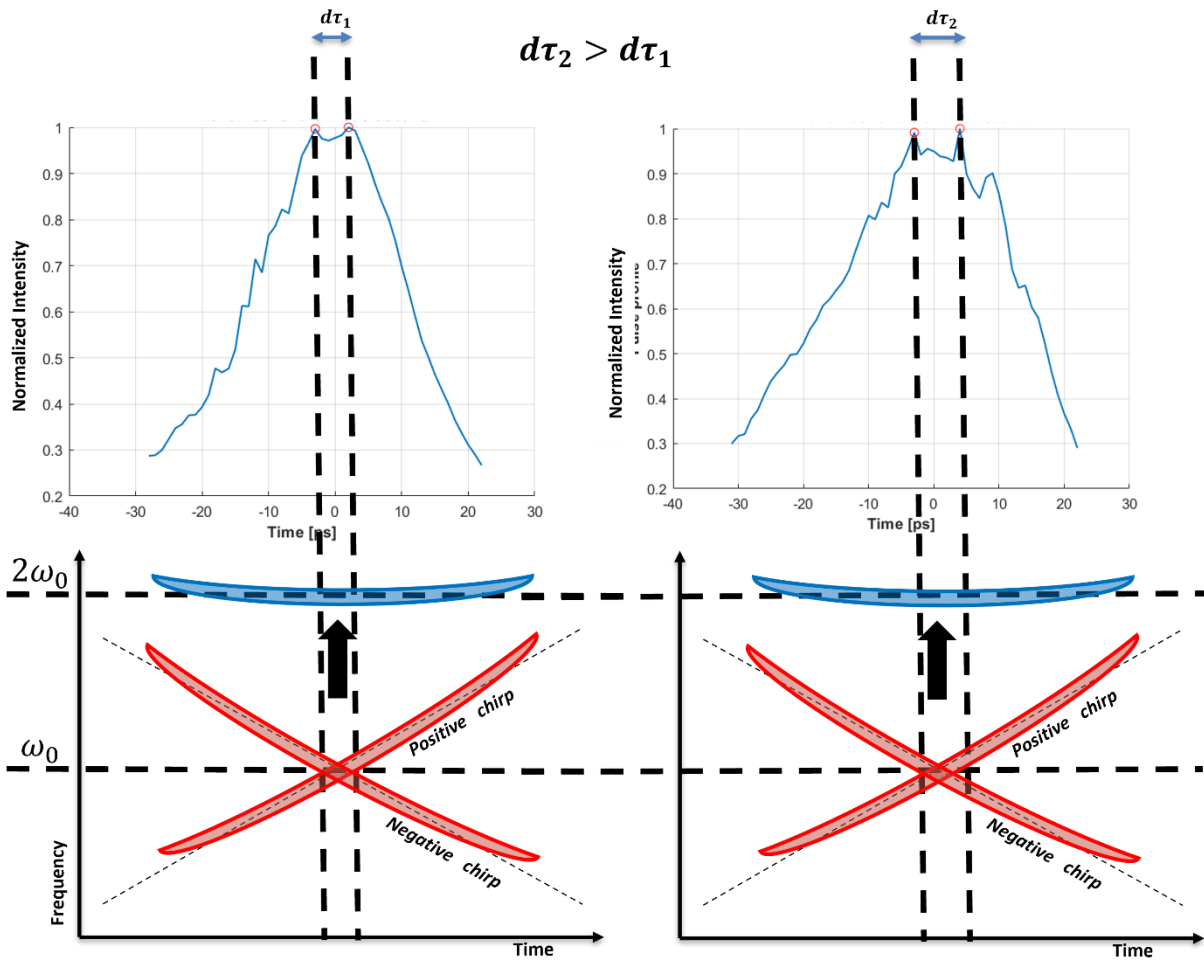


Figure 45: The temporal shape of the probe pulse obtained from the non-resonant signal produced by Argon with time-arrival information (top) and the conjugation diagram in the SHBC (bottom) from the first sideband (discrete position 8, left figure) and the third sideband (discrete position 4, right figure). The two red disks represent the broadband pulses, which undergo SFG to produce the narrowband pulse (blue disk). When this conjugation is imperfect, the center frequency of the probe can only be generated from the center of this conjugation. Subsequently, high frequencies appear at wider and wider time locations on either side of the center due to the higher-order non-linear chirp imparted to the pulses in either arm of this conjugation. Here, this translates to  $d\tau_2 > d\tau_1$ .

### 5.3 Modeling the synthetic representation of the probe pulse

With the full phase information acquired on all the discretized points, only the relative strength of each frequency (intensity) was required. This was measured by imaging the attenuated probe at each discretized point separately on the camera and composing the recorded data into one intensity value per point. Then, all the information required to build a synthetic model of the probe can be fed to an interferogram model which simulates the interference between the pulses “generated” at the multiple slit positions. This flow of data can be visualized through the flowchart in figure 46.

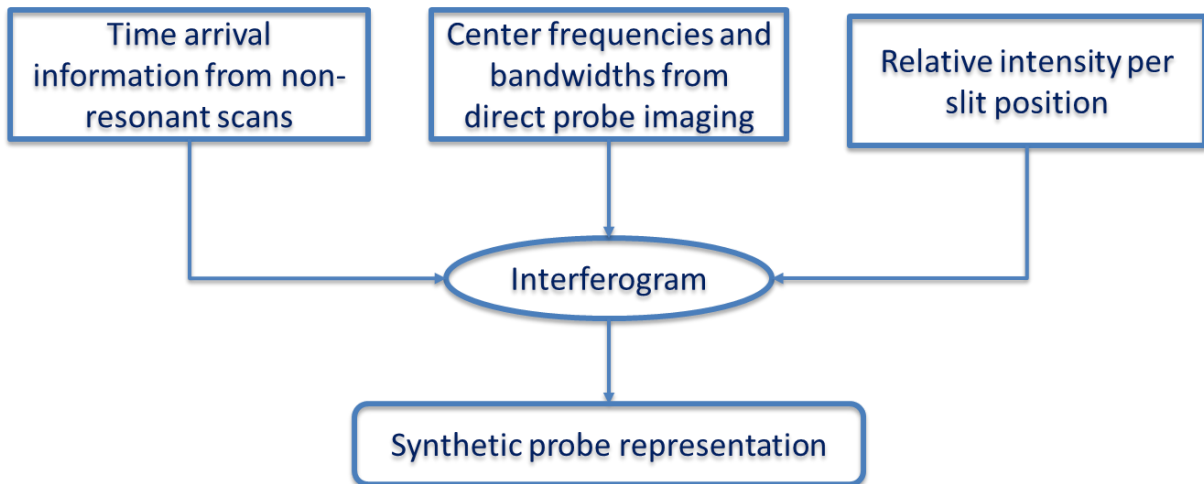


Figure 46: Flowchart of the phase and relative intensity information flow into the interference model and the resulting synthetic probe modeling.

The model works through a linear addition of time-domain pulses (assumed to have been formed after the filter in the Fourier plane) with respective phase and intensity information generated from different slit positions, as shown in figure 47.

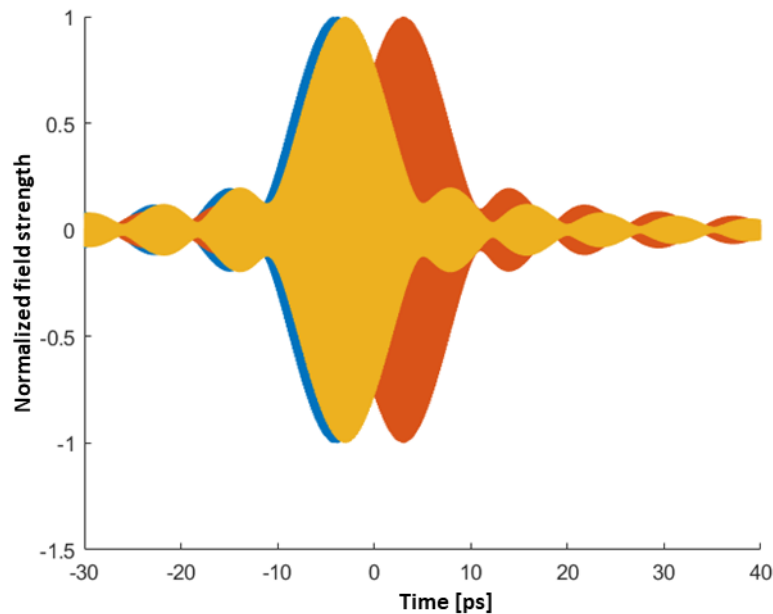


Figure 47: Working of the time-domain interferogram model. Each color represents a pulse generated at a different slit position, containing different frequency information and as can be seen, time arrival.

Hence, this continues as a time-domain model and builds a synthetic pulse by, First: adding sinusoids at the different frequencies,  $\omega_i$ , in the bandwidth passed by the slit,  $B$ , at each frequency segment with equal intensity and, second: adding the pulses built from the frequency segments of each slit position, attributed with an initial phase,  $\phi_j$  (coming from the time-arrival), and relative intensity of this discretized segment,  $A_j$ . This is shown in equation 13, which follows directly from equation 12 after the acquisition of the phase data, where the exponential function  $e^{i\alpha} (= \cos\alpha + i\sin\alpha)$  represents an electromagnetic field with a single frequency, and a pulse is generated through the addition of these waves. The final probe pulse

is generated through the intensity-weighted addition of multiple pulses at the discretized frequency locations,  $j \rightarrow 1:20$ .

$$\sum_{\forall \phi_j} \left( A_j * \sum_{\forall \omega_i \text{ in } B} \left( e^{2\pi(\omega_i t + \phi_j)} \right) \right) \quad \text{Eq.13}$$

The resulting synthetic probe has a similar FWHM as compared to the experimentally recorded time profile of the probe with the slit fully open (figure 48 left). However, the frequency domain representation (generated by performing a discrete Fourier transform on the time-domain representation) is skewed, because of heavy (and incorrect) interference.

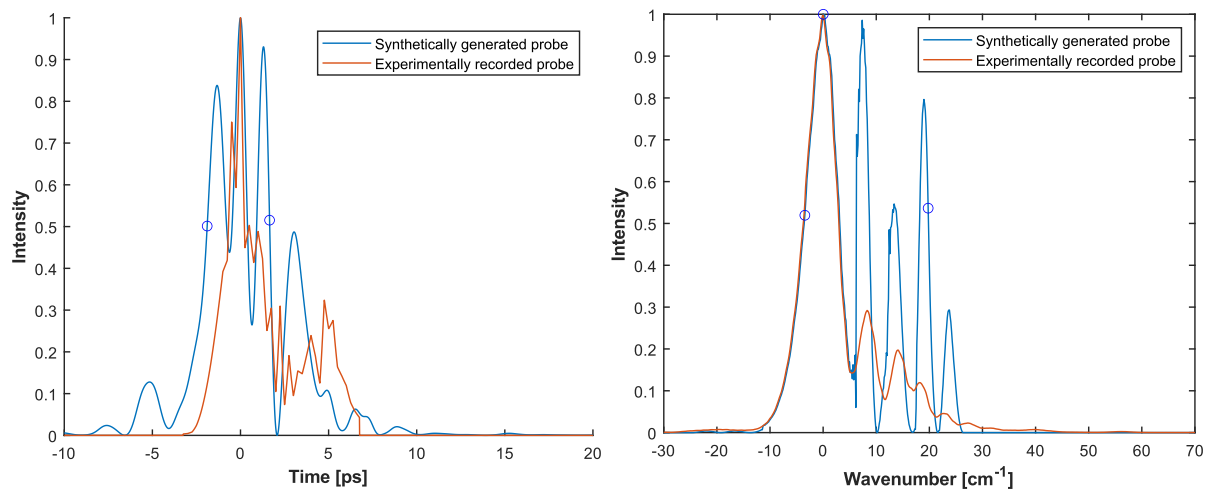


Figure 48: (Left) Comparison of the time-domain representations of the pulse recorded experimentally by performing an Argon scan with the slit fully open (Orange), and a synthetic representation created by the interferogram model. Blue circles show the time domain FWHM of the synthetic pulse. (Right) Comparison of the frequency-domain representations of the pulse recorded experimentally by imaging the attenuated probe directly on the camera with the slit fully open (Orange), and a synthetic representation created by the interferogram model. Blue circles show the frequency-domain FWHM of the synthetic pulse.

## 5.4 Validation of the synthetic probe pulse model

This pulse and its phase information could be accurate enough to perform CARS thermometry. This can be validated in the same way by generating a CARS spectrum and attempting to fit temperatures: by replicating the scattering process from different molecular responses using the synthetically generated probe pulse and comparing it to experimental data. The results of some of these experiments for validation were used to motivate the objective behind the thesis before, and here, it will be discussed: the various experiments performed, along with their use as validation for the synthetic probe pulse model. Mainly, four different environments were probed using both the filtered and direct (from the SHBC) probe pulses: Room temperature nitrogen, air, and hydrogen, and a hydrogen flame seeded with 50% nitrogen by volume. The flame, nitrogen, and air spectra were all recorded on the CSRS side of the coherent Raman spectrum and the pure hydrogen was recorded on the CARS side. The reason for this is due to the spectral coincidence of the probe with the spectra, as seen on the camera, and is explained in detail in the chapter on important observations. The results from the flame will be discussed later as this is the final test case and aim of the work. The room temperature experiments were carried out to obtain a map of the beating of the resonant spectra of these different environments across probe delays. This time-variation of frequency information or, simultaneous time- and frequency-resolved CSRS measurements are acquired by generating

the CSRS spectrum with the probe and pump/Stokes pulses positioned at varying delays and recording spectra at each delay. Such a spectrum consists of 1000 frames at 1kHz repetition rates, measuring across 1 second in total with an exposure time per frame, set to capture just one pulse (~1 ms). This is repeated for a total of 81 probe delays ranging from ~26.77 ps to ~46.78 ps with a step size of 250 fs (set by the delay stage). Figure 49 shows the experimental nitrogen spectrochronogram at room temperature with the slit open and a reconstruction of the same using the synthetic probe pulse. The characteristics of this experimental spectrochronogram, and the differences as compared to a similar spectrochronogram generated with a probe pulse produced through 4F-filtering, were explained in the section on the research objective. Figure 49 shows the extent of the capture of the beating of the resonant Raman lines across probe delays. A couple of different delays are selected, and their spectra are plotted in figure 50, which shows the differences between the two. The spectrochronogram captures some effects, such as the periodicity coming from the nitrogen molecular response, and the convolution of even and odd lines at specific delays.

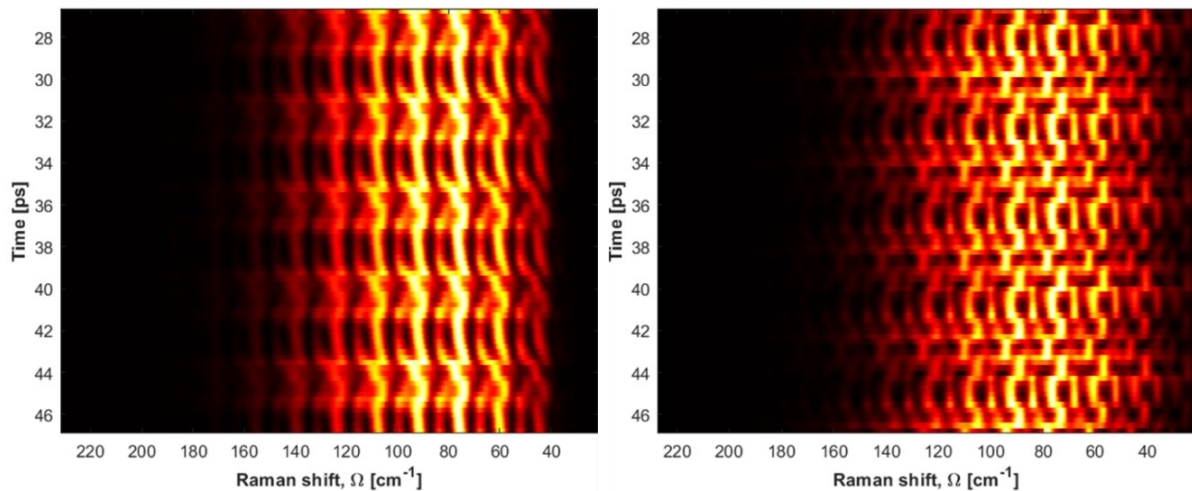


Figure 49: Comparison of room temperature nitrogen CSRS spectrochronograms at room temperature: Experimental on the left and synthetic reconstruction on the right. For a color bar, refer to figure 31.

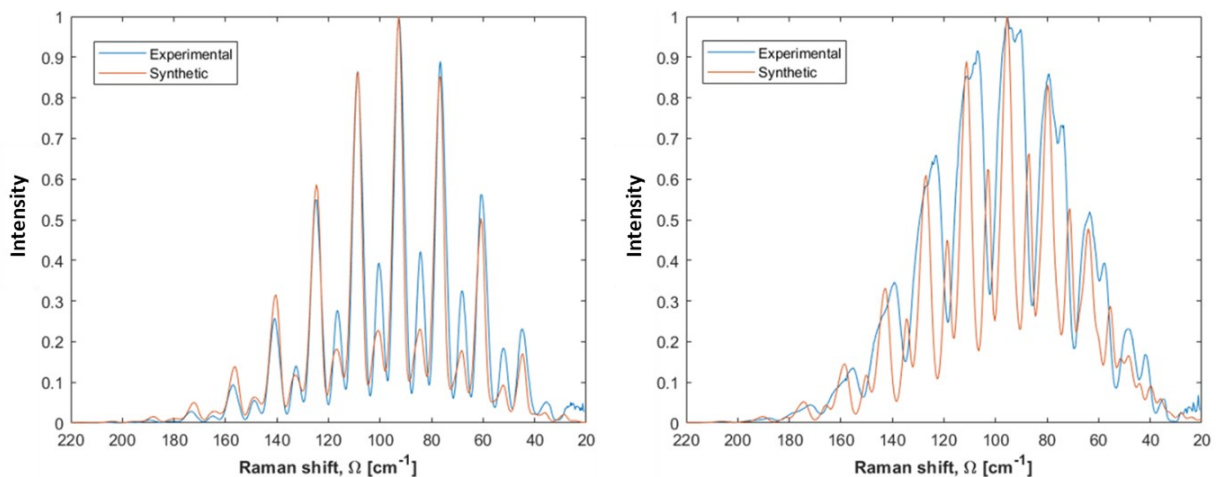


Figure 50: Comparison of nitrogen CSRS spectra at room temperature. The two figures represent two different delays (left: 29.52 ps and right: 26.76 ps), both of which can be seen on the spectrochronograms in figure 49. In each figure, the experimentally acquired spectra (blue) are compared to the synthetically generated spectra for that delay (orange).

This methodology looks very promising and some of the features in the beating pattern of  $N_2$  are captured. The synthetic spectra also look closer to the experimental ones, and some (inaccurate) temperatures can already be extracted from them. These fits are not shown yet

as it is more interesting after the next chapter. This decent capture also, importantly, validates the interferogram model. It was decided to improve this phase information further, using it as an initial step.

## 5.5 Optimization of the acquired phase information

While the data from the synthetic reconstruction suggest that the interferogram model works correctly (as can be seen from the similar FWHM of the pulses), the phase information acquired from the characterization is hypothesized to be slightly incorrect. Moreover, the interference between pulses generated at discretized frequencies is very sensitive to their relative phase information, down to even 50 fs (the pump/Stokes FWHM used for the correlation measurements was found later to be ~67 fs). This implies that the fits generated by the correlation of the non-resonant signal (such as figure 44) have small errors that have crept in from the errors in each measurement. Additionally, data such as those in figure 45 cannot be fit using a  $\text{sinc}^2$  curve, as they deviate from this shape due to the impact of two arrivals within the duration of the pulse. The errors that are consequences of these findings cannot be avoided easily and hence the final step before getting accurate phase information is an optimization that tunes the acquired phase data to achieve certain objectives. The objectives for this optimization were chosen to be a sum – residual value from each of the comparisons of the time and frequency domain representations of the probe pulse. The residuals from these curves are shown in figure 51. This forms a two-objective optimization and can be solved using a Pareto front, such as the one in figure 52, which attempts to find the best trade-off between the minimization of each objective.

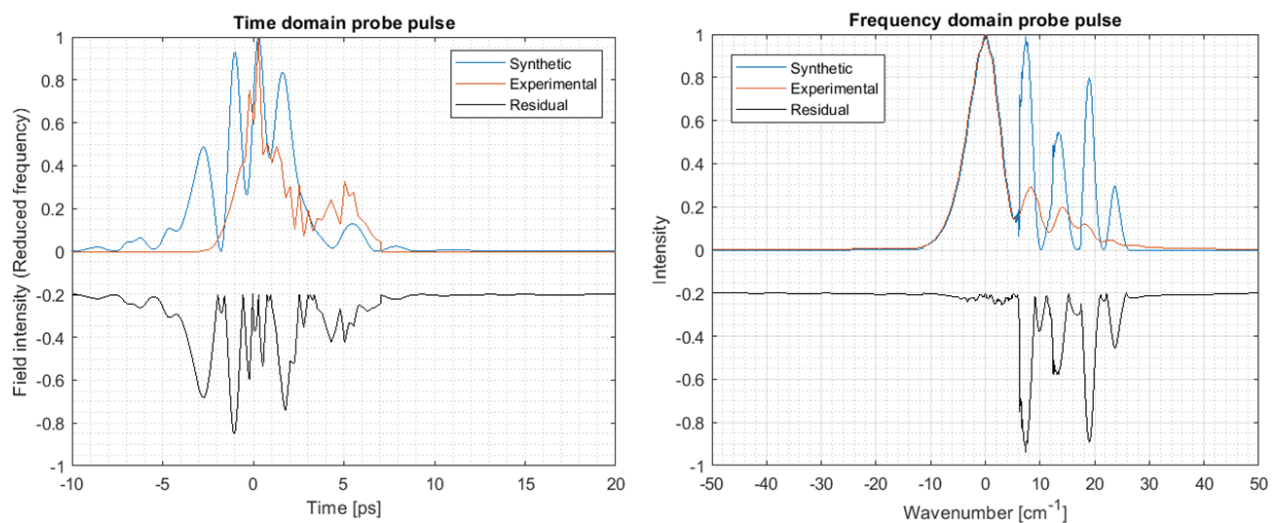


Figure 51: Two objectives to minimize, formed from the residuals of the time domain representation comparison (left) and the frequency domain comparison (right). The black curve shows the residual between the experimental (orange) and the synthetic (blue) curves in each figure.

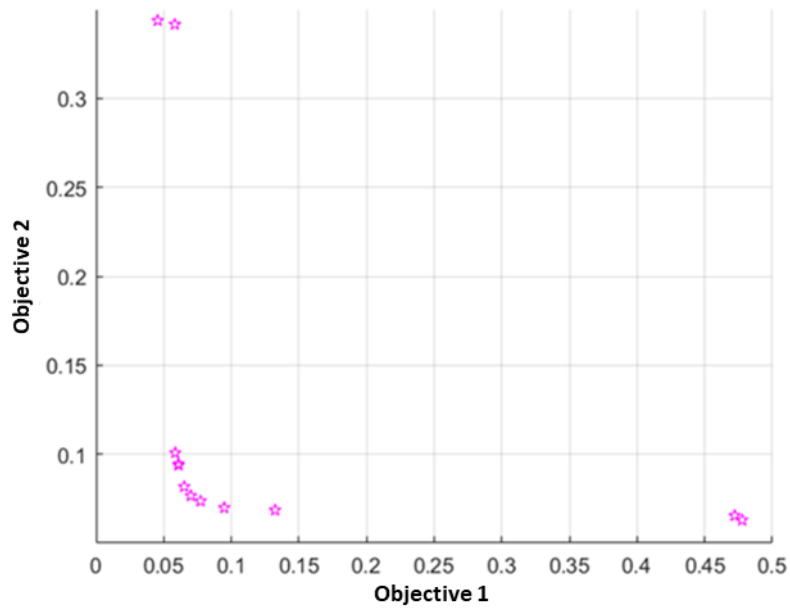


Figure 52: A Pareto front formed from the minimization of the two objectives.

An additional objective was included, namely: to minimize the residual for one repetitive period of the nitrogen spectrochronogram. Each horizontal line in the spectrochronogram can yield a residual (figure 53), and the summation of all the residuals across one repetitive period was set as an objective. With three objectives, a Pareto surface is now generated (figure 54), which is then a trade-off between three objectives.

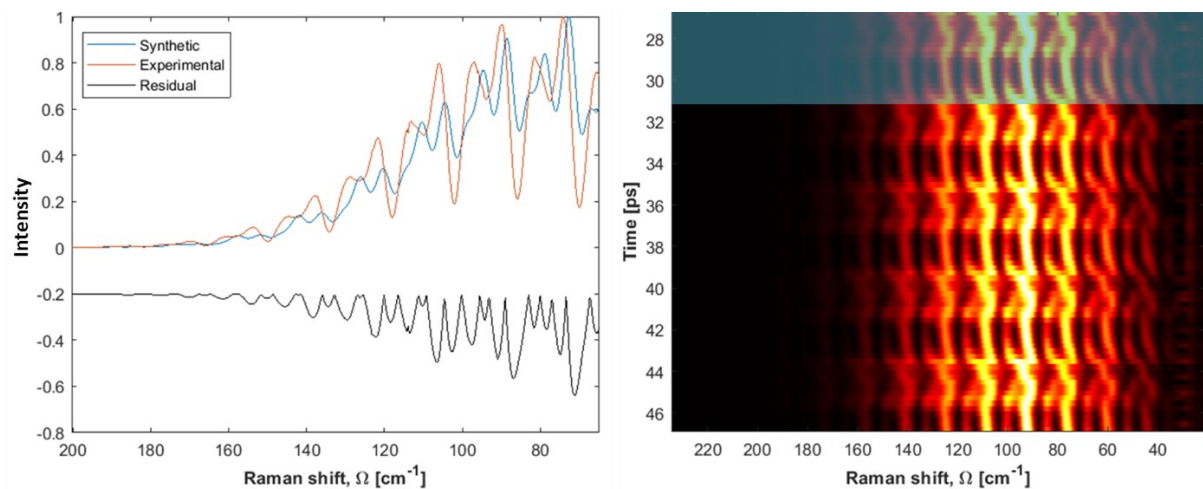


Figure 53: One repetitive period of the nitrogen CSRS spectrochronogram at room temperature was used to set an objective, using the residual computed at each delay. On the left is a residual from one such line (30.77 ps). For a color bar, refer to figure 31.

These objectives guarantee the similarity of the pulse with the experimentally recorded data for the probe with the slit fully open, while also allowing for inaccuracies in these measurements of the time and frequency by guaranteeing compensation of these errors by equalizing the spectrochronogram, which also contains valuable phase information on the probe.

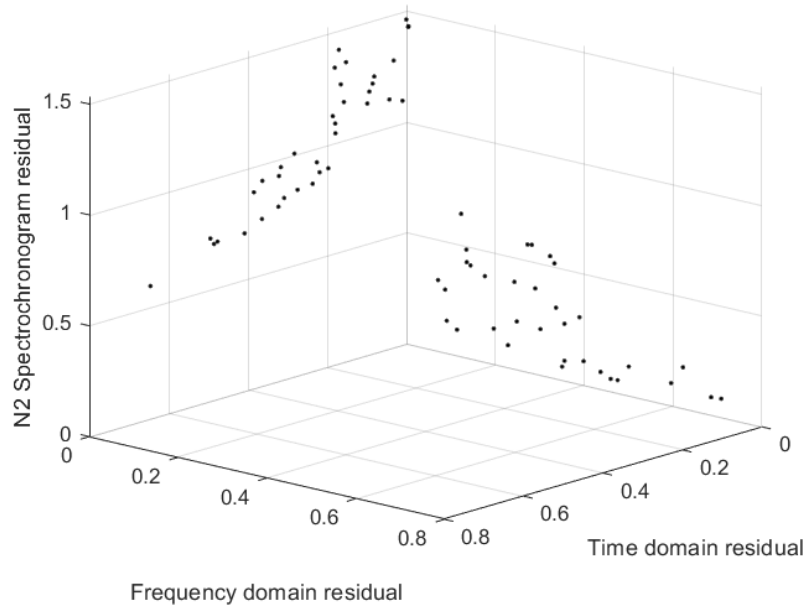


Figure 54: A Pareto surface generated from the minimization of three objectives, namely, the time and frequency domain residuals and the  $N_2$  spectrochronogram period residual.

The controllable inputs to the optimization are called design parameters, which in this case are, the arrival times per slit position, and the partial intensity per “conjugate” arrival. This constitutes a total of four design parameters per discretized frequency position, and they are detailed in figure 55.

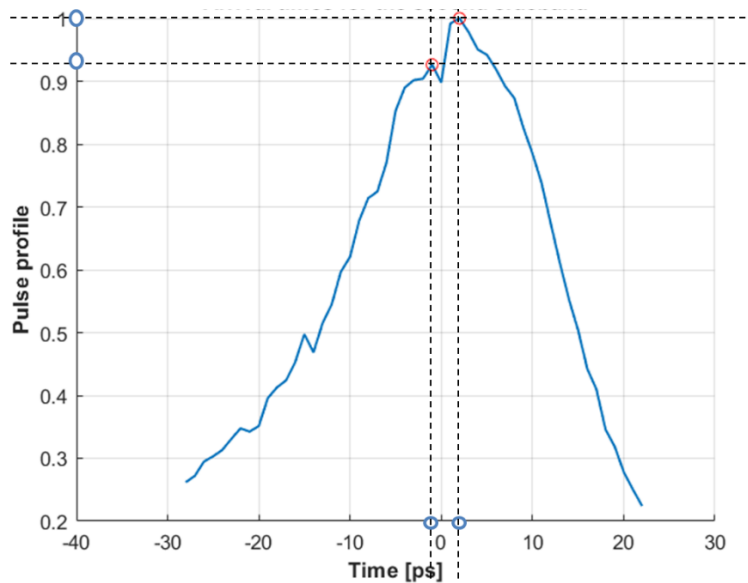


Figure 55: Design parameters per discretized frequency: Arrival times (vertical lines, points marked on the x-axis) and partial intensity per arrival (horizontal lines, points marked on the y-axis) marked on the temporal profile obtained from the correlation using the non-resonant signal, obtained for the second sideband or the discretized position 6 in figure 38.

To reduce the total number of design variables that influence the total computational time for the optimization), the probe spectra measured directly on the camera, decomposed into synthetic windows, were used as frequency information instead of the discretized information in figure 38. The spectra are divided into six windows which can be easily correlated to the phase information from the Argon scans. The result is a six-probe model, as shown in figure 56, and contains 20 design variables in total. (The center frequency and its

phase information are not variables, rather, the remaining points are all calculated relative to the center).

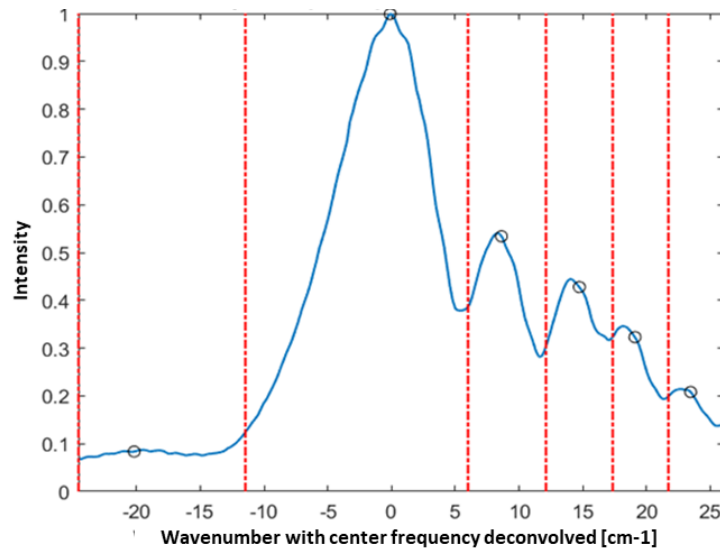


Figure 56: Synthetic windows placed on the experimentally recorded probe spectra, decomposed into windows, and resulting in a six-probe optimization model,

Constraints to ensure the physicality of the optimized results were then employed to the arrival times of each sideband. They restricted the arrivals of higher sidebands to physical values (which was elaborated using figure 45) by limiting the distance (in time) between two arrivals of the same sideband to the distance between those of the subsequent higher sideband (essentially setting this as the upper limit).

Additionally, the nitrogen spectrochronogram needed to be initialized. The objectives of residuals from the time and frequency domain representations only depend on the characterized phase and intensity information in the probe. The residual calculated from the nitrogen spectrochronogram, however, requires a convolution with the molecular response. This response depends on temperature further, which needs to be initialized and set as a constant.

Moreover, the combination of all the optical equipment in the setup also creates an effective additional linewidth in the resonant spectra observed (can be seen in figure 57, where the slit is closed). This is termed the “instrument function” and is crucial to the degree of convolution of different rotational Raman lines, especially when spectra are recorded with the slit open. It, in turn, affects the extent of beating and is responsible for some of the effects in the spectrochronogram. The instrument function is modeled as a combination of a Gaussian and a Lorentzian profile in the frequency domain (Voight profile), and the exact combination is achieved through trial and error. This profile is then convolved with the synthetic spectra to match what is seen on the camera. Hence, spectra with the slit closed are recorded to compare and get an estimate of both temperature and instrument function, which are then constants throughout the optimization.

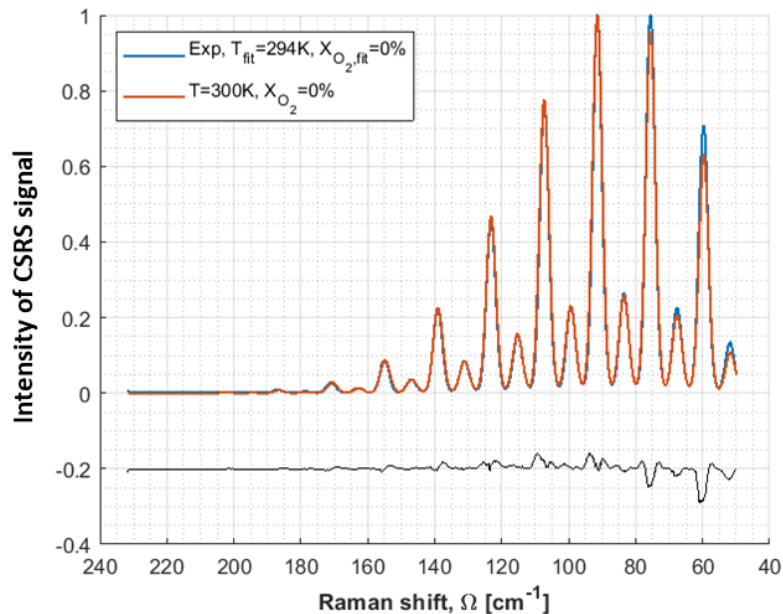


Figure 57: The best fit of nitrogen CSRS spectra at room temperature and an arbitrary delay. Experimental data recorded with the slit closed (blue), the synthetic best fit (closest fit at 300K, orange curve) and the residual between these two curves in black are shown. The fitting regime attributes a temperature of 294K and no Oxygen as expected. The synthetic curve is already compensated for the instrument function here.

Lastly, an algorithm needed to be chosen to run the optimization. Instead of using a gradient-based, a modified genetic algorithm was deemed apt for this work. The Genetic algorithm is optimal for a multi-objective problem and is generally very robust when searching for a global optimum. It starts with an initial population of design vectors – Arrival times and intensity per arrival. Then, the fitness of each individual is calculated and some of the fittest individuals (lowest residuals from the objectives) are retained. Their children form the next generation and, during the transfer to the next generation, mutations occur to these individuals randomly. This population then “evolves” until mutations do not improve the design vector beyond a certain tolerance. This process is shown in the flowchart (figure 58). The optimization process employed thus converged to a satisfactory result (in terms of improvement of the fitness over iterations) after 80,000 runs of the optimizing function, taking approximately four days in total.

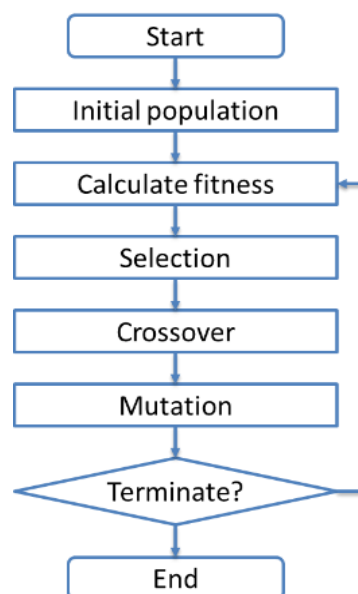


Figure 58: Flowchart of the steps in the Genetic algorithm from start to finish. The program ends when the termination condition of insufficient improvement in the genes is satisfied.

# 6

## Results and discussion

### 6.1 Synthetic probe representation

The synthetic representations of the probe pulse created with the optimized phase information now show a good reconstruction both in time and frequency (figure 60). This was expected, due to the nature of the objectives which minimize the residuals between the two curves. With this synthetic information, a spectrogram of the probe pulse can also be generated which details the nature of the output from the conjugation in the SHBC. This is shown in figure 59. In this figure, we can see the time-domain representation peaking twice near the maximum. It can also be seen that the sidebands and the tail form the majority of the intensity when this time-domain curve peaks twice, and the dip in between them corresponds to the main lobe of the probe pulse. This is a direct result of the two arrivals per frequency, which was a result of the non-resonant signal correlation measurements.

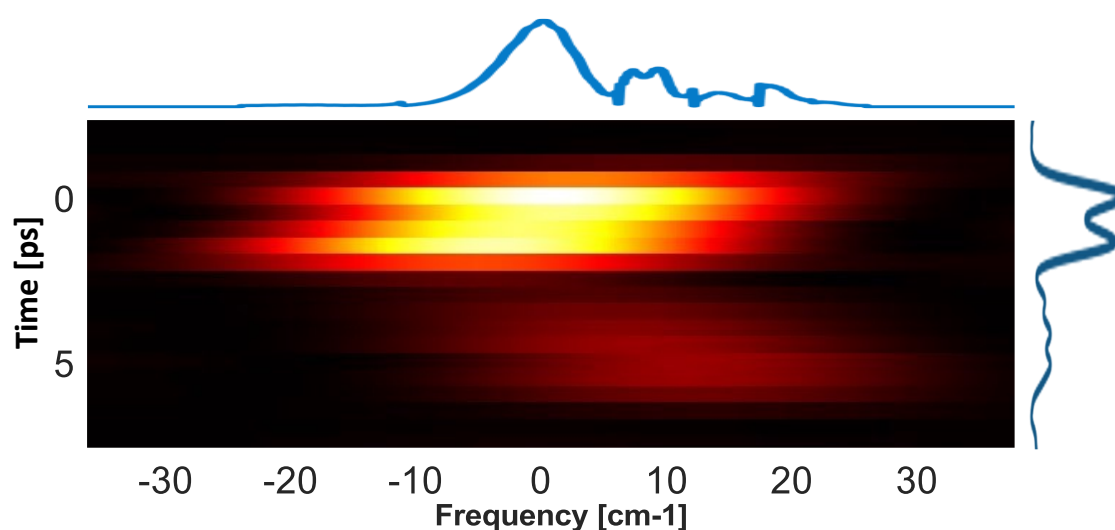


Figure 59: Spectrogram of the synthetic probe pulse (bottom right), along with the frequency-domain representation (top) and time-domain representation (bottom right). These time and frequency representations are the sum result in either direction, or the figures are placed in such a way to represent these sum results. A sum of all vertical lines in the spectrogram yields the time-domain response and the sum of all horizontal lines yields the frequency-domain response. For a color bar, refer to figure 31.

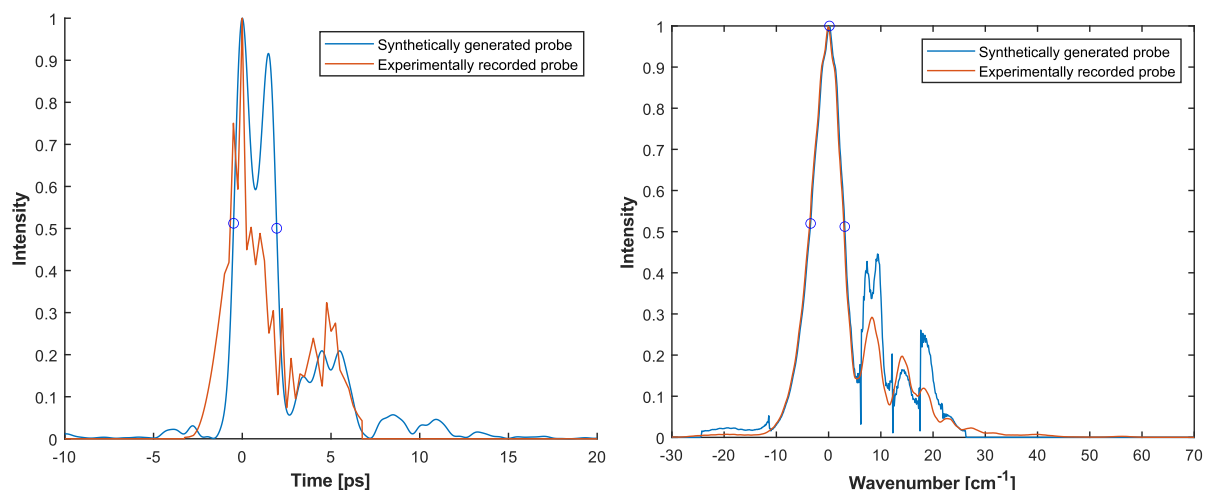


Figure 60: Comparison of the time (left) and frequency (right) domain representations of the pulse recorded experimentally, and a synthetic representation created by the interferogram model with phase information from the results of the optimization. Blue circles show the FWHM in each curve.

This spectrogram of the probe is the ideal result of the characterization, and this probe pulse can then be treated as a characterized constant, for use in generating CARS spectra.

## 6.2 Synthetic reconstruction of the nitrogen CSRS spectrochronogram

Figure 61 shows both the experimental nitrogen CSRS spectrochronogram at room temperature with the slit open and the synthetic reconstruction of the same using the probe pulse generated using the optimized phase information. The differences between the  $N_2$  CSRS spectra recorded using the filtered and direct probe were discussed in the section on the research objective. The synthetic reconstruction of this spectrochronogram produced with the direct output of the SHBC then captures the beating of the resonant Raman lines to a good extent: The spectrochronogram captures the periodicity coming from the nitrogen molecular response and also the varying degree of convolution of the different Raman lines (mostly even and odd lines) at specific delays. The reconstruction of this varying convolution is critical to retain the time- and frequency- resolution capabilities of hybrid fs/ps CARS, and can also be visualized in the spectrochronogram as the curvature in the lines that looks like an that leads to, and links, two repetitive periods in this spectrochronogram. Different delays are selected, and their spectra are plotted in figures 62-64, which show the differences between the experimental and synthetic spectra per delay.

The variation in the spectra across delays is produced from the different carrier frequencies in the probe scattering from different parts of the  $N_2$  molecular response, due to the chirp contained within this pulse. Hence, at a particular probe delay, when a larger band of frequencies in the probe act as the carrier frequencies, the lines in the spectrochronogram look more convolved and lead to a continuous shape (like figure 62). Then, as different carriers in the probe are time-gated by the response, the Raman lines shift in frequency, also proportional to the shift in the carrier from the probe (like figure 64). This eventually also reaches a point where a small band of frequencies in the probe act as carriers and we see a reasonable separation in different Raman lines, resembling the experiments with the direct probe (like figure 63). With this beating across probe delays captured to a very good extent, this model for the probe can be used to fit temperatures.

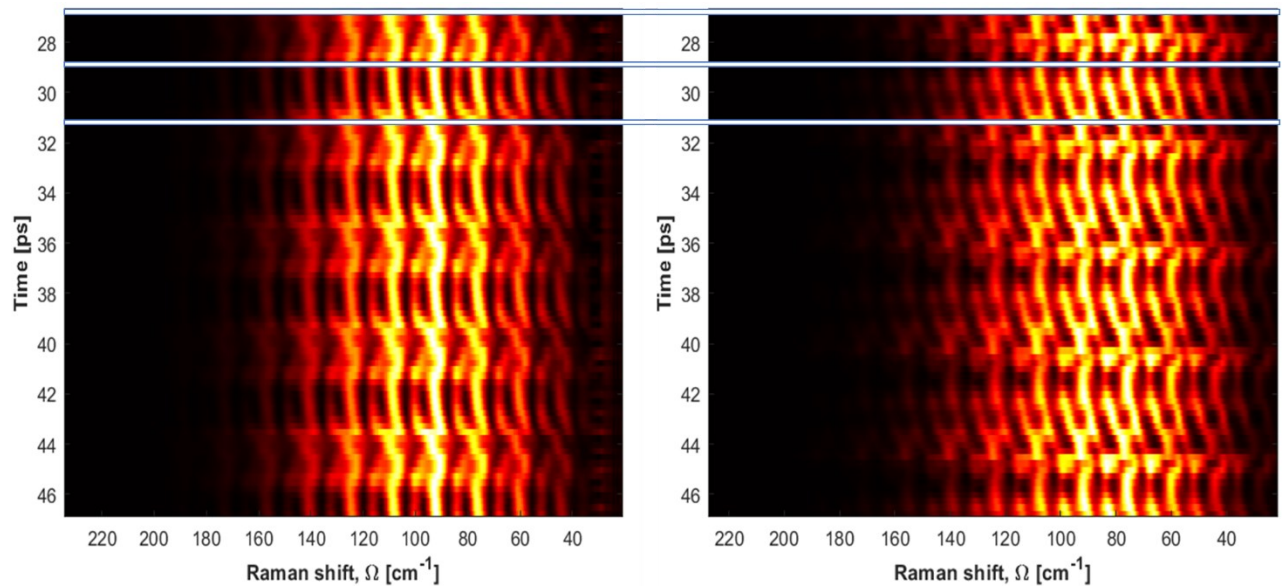


Figure 61: Comparison of nitrogen CSRS spectrochronograms at room temperature. Experimental, on the left, and synthetic reconstruction using optimized phase information on the right. The three marked horizontal lines across both spectrochronograms detail the delays for which spectra will be shown in the subsequent figures. For a color bar, refer to figure 31.

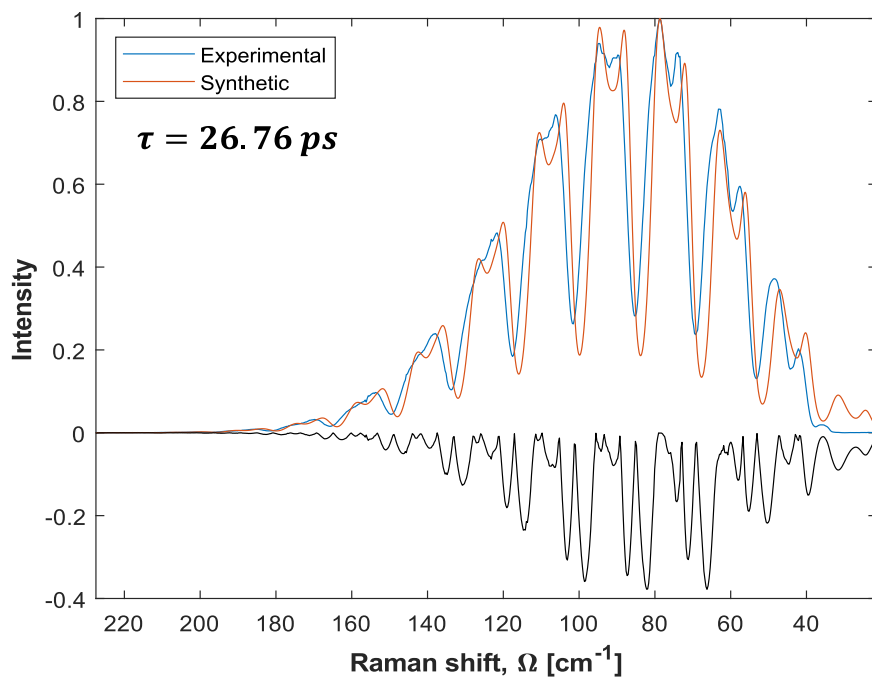


Figure 62: Comparison of nitrogen CSRS spectra at room temperature at a probe delay of 26.76 ps. Synthetically generated spectra using the phase-optimized probe pulse (orange curve), and experimentally acquired spectra for the same delay (blue curve). The black curve computes a residual (absolute difference) between the two.

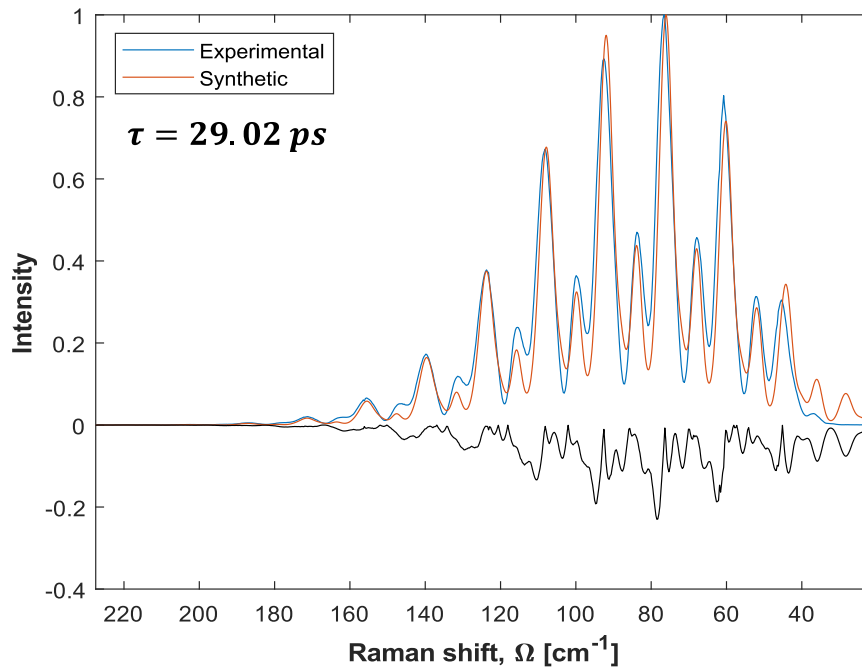


Figure 63: Comparison of nitrogen CSRS spectra at room temperature at a probe delay of 29.02 ps. Synthetically generated spectra using the phase-optimized probe pulse (orange curve), and experimentally acquired spectra for the same delay (blue curve). The black curve computes a residual (absolute difference) between the two.

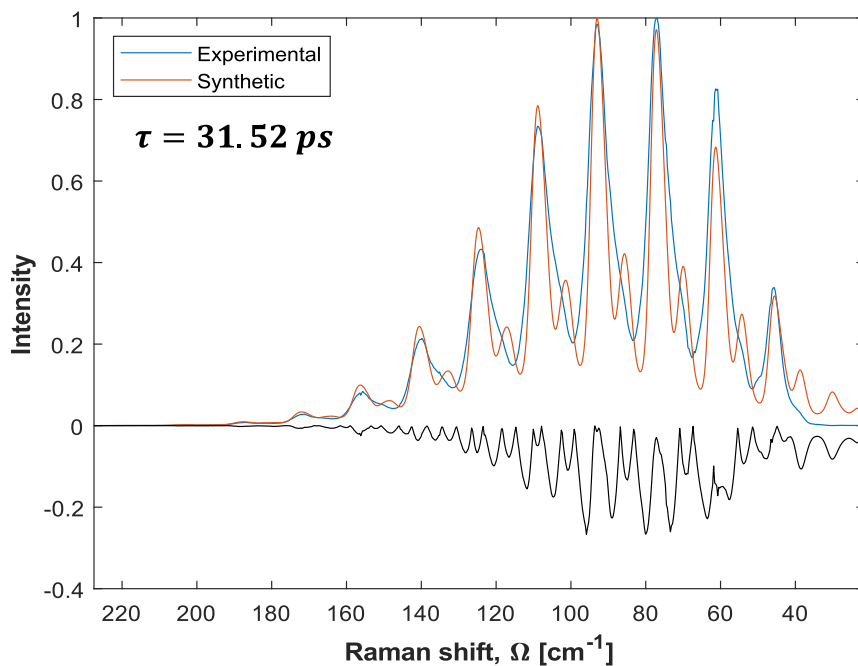


Figure 64: Comparison of nitrogen CSRS spectra at room temperature at a probe delay of 31.52 ps. Synthetically generated spectra using the phase-optimized probe pulse (orange curve), and experimentally acquired spectra for the same delay (blue curve). The black curve computes a residual (absolute difference) between the two.

From the figures above, it can be very qualitatively observed that the synthetic probe model is capable of reconstructing the spectra of nitrogen across delays at room temperature. This nitrogen spectrochronogram was the benchmark for validating the characterization, models, and optimization. The extent of the reconstruction is judged by how well the model can retrieve temperature as compared to a similar case using the filtered probe at room temperature. Such a comparison is shown in figure 65. Here, the fitted temperatures for the spectrum generated using the direct probe pulse are  $\sim 291.25$  K and is  $\sim 291.00$  K for the spectra generated by the

filtered probe pulse. Both these spectra shown are recorded at the same delay. The difference is minimal and hence, the temperatures retrieved are in very good agreement. This, however, is not the case for all the probe delays, and temperatures from some probe delays are retrieved better than others. This is due to inaccuracies in the characterization probe pulse which are spread unequally across delays. Nevertheless, spectra generated from most probe delays retrieve temperatures that are in good agreement with the ones from the filtered probe, and the synthetic probe model can then be used to fit temperatures using nitrogen spectra.

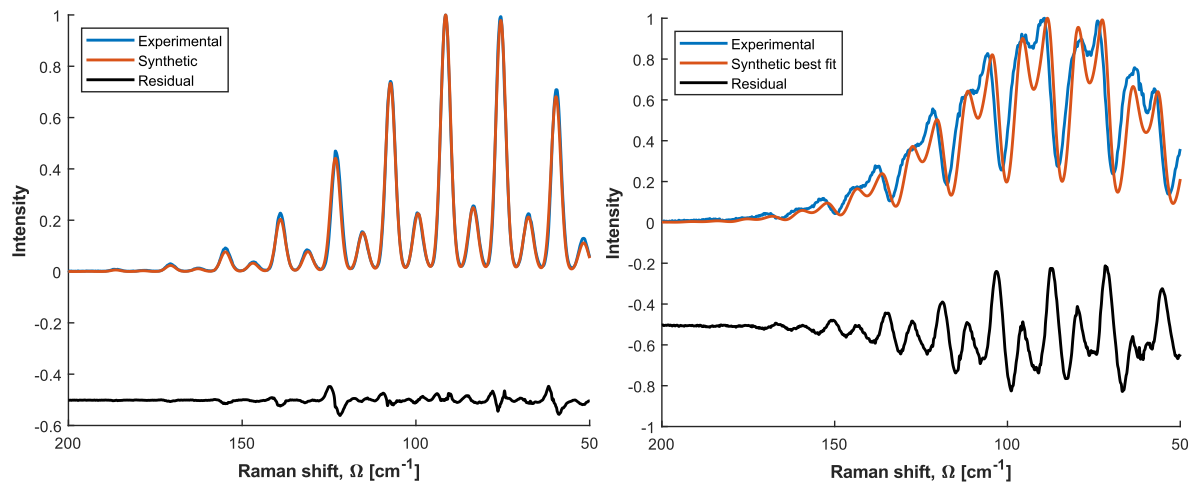


Figure 65: Best fit for nitrogen CSRS spectra at room temperature at a probe delay of  $\sim 43.53$  ps, performed for both the direct (right) and filtered (left) probes. Synthetic best fit using the appropriate probe pulse (orange curve), and experimentally acquired spectra (blue curve). The black curve computes a residual between the two. The fitted temperature for the filtered probe pulse (left) is  $\sim 291.00$  K, and for the direct probe pulse (right),  $\sim 291.25$  K. This figure replicates the initial attempt to fit these spectra using old models in figure 24.

### 6.3 Synthetic reconstruction of the Air CSRS spectrochronogram

With the synthetic model for the probe pulse validated with the nitrogen CSRS spectrochronogram, the validation should also extend to other molecular responses (other environments in the probe volume). This is because the probe pulse is now a characterized constant. To model the CARS/CSRS signal, the time-domain molecular response is convolved with the time-domain probe pulse profile. The variation in temperatures and species concentrations comes only from the molecular response and hence if the probe pulse can simulate spectra for a given molecular response, it should be able to capture the time- and frequency- domain characteristics of any other response as well.

To show this, the case of air at room temperature is presented. First, in figure 66 the air CSRS spectrochronogram at room temperature recorded with the filtered probe is shown, along with the synthetic reconstruction of the same (using a model for the filtered probe). Here, we can see that the resonant spectra for air beat across probe delays even with the filtered probe. This is due to the close proximity of the Raman lines of Oxygen and nitrogen (Air is 79% nitrogen and 21% Oxygen), and the time-dependent variation of both resonant spectra with different revival periods (Oxygen revival  $\sim 6.2$  ps and nitrogen revival  $\sim 8.4$  ps). And, the probe records the beating existing within the molecular response due to the lack of extremely high spectral resolution between these Raman lines.

When the same experiment is repeated using the direct probe from the SHBC, the chirp contained within this probe adds to the beating coming directly from the molecular response of air. This is evidenced in the spectrochronogram for air at room temperature recorded with the direct probe, as shown in figure 67, and its synthetic reconstruction is also shown.

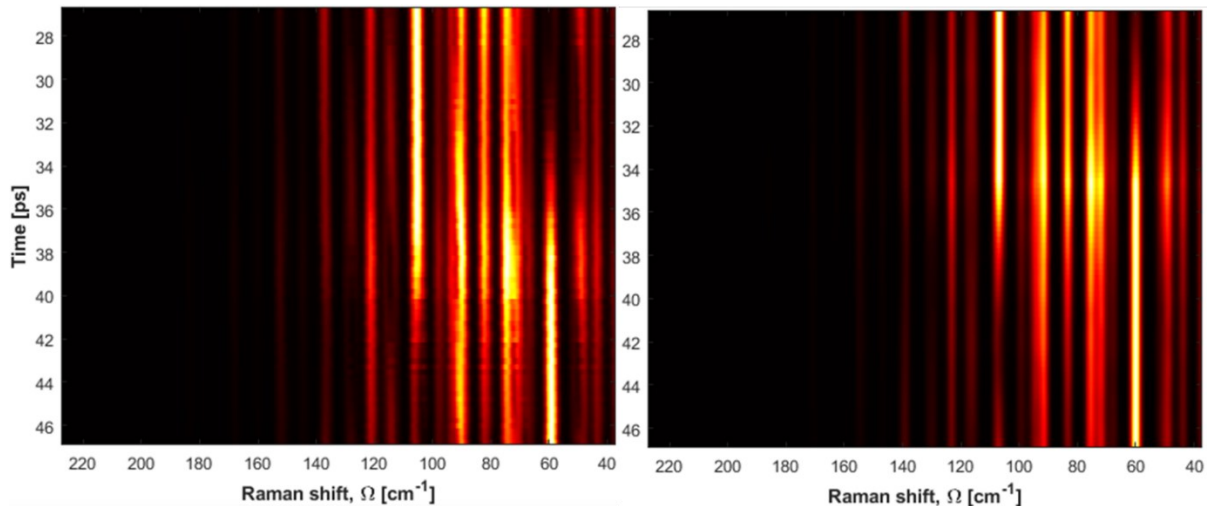


Figure 66: Comparison of Air CSRS spectrochronograms at room temperature, generated with the slit closed. Experimental, on the left, and synthetic reconstruction using a model of the filtered probe pulse on the right. For a color bar, refer to figure 31.

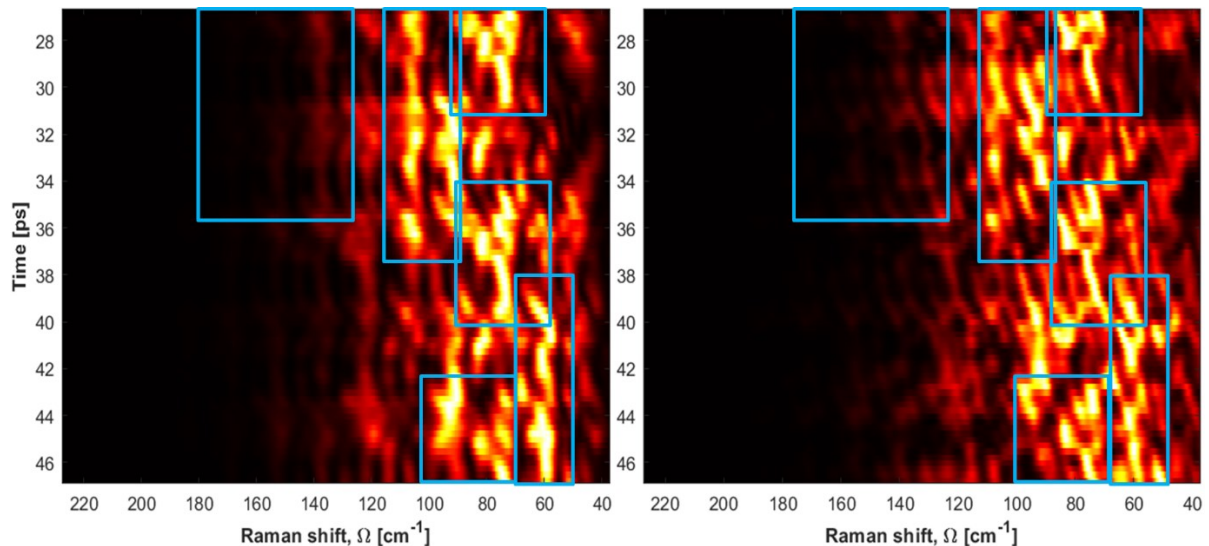


Figure 67: Comparison of Air CSRS spectrochronograms at room temperature. Experimental, on the left, and synthetic reconstruction using a probe pulse with optimized phase information on the right. The blue boxes show different spectrochronographic regions that evidence a good reconstruction. For a color bar, refer to figure 31.

The spectrochronogram itself is difficult to reduce to clear spectral features, but it still contains information on Boltzmann distributions, for example. Some spectrochronographic features that are similar between the acquisition and the reconstruction are marked in the comparison shown above. The box on the top left of these figures picks out a region containing the spectrochronographic properties of nitrogen CSRS, similar to those in figure 61.

This spectrochronogram is not retrieved as well as the one for nitrogen discussed above, but it is still a good approximation. There are significant limits to the accuracy of modeling the air spectrochronogram that are mainly due to the severe nature of the beating of resonant spectra across probe delays. This imposes limits on the accuracy of the fit between the experimental recording and synthetic spectra. However, the time-domain probing of this information is bound to be more sensitive to temperature changes if it can be reconstructed perfectly due to the same (severe, but characteristic) beating.

## 6.4 Flame thermometry

This section is about the use of this phase-characterized probe pulse in combustion applications. A nitrogen-diluted laminar  $H_2$ /air diffusion flame (50%  $H_2$  – 50%  $N_2$  by volume), provided on a Bunsen burner of 19 mm diameter, is used as the test case and the results are validated against experiments recorded with the filtered probe, which are already validated. Flow rates for  $H_2$  and  $N_2$  were set using analog flow controllers to be 1 Liter per minute each. With this information, one can define Reynold's number for this flow as:

$$Re_{\text{burner exit}} = \frac{Q * D_B}{\nu * A_B} = \sim 105 \quad \text{Eq.14}$$

With  $Q = 3.33 * 10^{-5} \frac{m^3}{sec}$ ;  $A_B = \pi * \left(\frac{D_B^2}{4}\right)$ ;  $D_B = 1.9 * 10^{-4} m$ ; and  $\nu = 2.12 * 10^{-5} Pa - s$ . Where,  $Q$  is the volumetric flow rate,  $A_B$  and  $D_B$  are the area and diameter of the burner respectively, and  $\nu$  is the kinematic viscosity of the hydrogen-nitrogen mix. A Reynold's number of 105 is considered low, as compared to 2000 near the transition to turbulent flow for flow in a pipe. Hence, this flow can be considered laminar which is important for the following discussion.

Particularly, nitrogen is the molecule of interest here, due to its common use as a molecule to gain spectroscopic information. At the center of a hydrogen diffusion flame, a small amount of nitrogen exists due to diffusion across the flame front and through the bulk of the flame. 50% nitrogen is seeded to supplement this. Oxygen, however, is completely consumed already near the flame front. The nitrogen was seeded along with the hydrogen fuel to increase the signal from nitrogen at the camera and to reduce the temperature of the flame to get it within measurable limits (due to the number of scattering molecules decreasing with temperature).

The objective here was to show the capability of the phase-characterized probe pulse to retrieve time- and frequency-resolved information from different parts of this flame. Hence, CSRS spectra were recorded at different delays (now with a much larger time step of  $\sim 1$  ps as generating a spectrochronogram is not the objective) ranging from  $\sim 41.77$  ps to  $\sim 46.77$  ps, with a total of 6 delays and 1000 frames recorded for each delay (with  $\sim 1$  ms exposure time with 1 kHz repetition rates). This delay scan was repeated for 23 positions of the flame, by moving the burner across the probe volume to cover half of the axisymmetric flame, and also some hotter air after the flame front. The flame was moved in steps of 0.5 mm transversely to the interaction length, to attain different temperatures and flame progress. Figure 68 shows this flame progress with the temperature across the flame, alongside the flame itself.

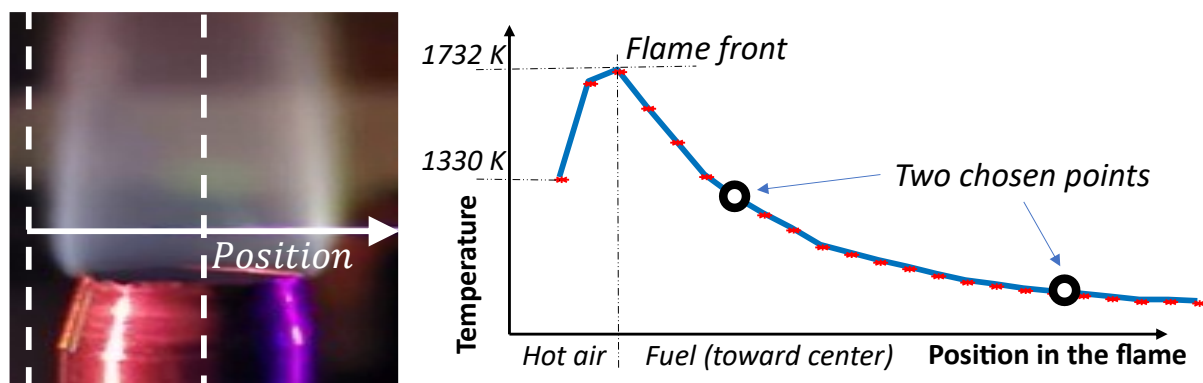


Figure 68: (Left) The  $H_2/N_2$  flame, with the positioning of the probe volume. The dashed lines represent the length measured, and the arrow shows the x-axis direction for the figure on the right. (Right) The flame temperature mapped across this flame at an arbitrary height (measured using the filtered probe pulse), denoting regions in the flame and the measurement points (red asterisks).

### 6.4.1 Center of the burner

Measurements conducted at the center of the burner with the slit closed suggest a temperature around  $\sim 877$  K (a temperature fit for one frame of this data is shown in figure 69 along with the shot-to-shot fluctuation of this temperature), with a variation of fitted temperature between  $\sim 860$ - $890$  K. This position was chosen due to the lack of parameters other than temperature affecting the spectra (such as  $O_2$  concentration), removing complexity from the fitting regime, and due to the relative stability of the flame at this position.

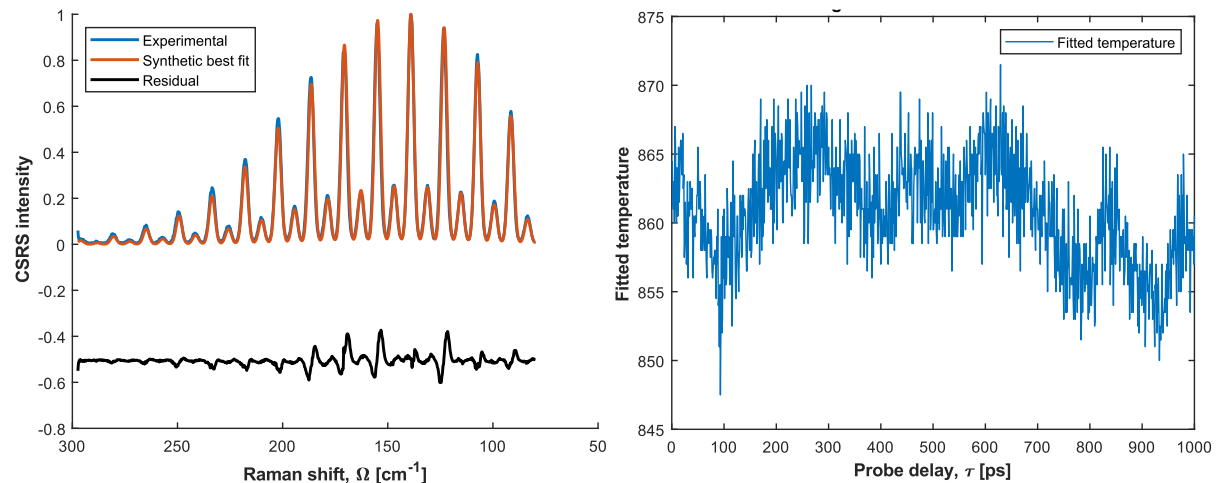


Figure 69: (Left) Temperature fit at the center of a hydrogen diffusion flame seeded with nitrogen at a particular arbitrary delay:  $T_{fit} = \sim 860$  K (mean temperature). The resonant lines here all belong to nitrogen (higher Raman lines are populated due to the higher temperature, as compared to the spectra previously shown at room temperature), and are produced with a probe pulse generated with the slit closed (experimental – blue curve). The orange curve is a synthetic model at the same conditions and the black curve is the residual between the two. (Right) Shot-to-shot fluctuation of this fitted temperature. Observed standard deviation:  $\sigma_{T_{fit}} = 3.22$ . The first frame in this plot was used to make the blue curve on the figure on the left.

The same experiment was repeated with the slit open, at the same position in the flame to get an idea of the accuracy of thermometry using the direct probe. The data recorded shows a variance across multiple delays, as expected, due to the similar nature of the beating contained in the nitrogen spectrochronograms shown before. The resonant nitrogen spectra beat across probe delay with a characteristic that depends on the temperature, phase information on the probe, and experimental apparatus because of the instrument function discussed before with the section on the optimization.

Two spectra measured using the direct probe pulse, at probe delays  $\sim 41.78$  ps and  $\sim 42.78$  ps are shown in figures 70 and 71 along with their shot-to-shot fitted temperatures. It is important to note that the spectrum in figure 71 resembles the spectrum generated using the filtered probe (figure 69) much more than the one in figure 70. This is due to the particular delay (42.78 ps), at which a small bandwidth of frequencies in the probe pulse is time-gated by the molecular response. Naturally, this delay would also fit closer temperatures to those predicted by the filtered probe pulse, and this can be seen, as  $T_{fit} = \sim 852$  K for this delay of the direct probe pulse as compared to  $T_{fit} = \sim 860$  K for the filtered probe pulse.

Whereas, the spectrum displayed in figure 70 (at a delay of 41.78 ps) shows a  $T_{fit} = \sim 819$  K. The temperature fits discussed are all mean temperatures across the 1000 frames captured, which present the inaccuracies here as  $\sim 1\%$  and  $\sim 4.7\%$  for the two delays (42.78 and 41.78). This variance in accuracy across probe delay is due to some delays being captured better

than others by the probe pulse model, which was also mentioned with the temperature fits at room temperature.

The spectra and their variation across delays are reconstructed to a good extent even at the center of this flame, albeit to a varying extent for different delays. The accuracies are good for each spectrum and are excellent for the particular delay mentioned above.

The resulting single-shot precision (standard deviation of fitted temperatures) for both the delays ( $\sigma_{T_{fit}} = 3.21$  for the delay of 41.78 ps and  $\sigma_{T_{fit}} = 3.40$  for the delay of 42.78 ps) show no significant difference from the one observed with the filtered probe ( $\sigma_{T_{fit}} = 3.22$ ), indicating that when the spectra do not fluctuate over single-shot and contain a sufficient signal-to-noise ratio, the precision using the direct probe is comparable to that of the filtered probe.

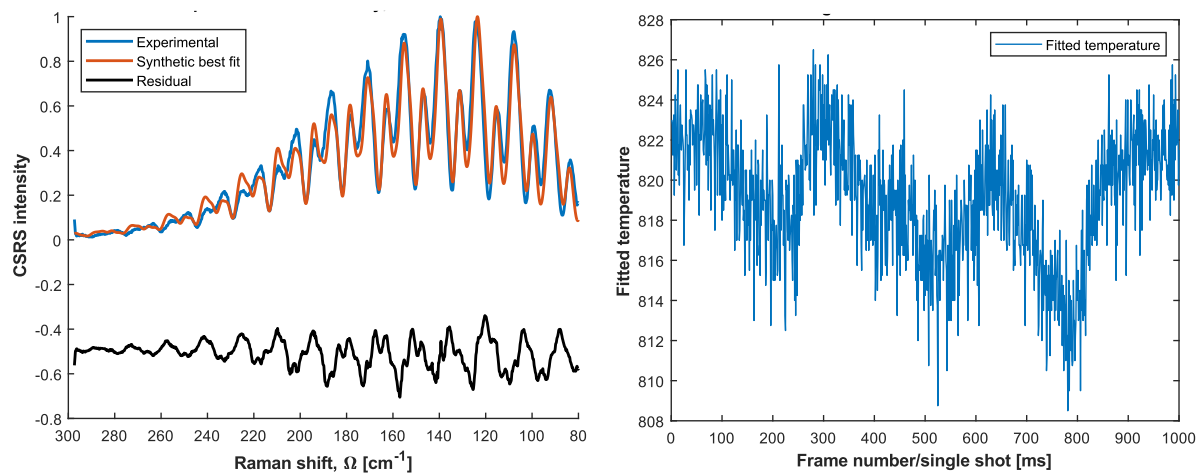


Figure 70: (Left) Temperature fit at the center of a hydrogen diffusion flame seeded with nitrogen at a probe delay of 41.78 ps:  $T_{fit} = \sim 819$  K (mean temperature). The resonant lines here all belong to nitrogen and are produced with a probe pulse generated with the slit open (experimental – blue curve). The orange curve is a synthetic model at the same conditions and the black curve is the residual between the two. (Right) Shot-to-shot fluctuation of this fitted temperature. Observed standard deviation:  $\sigma_{T_{fit}} = \sim 3.21$ . The first frame in this plot was used to make the blue curve on the figure on the left.

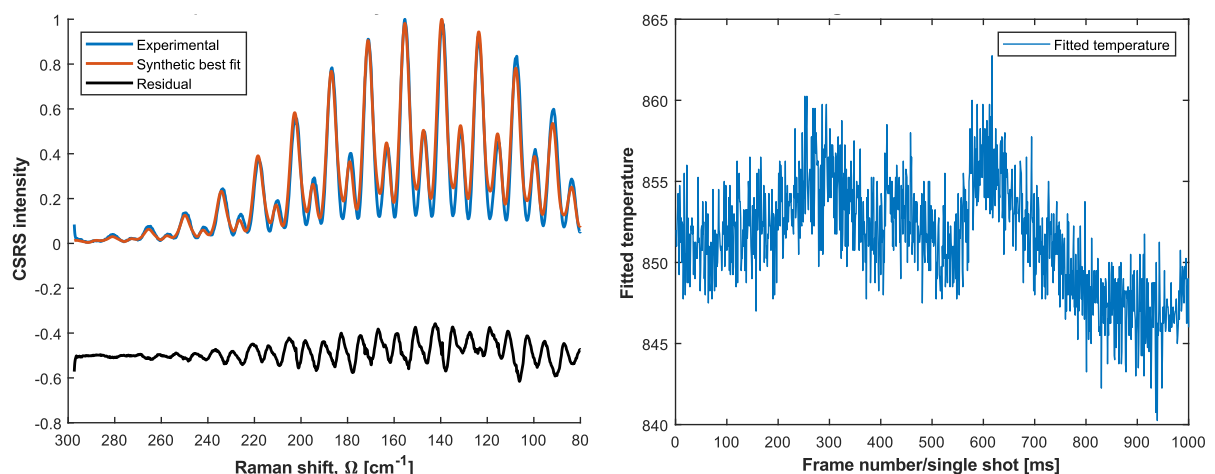


Figure 71: (Left) Temperature fit at the center of a hydrogen diffusion flame seeded with nitrogen at a probe delay of 42.78 ps:  $T_{fit} = \sim 852$  K (mean temperature). The resonant lines here all belong to nitrogen and are produced with a probe pulse generated with the slit open (experimental – blue curve). The orange curve is a synthetic model at the same conditions and the black curve is the residual between the two. (Right) Shot-to-shot fluctuation of this fitted temperature. Observed standard deviation:  $\sigma_{T_{fit}} = \sim 3.40$ . The first frame in this plot was used to make the blue curve on the figure on the left.

## 6.4.2 Near the flame front

The second point of validation where a higher temperature is expected, located at 3 mm from the flame front is discussed. This measurement point was chosen because of its higher temperature, further elevating the capability of the characterized probe pulse, but also as this is the closest point to the flame front without starting to include the resonant spectra of Oxygen in addition to those of nitrogen.

While this phase-characterized probe pulse is quite capable of resolving Oxygen spectra (as proven with the room temperature air CSRS spectrochronograms), there is an additional problem when trying to measure concentrations with this probe pulse: The probe delay set by the mechanical delay stage in this setup is not perfect. It was found while working with the data that there was a near-constant offset in the probe delays that needed to be fitted to each spectrum when measured with the slit open (along with temperature, the probe delay can also be a fitting parameter when one is unsure of the exact delay that the stage offers). Moreover, this offset can only be pinpointed to a confidence interval, and cannot be represented as a fixed value, mainly due to minute errors with the phase-characterization or the experimental spectra themselves, leading to a variation of the fitted probe delay.

Hence, when attempting to fit these spectra with Oxygen involved, adding beating to the pre-existing beating from the chirp in the probe pulse, with the current fitting regime, the variation of frequency information with time can either be attributed to the presence of Oxygen or the lack of accuracy on the probe delay. This is a major limitation as it prevents the probing of the highest temperatures, such as at the flame front. However, with better characterization using the information learned in this project, it should be possible to not only characterize the probe pulse better but also to calibrate the offset in probe delay and measure species content.

The figures below show a comparison of temperature fits at this position of the flame using both the direct and the filtered probe pulses at arbitrary delays. At this point in the flame, there are fluctuations with time which cause a difference in temperatures between measurements. Hence, in this plot, the closest recorded temperature fits from the two different probe regimes are shown:  $T_{fit} = \sim 1200 \text{ K}$ ,  $\tau = 43.78 \text{ ps}$  for the case with the direct probe pulse, and  $T_{fit} = \sim 1143 \text{ K}$  for the case with the filtered probe pulse.

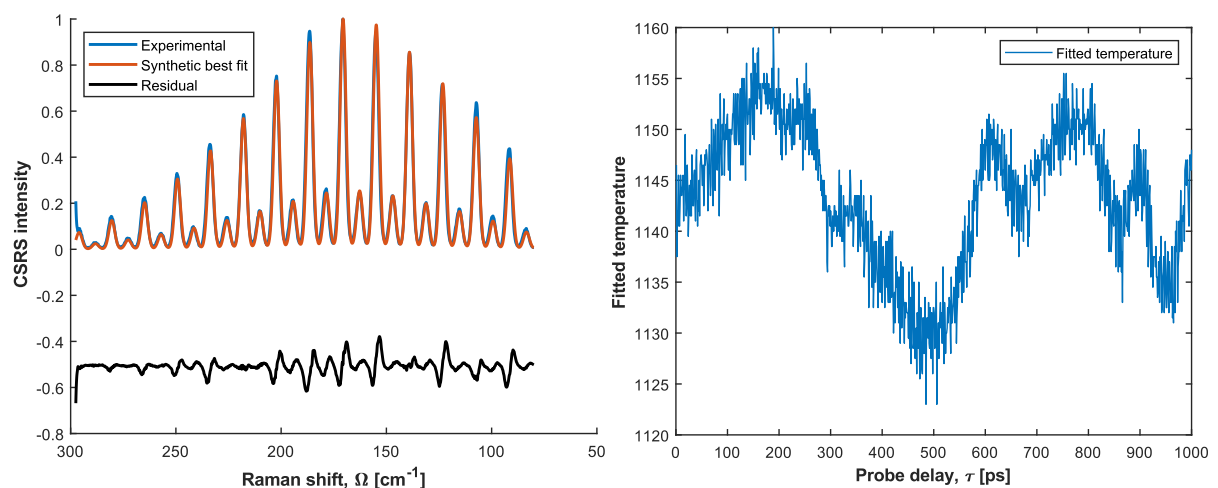


Figure 72: (Left) Temperature fit 3mm away from the flame front of a hydrogen diffusion flame seeded with nitrogen:  $T_{fit} = \sim 1143 \text{ K}$  (mean temperature). The resonant lines here all belong to nitrogen and are produced with a probe pulse generated with the slit closed (experimental – blue curve). The orange curve is a synthetic model at the same conditions and the black curve is the residual between the two. (Right) Shot-to-shot fluctuation of this fitted temperature. Observed standard deviation:  $\sigma_{T_{fit}} = \sim 7.08$ . The first frame in this plot was used to make the blue curve on the figure on the left.

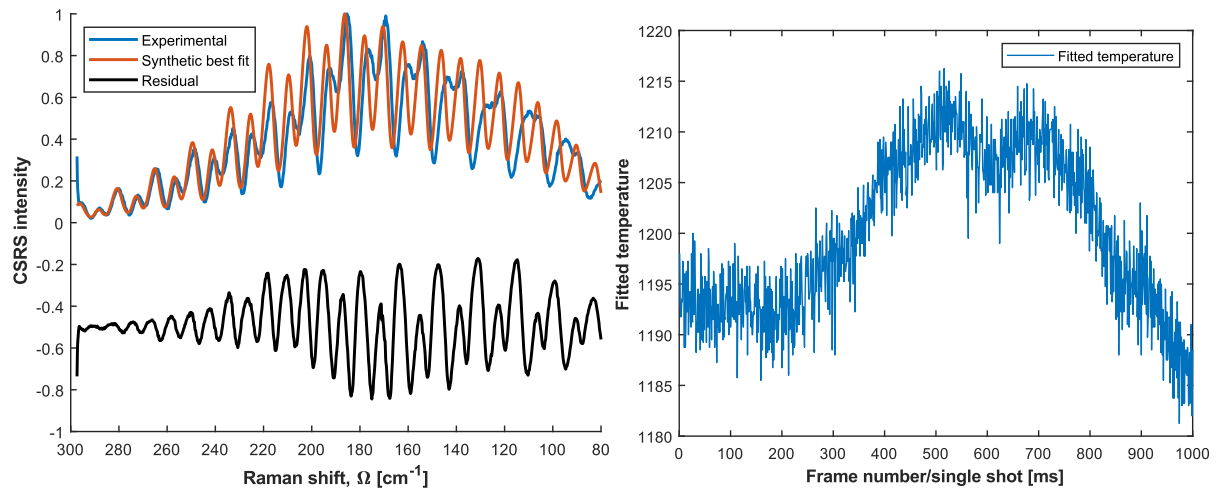


Figure 73: (Left) Temperature fit 3mm away from the flame front of a hydrogen diffusion flame seeded with nitrogen at a probe delay of 43.78 ps:  $T_{fit} = \sim 1200$  K (mean temperature). The resonant lines here all belong to nitrogen and are produced with a probe pulse generated with the slit open (experimental – blue curve). The orange curve is a synthetic model at the same conditions and the black curve is the residual between the two. (Right) Shot-to-shot fluctuation of this fitted temperature. Observed standard deviation:  $\sigma_{T_{fit}} = \sim 7.90$ . The first frame in this plot was used to make the blue curve on the figure on the left.

The higher residual in the case of the direct probe pulse shows that the phase-characterization is not perfect, but more than sufficient to capture temperature changes across this flame. This maintains the ability of the phase-characterized probe pulse to measure temperatures accurately as those with the filtered probe pulse, even at a higher temperature such as these ( $\sim 1150$  K).

Additionally, due to the time-variance of the spectra generated in the case of the phase-characterized probe pulse, this regime could be more sensitive to temperatures. However, to compute and use the spectra at different delays, these spectra must be recorded sequentially (using the current setup), which introduces fluctuations in the flame to spectra at different delays. Nevertheless, figures 72 and 73 show also the shot-to-shot fluctuations for the two cases, which show the extent of the fluctuations in the flame captured by each case. The standard deviation values presented in respective figure captions do not represent precision anymore due to the added fluctuation in this position in the flame but only act as a representation of the spread of the data. Their similarity ( $\sigma_{T_{fit}} = \sim 7.90$  for the direct probe pulse case and  $\sigma_{T_{fit}} = \sim 7.08$  for the filtered probe pulse case) hints at the capture of the spread of temperatures at this point in the flame due to these fluctuations.

# Conclusions

This project researched the CARS spectra generated using the higher power direct probe pulse output of the SHBC. The signals recorded using higher probe pulse powers implied a higher signal-to-noise ratio, which would increase the precision of CARS at high temperatures.

It was observed that the nitrogen CARS spectra recorded with this pulse show a considerable variation in the spectra across probe delays due to the chirp contained within the probe pulse, along with its shorter duration.

Hence, this probe pulse was characterized by discretizing its frequency domain representation using the 4F-filter and measuring the time signatures of each resulting segment. The frequency information was read by generating nitrogen CARS signal from each of these segments, which showed a frequency shift dependent on the carrier frequency of the probe pulse segment used to generate it.

The time signature measurement was done by using the femtosecond pump/Stokes pulse to time gate the picosecond probe pulse and recording the non-resonant signal generated from this superposition, to use as a method of correlation. Precisely, the intensity of the non-resonant signal generated at different time gates correlates linearly, directly, to the intensity of the probe pulse used to generate it.

The time-arrival information of the different probe pulse segments indicated that the sidebands appear twice in the probe pulse, once on each side of its main lobe, due to the nature of the conjugation in the SHBC, thereby increasing the complexity of the chirp contained in the pulse.

However, the reconstruction of the probe pulse, along with simulations of the nitrogen spectrochronogram did not recount the experimentally observed results of the same. This was proposed to be due to limitations in the experimental characterization of the probe pulse, namely, the unavoidable fluctuations of the non-resonant signal from an open gas using two-beam fs/ps CARS, the duration of the pump/Stokes pulse used for the experiment, and, any possible errors in the measurements of the nitrogen CARS spectra themselves.

The acquired phase information was subsequently tuned using a tailored genetic algorithm that moderated the interference pattern in the probe pulse by controlling time-arrival information and minimizing residuals formed from the probe pulse and CARS signal comparisons.

The resulting synthetic model for the probe pulse recounted the experimentally observed representations in time and frequency domains to a good extent and was capable of reconstructing the experimental CSRS spectrochronograms of pure nitrogen and, to a slightly lesser extent, air, at room temperature.

Hence, the direct probe pulse from the output of the SHBC can be used for CARS measurements when it is characterized and this characterization can be performed using CARS signals themselves. This probe pulse is intended to be used as a characterized constant, alongside models for the molecular response, to simulate the variation of spectra with probe delay in various environments, to yield temperature measurements.

These models were finally used to test the phase-characterized probe in a laminar hydrogen diffusion flame, seeded with 50% nitrogen. At the center of this flame, the mean temperatures predicted by the filtered probe and the direct probe differ by ~1% and 4.7% for

different delays. The precision, however, is not so critically impacted by the inaccuracies in the characterization and is similar to those observed with the filtered probe.

The difference in accuracy across probe delays is due to errors in the characterization of the direct probe pulse, affecting some delays more than others. This becomes more critical near the flame front, where the limitation of fitting both the probe delay and concentrations becomes a challenge.

It is expected that when the characterization is perfected, these challenges can be overcome, and a direct increase in signal-to-noise ratio would lead to maximum precision, along with the capability of time-domain probing of spectral data.

In the future, these characterizations would need to be performed using a constant change in the slit at the Fourier plane (or the use of thicker material), in a gas cell/solid material within a short time to not incur variations due to slow changes in the setup.

# Appendix

This chapter contains further remarks and observations that may not contribute to the flow of the chapters before but contains information discovered during the thesis which is critical to the evolution of the work discussed above and is meant to be read as an appendix.

## Probe pulse fluctuations

Before the phase information of this probe pulse can be characterized and used to predict temperatures, its variation over shots/pulses was scrutinized. If there was a significant variation between the pulses, then the added complexity would need to be evaluated and checked whether it is possible to characterize the phase information for this pulse, as a spread over pulses. The variation in these pulses is shown below.

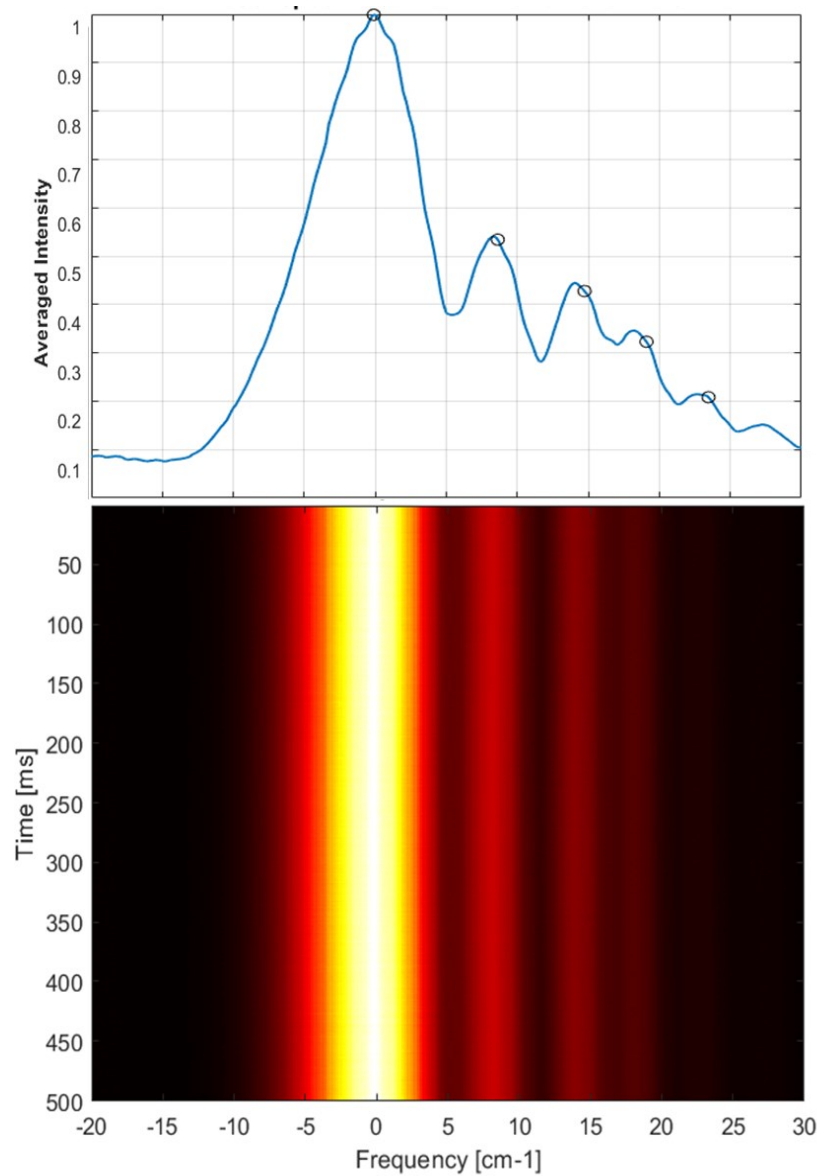


Figure 74: Spectral content in the laser pulses, detailed over multiple pulses (temporal resolution is the same as pulses repetition rate here, 1kHz). The first image (from the top) shows the already familiar spectral information of the probe output from the SHBC, averaged over 1000 pulses. The image below is a spectral content representation of each pulse (with time on the y – axis).

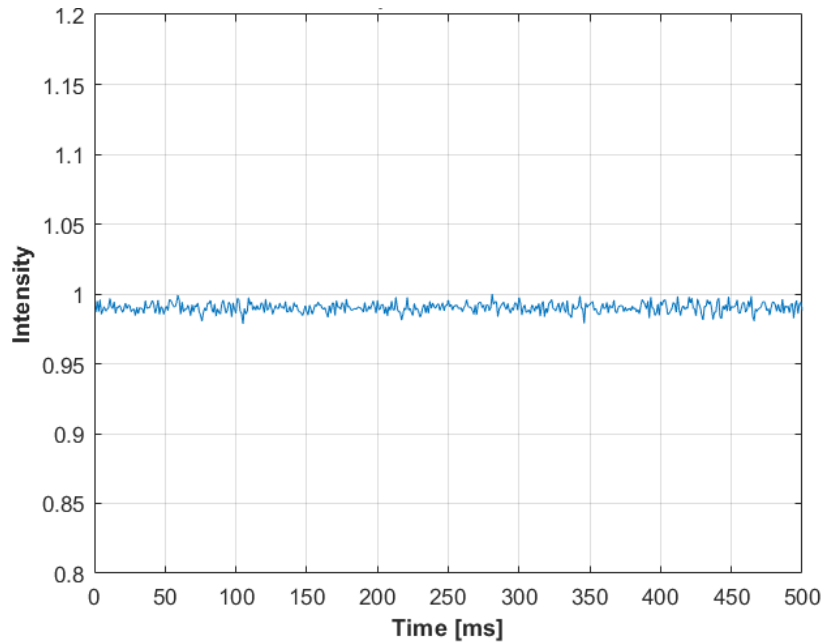


Figure 75: Intensity of the laser pulse-to-pulse. Each data point is a spectrally binned value from the spectrogram in figure 75.

It can be seen from the figures above that the laser pulses do not vary significantly with respect to each other in both spectrally averaged intensity and relative spectral intensity and keep to the manufacturer’s claim of pulse characteristics (which has a low variance over pulses). This is, importantly, also the case with the pulse output from the SHBC, which confirms that the imperfections in the gratings leading to the photons at uncharacteristic frequencies are constant (see the section on the SHBC within the experimental setup).

These imperfections are, as mentioned before, unavoidable, and depend heavily on the settings in the SHBC. Precisely, the delay stage in the SHBC that shifts, in time, one conjugately chirped pulse with respect to the other and the phase matching conditions at the BBO crystal where the sum–frequency generation occurs. For multiple reasons relating to different requirements for different projects at the lab, these settings need to be changed. It is important to note that for each different setting in the SHBC for the delay stage and the BBO crystal, a new probe with photons at different “extra” frequencies would be produced and this would then need to be characterized as well. The shift in the probe spectrum is shown below. The treatment of different probe spectra and the characterization of different sets of phase information is beyond the scope of this report, which is centered on developing a new and efficient way to characterize this phase information. All the experiments done in this work were performed at “setting – 1” shown in figure 77.

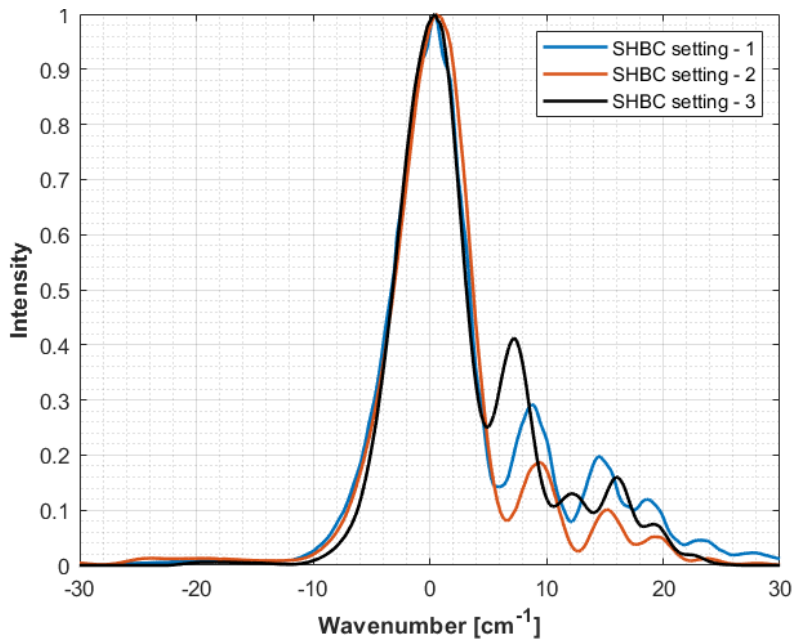


Figure 76: Shift in the spectrum of the probe with changes in the position of the delay stage in the SHBC and/or the phase matching at the BBO crystal.

## Spectral coincidence of the probe and CARS signal

Since the probe is sufficiently more intense than the CARS signal, it will first saturate and then damage the sCMOS camera if not sufficiently suppressed in intensity (when observing a regular intensity CARS signal). Moreover, slightly more broadband or asymmetric pulses (as compared to the original narrow probe) will have frequency content that will superimpose onto the CARS signal, which may have scattered from other frequencies in the probe (Figure 78). Hence it is imperative that the probe is not received by the camera and is dumped or suppressed somehow beforehand.

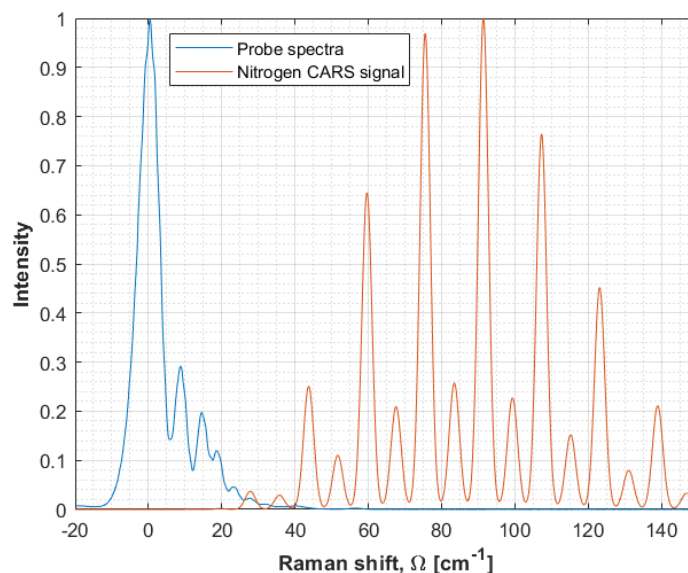


Figure 77: Spectral coincidence of the higher frequency photons from the probe and the CARS signal from nitrogen as would be seen on the camera. This nitrogen signal is generated with the slit in the 4F – plane closed. Both signals have been normalized with respect to each other to show the spectral coincidence of the probe at low Raman shifts (~20 – 40). The nitrogen signal in orange is orders of magnitude weaker than the probe and the probe was attenuated considerably to image it on the camera.

A very useful method to suppress the non-resonant signal using the controlled direction of polarization for the input laser beams (pump/Stokes and probe) was proposed in [50]. The difference in polarization between the resonant and non-resonant occurs due to extra contribution into polarization from electronic resonances in the case of non-resonant four-wave mixing. As mentioned before, the non-resonant signal can be avoided by delaying the probe with respect to the pump/Stokes beam. Hence, this method can be used to tune the polarization of the CARS signal to suppress the probe after generating the CARS signal, instead of the non-resonant signal. Since this proved to be insufficient, an additional suppression method using angle – tuning of a thin film acting as a bandpass filter was included. This filtered out the frequencies of the probe and some of the CARS signal, allowing the higher frequency components of the CARS signal to pass through the spectrometer.

However, the probe spectrum falls directly over most of the nitrogen CARS spectrum at room temperature, and it was deemed unrewarding to attenuate a large part of this spectrum. Hence, the nitrogen, Air, and flame data that were displayed in this report were recorded on the CSRS side of the coherent Raman spectrum (which falls on the left of the probe in the spectral plot, as shown in figure 79). This frequency range does not face interference as there is significantly lower intensity in the probe spectra at frequencies much lower than the center frequency in the probe. Hence, this can be separated using a combination of polarization separation and thin-film angle–tuning.

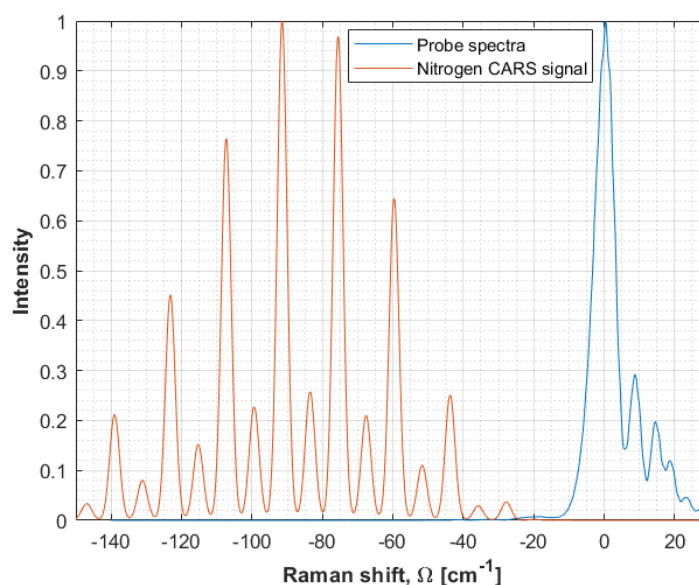


Figure 78: Absence of spectral coincidence of the lower frequency photons from the probe and the CSRS signal from nitrogen as would be seen on the camera. This nitrogen signal is generated with the slit in the 4F – plane closed. Negative frequencies show that the spectrum is red-shifted from the probe and is presented as would be seen on the camera

## Impact of the direct probe on the non-resonant signal

Generally, the non-resonant signal is used to reference the excitation efficiency of the pump/Stokes pulse. Essentially, since the pump/Stokes pulse does not contain a constant intensity per frequency (it is generally a Gaussian shape), each of the Raman transitions are driven with a different intensity and the resulting strength of each Raman line differs for this different reason (than temperature, for example). To remove this effect of excitation efficiency, the non-resonant signal is also recorded, and the resonant spectrum is normalized with this signal. Two such signals were compared in figure 12 and discussed with the theory of CARS.

The non-resonant signal recorded with the slit open shows a shift in its peak and an overall different shape. This is suspected to be because of the asymmetric probe resulting also in an asymmetric non-resonant signal (the comparison is shown in figure 80). This non-resonant signal is then no longer a representation of the excitation efficiency (which should only depend on the pump/Stokes pulse).

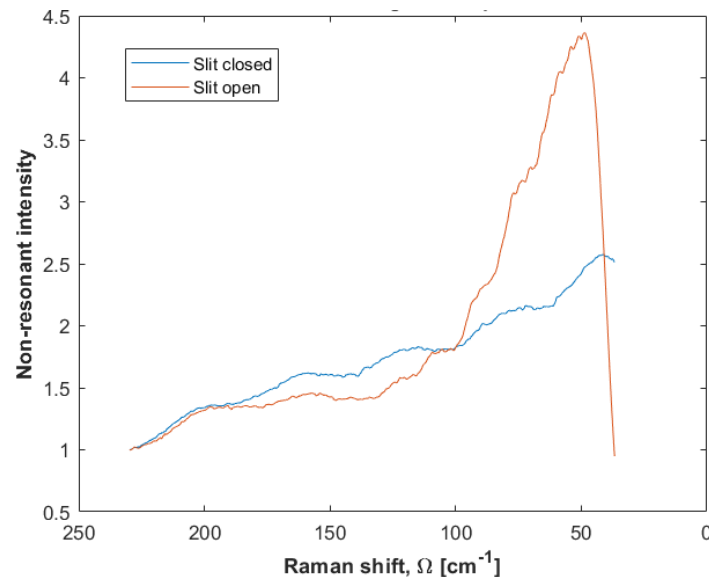


Figure 79: Non-resonant signals from the slit open and slit closed case compared. The initial drop at  $\sim 30 \text{ cm}^{-1}$  is due to the bandpass filter attenuating the signal. Signals were recorded with Argon at room temperature. The orange curve seems to be shifted to the right along with an apparent shorter FWHM in the frequency domain.

Figure 81 shows a synthetic computation of the non-resonant signal produced as a convolution of the probe with the pump/Stokes pulse. This is also compared between the cases with the slit open and closed. This model predicts the differences in the experimental data to an extent, such as the shift in the peak on the non – resonant signal. However, the understanding of the effects on the non – resonant signal from the probe with the slit open is not important to this work. It is important to note, however, that the excitation efficiency can only be accurately captured by a symmetric probe and was done so across all the experiments in this thesis.

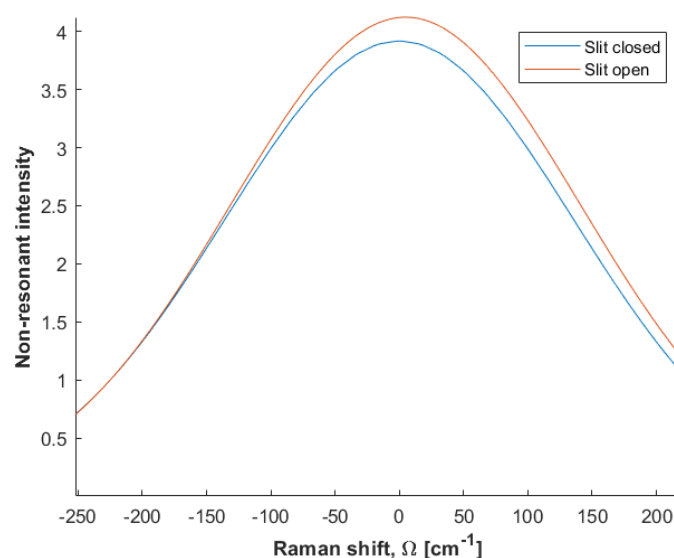


Figure 80: Synthetic computation of the non-resonant signals produced with the slit open and closed. This is computed by performing a convolution of the respective models of the probes with the broadband pump/Stokes pulse.

## Limits on the characterization and validation processes

During the discussion on the correlation of time-arrival information using the non-resonant signal, the impact of flow rate was introduced to explain the limits on the characterization of the pulse in a gas, and it was suggested that the correlation measurement would yield better results if the non-resonant signals were acquired in a solid medium such as glass. In this section, some further limits and sensitivities to the characterization and validation are discussed:

The mechanical slit in the 4F-plane that performs a filter in the frequency domain effectively dumps pulse energy. The pulse, over time, also damages the slit and causes abrasions that slightly widen the slit. This results in additional frequencies being passed through along with their respective time information, which would hurt the correlation experiments. It was found that the rate of damage to the slit is considerable and the effects could be seen within a day of experimentation. This is a major problem and would need to be fixed in future efforts.

## Phase information from the optimization

The optimization was fed with additional experimental data as objectives. Mainly, the entire CSRS spectrochronogram of air at room temperature was reduced to residuals computed at each delay (similar to the objective from the nitrogen spectrochronogram). This aided the optimization process as it reduced the weight of experimental uncertainties due to more information containing information on the probe, invariant about relative intensities, time information, and frequencies.

The tailored genetic algorithm used in this thesis optimizes the arrival times and intensity per conjugate arrival (design variables) to minimize the three objectives of the time- and frequency domain representations of the probe pulse and a period of the room temperature nitrogen CSRS spectrochronogram. While the results of the optimization were more than satisfactory and lead to good fits both in room temperature for multiple species and in the hydrogen diffusion flame, there are some general remarks to be made regarding the optimization process:

To make a comparison, the differences between the optimized design variables and those that were predicted by the correlation measurements using the non-resonant signal are shown in figure 82 for the first and second sidebands.

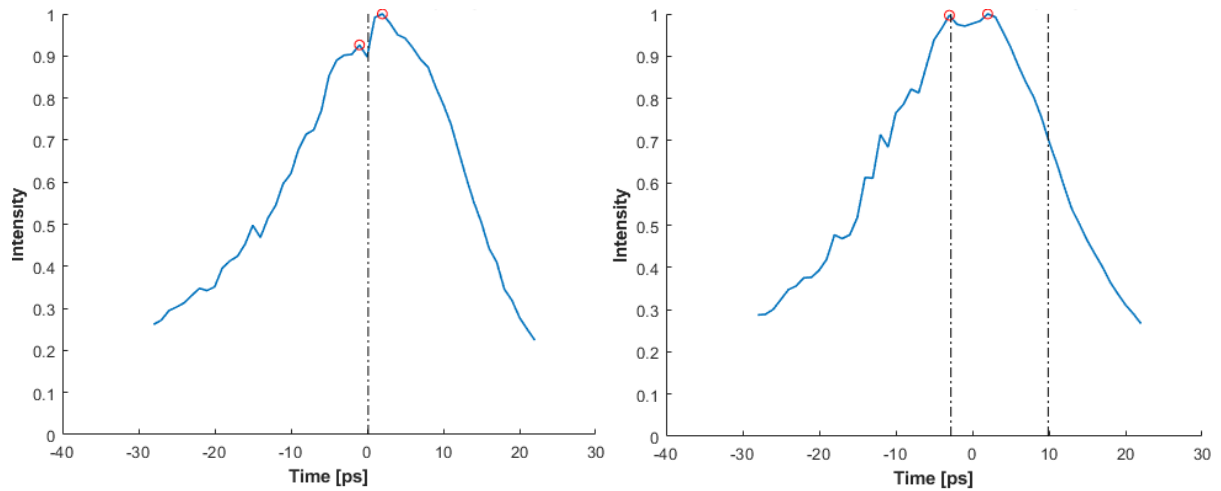


Figure 81: Arrival times resulting from the measurement of the time-domain profile through the non-resonant signal correlation. The profile for the first sideband is shown on the right and the one for the second sideband is shown on the left. In each figure, the blue curve represents the time-domain profile after the discretization at the 4F-filter, the red circles represent the time-arrivals for their respective frequencies as suggested by these profiles, and the black dashed lines mark the optimized time-arrivals predicted by the genetic algorithm.

The optimizer moves one arrival time (the later arrival) of the first sideband to an even later arrival, while it does not change the other. For the second sideband, however, the optimizer moves both arrivals to one location in time, signaling the existence of a strong higher-than-second-order chirp within the broadband pumps that generate this probe pulse. It is important to note that this optimization does not violate constraints by moving the second arrival much farther (in time), and reducing its relative intensity to zero, in the case of the second sideband. Regardless, the effect of the optimizer on arrival times across the different sidebands varies and it was decided that studying the generation of the probe pulse within the SHBC was not of importance to this thesis. Additionally, the extent of the global nature of the minima of the objective function obtained by the optimizer is not analyzed. It is important to note, however, that multiple sets of the optimized phase information retrieved along the optimization process can reconstruct the nitrogen spectrochronogram to a good extent (such as the comparison in figure 64). They vary in the reconstruction of the time- and frequency domain representations which were also used as objectives and retrieved from experiments subject to errors (the time domain representation was especially error-prone due to the fluctuations discussed along with figure 45. This hints at the possibility of multiple sets of phase information that could be presented as the solution to this experimentally bounded problem.

# Bibliography

- [1] T. F. Stocker and Intergovernmental Panel on Climate Change. Working Group I., *Climate change 2013: the physical science basis*. 2013.
- [2] H. Chao, D. B. Agusdinata, D. DeLaurentis, and E. B. Stechel, "Carbon offsetting and reduction scheme with sustainable aviation fuel options: Fleet-level carbon emissions impacts for U.S. airlines," *Transportation Research Part D: Transport and Environment*, vol. 75, pp. 42–56, Oct. 2019, doi: 10.1016/j.trd.2019.08.015.
- [3] A. Flightpath, "2050-europe's vision for aviation," *Advisory Council for Aeronautics Research in Europe*, 2011.
- [4] B. Böhm, J. Brübach, C. Ertem, and A. Dreizler, "Experiments for combustion-LES validation," *Flow, Turbulence and Combustion*, vol. 80, no. 4, pp. 507–529, Jun. 2008, doi: 10.1007/s10494-008-9144-4.
- [5] M. J. Evans and P. R. Medwell, "Understanding and Interpreting Laser Diagnostics in Flames: A Review of Experimental Measurement Techniques," *Frontiers in Mechanical Engineering*, vol. 5, Nov. 2019, doi: 10.3389/fmech.2019.00065.
- [6] S. R. Turns, "An Introduction to Combustion: Concepts and Applications," 2000.
- [7] A. C. Eckbreth, "Laser Diagnostics for Combustion Temperature and Species Measurements," 1996.
- [8] A. C. Eckbreth and T. J. Anderson, "Dual broadband CARS for simultaneous, multiple species measurements," 1985.
- [9] R. W. Boyd, "The Nonlinear Optical Susceptibility," in *Nonlinear Optics*, Elsevier, 2003, pp. 1–65. doi: 10.1016/b978-012121682-5/50002-x.
- [10] C. W. Thiel, "Four-Wave Mixing and its Applications," 2000.
- [11] A. Bohlin, *Development and application of pure rotational CARS for reactive flows*. Division of Combustion Physics, Department of Physics, Lund University, 2012.
- [12] H. Rigneault and P. Berto, "Tutorial: Coherent Raman light matter interaction processes," *APL Photonics*, vol. 3, no. 9, Sep. 2018, doi: 10.1063/1.5030335.
- [13] A. Bohlin, B. D. Patterson, and C. J. Kliewer, "Communication: Simplified two-beam rotational CARS signal generation demonstrated in 1D," *Journal of Chemical Physics*, vol. 138, no. 8, Feb. 2013, doi: 10.1063/1.4793556.
- [14] A. C. Eckbreth, "BOXCARS: Crossed-beam phase-matched CARS generation in gases," *Applied Physics Letters*, vol. 32, no. 7, pp. 421–423, 1978, doi: 10.1063/1.90070.
- [15] A. Lowe, L. M. Thomas, A. Satija, R. P. Lucht, and A. R. Masri, "Chirped-probe-pulse femtosecond CARS thermometry in turbulent spray flames," *Proceedings of the Combustion Institute*, vol. 37, no. 2, pp. 1383–1391, 2019, doi: 10.1016/j.proci.2018.06.149.
- [16] D. R. Richardson, R. P. Lucht, W. D. Kulatilaka, S. Roy, and J. R. Gord, "Theoretical modeling of single-laser-shot, chirped-probe-pulse femtosecond coherent anti-Stokes Raman scattering thermometry," *Applied Physics B: Lasers and Optics*, vol. 104, no. 3, pp. 699–714, Sep. 2011, doi: 10.1007/s00340-011-4489-0.
- [17] S. P. Kearney, D. Farrow, J. D. Miller, and T. R. Meyer, "Strategies for Single-Laser-Shot Femtosecond Pure-Rotational CARS Thermometry," 2012.
- [18] J. D. Miller, "Hybrid femtosecond/picosecond coherent anti-Stokes Raman scattering for gas-phase temperature measurements," 2012. Accessed: Mar. 22, 2021. [Online]. Available: <https://lib.dr.iastate.edu/etd/12610/>
- [19] C.-Y. She, "Spectral structure of laser light scattering revisited: bandwidths of nonresonant scattering lidars," *Applied Optics*, vol. 40, no. 27, p. 4875, Sep. 2001, doi: 10.1364/ao.40.004875.

- [20] M. Hayashi, Y. Nomura, and Y. Fujimura, "Theory of time-resolved coherent anti-Stokes Raman scattering from molecules in liquids. Effects of coherence transfer," *The Journal of Chemical Physics*, vol. 89, no. 1, pp. 34–41, 1988, doi: 10.1063/1.455475.
- [21] N. Torge Mecker *et al.*, "Optimizing hybrid rotational femtosecond/picosecond coherent anti-Stokes Raman spectroscopy in nitrogen at high pressures and temperatures," *Journal of the Optical Society of America B*, vol. 37, no. 4, pp. 1035–1046, 2020, doi: 10.1364/JOSAB.383575.
- [22] G. Plaezek, "Die Rotationsstruktur der Ramanbanden mehratomiger Moleküle."
- [23] H. Bettermann, "Fundamentals of Molecular Symmetry. Series in Chemical Physics. By Philip R. Bunker and Per Jensen.," *Angewandte Chemie International Edition*, vol. 44, no. 41, p. 6616, 2005, doi: <https://doi.org/10.1002/anie.200485285>.
- [24] J. K. G. Watson, "Quadratic Herman-Wallis Factors in the Fundamental Bands of Linear Molecules General theoretical formulas are derived for the coefficients in the terms A?," 1987.
- [25] A. Bohlin, P. E. Bengtsson, and M. Marrocco, "On the sensitivity of rotational CARS N<sub>2</sub> thermometry to the Herman-Wallis factor," *Journal of Raman Spectroscopy*, vol. 42, no. 10, pp. 1843–1847, Oct. 2011, doi: 10.1002/jrs.2869.
- [26] S. P. Kearney, D. J. Scoglietti, and C. J. Kliewer, "Hybrid femtosecond/picosecond rotational coherent anti-Stokes Raman scattering temperature and concentration measurements using two different picosecond-duration probes," *Optics Express*, vol. 21, no. 10, p. 12327, May 2013, doi: 10.1364/oe.21.012327.
- [27] P. v. Kolesnichenko, J. O. Tollerud, and J. A. Davis, "Background-free time-resolved coherent Raman spectroscopy (CSRS and CARS): Heterodyne detection of low-energy vibrations and identification of excited-state contributions," *APL Photonics*, vol. 4, no. 5, May 2019, doi: 10.1063/1.5090585.
- [28] T. Seeger, J. Kiefer, A. Leipertz, B. D. Patterson, C. J. Kliewer, and T. B. Settersten, "Picosecond time-resolved pure-rotational coherent anti-Stokes Raman spectroscopy for N<sub>2</sub> thermometry RCARS spectra from pure N<sub>2</sub> at 294 K and 1 bar and from N<sub>2</sub> at 1100 K on the fuel-rich side of an," 2009.
- [29] R. Paschotta, "RP Photonics," *RP Photonics*, 2020. [https://www.rp-photonics.com/transform\\_limit.html](https://www.rp-photonics.com/transform_limit.html) (accessed Apr. 19, 2021).
- [30] Jean-Claude Diels and Wolfgang Rudolph, *Ultrashort Laser Pulse Phenomena*, 2nd ed. 2006. Accessed: Apr. 19, 2021. [Online]. Available: <https://www.elsevier.com/books/ultrashort-laser-pulse-phenomena/liao/978-0-12-215493-5>
- [31] R. Paschotta, "Chirp," *RP Photonics*, 2020. <https://www.rp-photonics.com/chirp.html> (accessed Apr. 19, 2021).
- [32] D. R. Richardson, R. P. Lucht, S. Roy, W. D. Kulatilaka, and J. R. Gord, "Single-laser-shot femtosecond coherent anti-Stokes Raman scattering thermometry at 1000 Hz in unsteady flames," *Proceedings of the Combustion Institute*, vol. 33, no. 1, pp. 839–845, 2011, doi: 10.1016/j.proci.2010.05.060.
- [33] Laurie Ann Peach, "Gratings separate the different colors of light," *Laser Focus World*, 1997. <https://www.laserfocusworld.com/optics/article/16550914/gratings-separate-the-different-colors-of-light> (accessed Apr. 19, 2021).
- [34] W. D. Kulatilaka, J. R. Gord, and S. Roy, "Effects of O<sub>2</sub>-CO<sub>2</sub> polarization beating on femtosecond coherent anti-Stokes Raman scattering (fs-CARS) spectroscopy of O<sub>2</sub>," *Applied Physics B: Lasers and Optics*, vol. 102, no. 1, pp. 141–147, Jan. 2011, doi: 10.1007/s00340-010-4188-2.
- [35] L. Castellanos, F. Mazza, D. Kliukin, and A. Bohlin, "Pure-rotational 1D-CARS spatiotemporal thermometry with a single regenerative amplifier system," *Optics Letters*, vol. 45, no. 17, p. 4662, Sep. 2020, doi: 10.1364/ol.398982.
- [36] R. P. Lucht, S. Roy, T. R. Meyer, and J. R. Gord, "Femtosecond coherent anti-Stokes Raman scattering measurement of gas temperatures from frequency-spread

- dephasing of the Raman coherence,” *Applied Physics Letters*, vol. 89, no. 25, 2006, doi: 10.1063/1.2410237.
- [37] T. Y. Chen, B. M. Goldberg, E. Kolemen, Y. Ju, and C. J. Kliewer, “Time and frequency-domain FS/PS cars measurements and modelling of the ch4 V1 vibrational q-branch,” in *AIAA Scitech 2021 Forum*, 2021, pp. 1–10. doi: 10.2514/6.2021-1143.
- [38] S. Legros, W. Kulatilaka, B. Barviau, and F. Grisch, “Femtosecond Pure Rotational Chirped-Probe-Pulse CARS for single-shot thermometry in flames,” 2020.
- [39] S. Zamith, Z. Ansari, F. Lepine, and M. J. J. Vrakking, “Single-shot measurement of revival structures in femtosecond laser-induced alignment of molecules,” 2005.
- [40] N. Owschimikow, B. Schmidt, and N. Schwentner, “Laser-induced alignment and anti-alignment of rotationally excited molecules,” *Physical Chemistry Chemical Physics*, vol. 13, no. 19, pp. 8671–8680, May 2011, doi: 10.1039/c0cp02260h.
- [41] Y. I. Salamin and S. Carbajo, “A simple model for the fields of a chirped laser pulse with application to electron laser acceleration,” *Frontiers in Physics*, vol. 7, no. FEB, 2019, doi: 10.3389/fphy.2019.00002.
- [42] S. Chandra, A. Compaan, and E. Wiener-Avneart, “Phase Matching in Coherent Anti-Stokes Raman ScatterFng,” 1981.
- [43] F. Mazza, L. Castellanos, D. Kliukin, and A. Bohlin, “Coherent Raman imaging thermometry with in-situ referencing of the impulsive excitation efficiency,” *Proceedings of the Combustion Institute*, 2020, doi: 10.1016/j.proci.2020.06.360.
- [44] S. P. Kearney and D. J. Scoglietti, “Hybrid femtosecond/picosecond rotational coherent anti-Stokes Raman scattering at flame temperatures using a second-harmonic bandwidth-compressed probe,” 2013.
- [45] T. L. Courtney, N. T. Mecker, B. D. Patterson, M. Linne, and C. J. Kliewer, “Generation of narrowband pulses from chirped broadband pulse frequency mixing,” *Optics Letters*, vol. 44, no. 4, p. 835, Feb. 2019, doi: 10.1364/ol.44.000835.
- [46] H. Zhao, Z. Tian, T. Wu, Y. Li, and H. Wei, “Dynamic and sensitive hybrid fs/ps vibrational CARS thermometry using a quasi-common-path second-harmonic bandwidth-compressed probe,” *Applied Physics Letters*, vol. 118, no. 7, Feb. 2021, doi: 10.1063/5.0036303.
- [47] B. Li, O. K. Ersoy, C. Ma, Z. Pan, W. Wen, and Z. Song, “A 4F optical diffuser system with spatial light modulators for image data augmentation,” *Optics Communications*, p. 126859, Feb. 2021, doi: 10.1016/j.optcom.2021.126859.
- [48] F. Vestin, M. Afzelius, and P. E. Bengtsson, “Development of rotational CARS for combustion diagnostics using a polarization approach,” *Proceedings of the Combustion Institute*, vol. 31 I, no. 1, pp. 833–840, 2007, doi: 10.1016/j.proci.2006.07.066.

# Acknowledgments

In the past year, a lot has happened and the world has changed. There were periods of uncertainty for a lot of us, and there were some parts that were enjoyed less. In spite of this, I have enjoyed my time at TU Delft, and especially during my thesis where I got to work on something challenging, interesting, hands-on, and rewarding. I hope to follow a career path that keeps me as curious and as excited as I have been during this time. The thesis would not have been so enjoyable without the help and support of a lot of people. I would like to mention a few here.

Ir. Leonardo Castellanos, I appreciate everything you have done for me. By working with you, I have gained so much experience on how an experimentalist thinks and acts, and the many nuances that go into a successful experimental campaign. There were some long days in the lab, and you were always calm and ready for every obstacle we had to face. I also made mistakes that you helped me learn from and I hope to someday work in a laboratory with the knowledge and skill that you showed me. I think you have a very successful career ahead.

Ir. Francesco Mazza, our conversations on extremely general topics including politics, beer, and physics were always intriguing. You have made me think about what I want to do in my career in a more challenging way that will not let me take a simple road I think. I always dropped whatever I was doing when I could see you were starting to talk about physics, and I hope someday I can be a good enough sparring partner as well. Regardless, I am sure you will be a positive influence on all your future colleagues.

Dr. Alexis Bohlin, I am full of thanks for giving me this opportunity to work on such fundamental research, this was more than what I expected when I started in this group. It also has to be said that this group with all the Ph.D. and master students was such a positive atmosphere to work in, and the credit has to go to you for everything you do to ensure it. I wish you all the success at your new lab in Sweden!

Dr. Dmitrii Kliukin, you initiated me into the world of light-matter interaction and I can remember how simple everything sounded when you explained it. I am grateful to have had you as my supervisor for that part of my thesis, and I hope you continue in academia as I can see it helping a lot of students.

Aert Stutvoet, I hope to congratulate you on your graduation next week! We were very much on the same level of progress in our theses and I think it helped both of us in the last couple of months where we could bounce ideas off each other. I respect your work ethic very much (and also the quality of your graphs). I think you will do well in whatever you set out to do next.

I would lastly like to thank all my friends and family for their continued support. Especially my parents and my sister – who I will always count on.